Roma Tre

CORSO DI DOTTORATO DI RICERCA IN FISICA

CICLO XXXVIII

Front-End Electronics Characterization and Inverse Beta Decay Monte Carlo Studies in the JUNO-TAO Experiment

Elia Stanescu Farilla

Nome e Cognome del dottorando firma

Stefano Maria Mari

Docente Guida: Prof. firma

Giorgio Matt

Coordinatore: Prof. firma

Dipartimento di Matematica e Fisica
PhD in Physics, XXXVIII Cycle

Front-End Electronics Characterization and Inverse Beta Decay Monte Carlo Studies in the JUNO-TAO Experiment

Supervisor
Stefano Maria Mari

Candidate
Elia Stanescu Farilla

31st March 2026

Contents

Introduction

Neutrinos are among the most elusive and intriguing particles in the Standard Model of particle physics. In 1930 Pauli suggested the hypothesis of a neutral particle of very low mass to explain the energy spectrum of the beta decay [1]. Few years later Fermi incorporated this particle in his theory of beta decay and called it ”neutrino” [2]. Then, in 1956, Cowan and Reines realized an experiment detecting for the first time neutrinos from a nuclear reactor [3]. Soon after, in 1957, Pontecorvo suggested for the first time the hypothesis of neutrino oscillations [4].

The discovery of neutrinos marked the beginning of an extensive experimental program that, over the decades, has revealed unexpected properties of these particles. In particular, the observation of neutrino oscillations in 1998 by the Super-Kamiokande experiment [5] provided the first clear evidence of physics beyond the Standard Model, establishing that neutrinos are massive and that lepton flavor is not conserved.

In the current era of neutrino physics, the focus has shifted toward precision measurements of the oscillation parameters and the resolution of the remaining open questions, among which the determination of the neutrino mass ordering represents a major challenge. Medium-baseline reactor experiments play a unique role in this context, as they allow mass ordering to be probed through vacuum oscillations with minimal dependence on matter effects. The Jiangmen Underground Neutrino Observatory (JUNO), in the Guangdong province in South China, is one of the most promising new-generation experiments in the sector. With its 30k tons target, JUNO is the largest liquid scintillator experiment ever built. By detecting antineutrinos from six reactors, JUNO aims to determine the neutrino mass ordering up to 3σ within six years of data taking, and to measure the oscillation parameters with precision below 1%. The JUNO experiment started operations in August 2025 and, with less than 60 effective days of data taking, managed to measure solar oscillation parameters with world-leading precision.

The Taishan Antineutrino Observatory (TAO) is a satellite experiment of JUNO, consisting of a ton-level liquid scintillator detector. Operating at a very short distance from one of the reactors of the Taishan nuclear power plant, TAO is designed to perform high precision measurements of the unoscillated reactor antineutrino spectrum, essential for JUNO to reach the sensitivity to solve the mass ordering problem. To achieve this objective, TAO will reach an unprecedented energy resolution below 2% at 1 MeV. The realization of this incredible result relies on its unique experimental features, such as the use of silicon photomultipliers, the gadolinium-doping of the scintillator, and the operation at cryogenic temperatures.

This thesis presents the work I carried out as a PhD student within the JUNO collaboration, focusing on the TAO experiment. The first part of the work concerns the characterization of the TAO front-end electronics and silicon photomultipliers. The JUNO group of Roma Tre University was committed to design and produce two fundamental components of the TAO front-end electronics: the front-end boards that couple with the silicon photomultipliers and the analog-to-digital converters. I contributed to the experimental characterization of pre-production front-end boards, performing measurements to assess their performance, noise behavior, and stability when coupled to silicon photomultipliers. These characterization studies are crucial since the performance of the silicon photomultipliers directly impacts the achievement of the record energy resolution that TAO is expected to reach. I also contributed to the mass testing of the front-end boards and ADCs, which are now installed and being used in the commissioning phase of the TAO detector. All measurements were performed at the INFN laboratories (Istituto Nazionale di Fisica Nucleare) of Roma Tre University.

During my PhD I went several times in China to participate to the international JUNO collaboration meetings, and, in June 2025 I contributed to the installation of the TAO central detector at the Taishan nuclear power plant.

The second part of the thesis is dedicated to the Monte Carlo simulation of inverse beta decay events in the TAO detector. These simulations represent a fundamental tool to model the interaction of particles within the detector and to quantitatively describe its response. In particular, they allow the connection between the true physical quantities, such as the energy of the incoming antineutrino and the positron, and the experimentally accessible observables, such as the number of photoelectrons detected by the silicon photomultipliers. The Monte Carlo framework is also used to study detector effects, including energy leakage, resolution, and non-linearities, which play a crucial role in high-precision measurements. These simulations therefore provide an essential input for the interpretation of experimental data and for the construction of the detector response model.

The thesis is organized as follows. Chapter 1 introduces the theoretical framework of neutrino physics, with particular emphasis on neutrino oscillations. Chapter 2 describes the JUNO and TAO experiments, their physics goals and detector designs. Chapter 3 presents the characterization of the TAO silicon photomultipliers and front-end electronics, including measurements and performance results. Chapter 4 focuses on Monte Carlo simulation of inverse beta decay events in the TAO detector.

Chapter 1

Neutrino Physics

1.1 Neutrino oscillations

Our current understanding of nature is based on the existence of fundamental forces governing physical phenomena. In our current knowledge, we can distinguish four of them: electromagnetic, weak, strong and gravity forces. Quantum field theory [6, 7, 8] allowed us to describe in only one theory the first three. This theory, based on the local symmetry $SU(3) \times SU(2) \times U(1)$ is called Standard Model (SM) of particles. The SM is one of the most successful models in physics, being able to predict with an astonishing precision different processes. The Standard Model describes three of the fundamental forces as mediated by the exchange of particles, in particular spin 1 bosons. The matter particles, on the other hand, are divided in three generations of spin 1/2 fermions, each of them including two quarks and two leptons. The symmetry principles that are behind the construction of the standard model predict that all the particles must be massless. However, we observe that most of the particles we know do have masses [9]. The mechanism that generates such masses is a spontaneous symmetry breaking (SSM) process called Higgs mechanism [10] The particle responsible for this mechanism is a spin 0 boson, the Higgs boson, which completes the particle content of the SM. This particle, introduced in the theory in the 1964 has been observed in 2012 at the Large Hadron Collider [11, 12] confirming the incredible predictive power of the SM. Despite its great success [13], the Standard Model still fails to explain some very important phenomena [14, 15]. One of them will be treated with particular focus in this thesis: neutrino oscillation, which have been one of the most studied processes in the last decades. Several neutrino experiments succeeded in observing the phenomenon and in measuring the parameters involved. In this chapter we will discuss the formalism of the oscillations in vacuum and in matter as well as the strategies one can adopt to measure the oscillation parameters.

1.1.1 Formalism of the oscillations

If neutrinos are massive, whatever their mass is, they can undergo the phenomenon of neutrino oscillations. As we will show in few lines, we only require that all the three neutrinos do not have the same mass. The theory of neutrino oscillations was born at the time of the first neutrino observations [4, 3]. Then, in the following decades, such phenomenon has been used to explain some discrepancies between data and theory until it has been observed and discovered in 1998 by the Super-Kamiokande experiment [5]. Neutrino oscillations occur when neutrinos change their flavor during their propagation. This process is governed by the oscillation probabilities, which can be obtained from a mixing matrix and the knowledge of the differences between neutrino masses. The mixing matrix is called PMNS (Pontecorvo-Maki-Nakagawa-Sakata) matrix [4, 16] and can be parameterized using three mixing angles and a complex phase

$$\begin{aligned} U_{PMNS} &= \begin{pmatrix} 1 & 0 & 0 \\ 0 & c_{23} & s_{23} \\ 0 & -s_{23} & c_{23} \end{pmatrix} \begin{pmatrix} c_{13} & 0 & s_{13}e^{-i\delta} \\ 0 & 1 & 0 \\ -s_{13}e^{i\delta} & 0 & c_{13} \end{pmatrix} \begin{pmatrix} c_{12} & s_{12} & 0 \\ -s_{12} & c_{12} & 0 \\ 0 & 0 & 1 \end{pmatrix} \\ &= \begin{pmatrix} c_{12}c_{13} & s_{12}c_{13} & s_{13}e^{-i\delta} \\ -s_{12}c_{23} - c_{12}s_{23}s_{13}e^{i\delta} & c_{12}c_{23} - s_{12}s_{23}s_{13}e^{i\delta} & s_{23}c_{13} \\ s_{12}s_{23} - c_{12}c_{23}s_{13}e^{i\delta} & -c_{12}s_{23} - s_{12}c_{23}s_{13}e^{i\delta} & c_{23}c_{13} \end{pmatrix} \end{aligned} \tag{1.1}$$

where $s_{ij} = \sin\theta_{ij}$ and $c_{ij} = \cos\theta_{ij}$, where $\delta{=}\delta_{CP}$ is responsible for CP violation. The complex phase $\delta{=}\delta_{CP}$ appearing in the PMNS matrix introduces the possibility of CP violation in the leptonic sector. If δ_{CP} differs from 0 or π, the oscillation probabilities of neutrinos and antineutrinos are not identical, leading to measurable differences in the appearance or disappearance rates of different flavors. The observation of CP violation in the neutrino sector would have profound implications for our understanding of fundamental physics. In particular, it could provide an important ingredient for mechanisms such as leptogenesis, which attempt to explain the observed matter–antimatter asymmetry of the Universe through CP-violating processes involving leptons in the early Universe.

Let us now discuss how to obtain the neutrino flavor transition probabilities. First of all, we can consider a neutrino flavor eigenstate of momentum p.

This state must be created from the vacuum by the neutrino conjugate field, thus can be written as superposition of mass eigenstates in the following way

$$|\nu_\alpha(p)\rangle = \sum_i U^*_{\alpha i} |\nu_\alpha(p)\rangle \tag{1.2}$$

where the greek subscripts denotes the flavors, the latin ones the mass eigenstates. The matrix U is the leptonic PMNS mixing matrix. In the ultra-relativistic regime, writing the flavor state as a superposition of mass states with the same momentum is the same as considering the mass states to have the same energy. If we consider the neutrino state after a time t, it evolves, following the Schroedinger equation

$$|\nu_\alpha(p)\rangle = \sum_i e^{-iE_i t} U^*_{\alpha i} |\nu_\alpha(p)\rangle \tag{1.3}$$

where E is the neutrino energy. When we deal with neutrinos we are always in the ultra-relativistic limit. Thus, assuming $c = 1$ and $\hbar = 1$, we can write

$$E_i = \sqrt{p^2 + m_i^2} \sim p + \frac{m_i^2}{2p} \tag{1.4}$$

where we assumed that all eigenstates have the same momentum. If we want to determine the probability that a neutrino of flavor α turns into a neutrino of flavor β at a given time t, we need the following amplitude

$$\begin{aligned} A_{\alpha\beta} &= \langle \nu_\beta(p,t) | \nu_\alpha(p,t)\rangle = \sum_{i,j} U_{\beta j} U^*_{\alpha i} e^{-iE_i t} \langle \nu_j(p) | \nu_i(p)\rangle = \qquad (1.5) \\ &= \sum_i U_{\beta i} U^*_{\alpha i} e^{-iE_i t} \end{aligned}$$

which has to be squared

$$\begin{aligned} P_{\alpha\beta} &= \left| \sum_i U_{\beta i} U^*_{\alpha i} e^{-iE_i t} \right| \qquad (1.6) \\ &= \sum_{i,j} U_{\beta i} U^*_{\alpha i} U^*_{\beta j} U_{\alpha j} e^{-i(E_i - E_j)t}. \end{aligned}$$

In the ultra-relativistic limit, we can write $t \sim L$ and $p \sim E$, obtaining that $E_i - E_j = (m_i^2 - m_j^2)L/2E = \Delta m_{ij}^2 L/2E$. Thus, as already mentioned, the oscillation probabilities only depend on the so-called *mass splittings* Δm_{ij}^2; this is the reason why we need not only non-vanishing, but also non-degenerate mass eigenstates to observe neutrino oscillations. Rewriting eq. 1.6 in a convenient way, we obtain the general neutrino oscillation formula

$$\begin{aligned} P_{\alpha\beta} &= \delta_{\alpha\beta} - 4\sum_{i<j} \Re[U_{\beta i}U^*_{\alpha i}U^*_{\beta j}U_{\alpha j}] \sin^2\left(\frac{\Delta m^2_{ij}}{4E}L\right) + \\ &\quad +2\sum_{i<j} \Im[U_{\beta i}U^*_{\alpha i}U^*_{\beta j}U_{\alpha j}] \sin\left(\frac{\Delta m^2_{ij}}{2E}L\right) . \end{aligned} \tag{1.7}$$

Some remarks about the probabilities. If we consider antineutrinos, we need the substitution $U \to U^*$. Thus, the first two terms of the probabilities are unaltered, while the last term which involves the imaginary part of the combination of matrix elements changes sign. For this reason, if the mixing matrix is real, there are no differences in the probabilities (no CP violation). In the three neutrino framework, however, we have one complex phase surviving in the matrix and for this reason we expect in general to observe CP violation. Moreover, any rephasing of the mixing matrix, do not affect probabilities. Thus, Majorana phases cannot be determined studying oscillations. Another interesting approach to obtain oscillation probability, makes use of the neutrino Hamiltonian. In this case we describe neutrinos as n level quantum mechanical system. Given that, it is possible to write the flavor eigenstates vector in terms of the mass eigenstates vector through the mixing matrix $\nu_f = U\nu_m$. The Hamiltonian of the system in the mass basis is the free particle one, namely

$$(H_m)_{ij} = \delta_{ij}\left(p + \frac{m_i^2}{2E}\right) . \tag{1.8}$$

The subtraction of a contribution proportional to the identity matrix does not affect the oscillation probabilities. The Hamiltonian matrix can be thus written equivalently as

$$H_m = \frac{1}{2E}\,\mathrm{diag}(0, \Delta m^2_{21}, \Delta m^2_{31}). \tag{1.9}$$

In the flavor basis, the Hamiltonian becomes $H_f = UH_mU^\dagger$. Using the Schrödinger equation for the Hamiltonian operator, we obtain a transition amplitude equivalent to the previous expression

$$\begin{aligned} A_{\alpha\beta} &= \nu^\dagger_\beta U e^{-iH_mL}U^\dagger\nu_\alpha = \\ &= U_{\beta j}\nu^\dagger_j e^{-iH_mL}\nu_i U^*_{\alpha i} = \\ &= \sum_i U_{\beta i}U^*_{\alpha i}e^{-i\frac{\Delta m^2_{ij}L}{2E}} \end{aligned} \tag{1.10}$$

1.1.2 Oscillations in matter

If neutrino travel through the Earth, or in any matter media, they can undergo weak interactions; this can alter the oscillation probabilities. Wolfestein, Mikheyev and Smirnov [17, 18, 19] studied for the first time the effect of the matter (called MSW effect) in neutrino propagation. Indeed, the neutrino Hamiltonian can get contributions at the first order in the small coupling G_F if we consider the coherent forward scattering on the matter particles. Even though the contribution is small, it has to be compared to neutrino mass splittings (which appear in the free Hamiltonian) and for this reason it can become non-negligible. Let us now consider the processes which occur during neutrino propagation in matter. They can be Neutral Current (NC) interactions, in which a neutrino of whatever flavor scatters on a proton, a neutron or an electron exchanging a Z boson, or Charged Current (CC) interactions, in which only the electron neutrino scatters on matter electrons exchanging a W boson. The Feynmann diagrams corresponding to the two interactions are shown in Figure 1.1. We will focus on the latter contribution first. The lagrangian term is the usual charged current lagrangian which can be written as

$$\mathcal{L}_{CC} = \frac{G_F}{\sqrt{2}}[\bar{\nu}_e \gamma^\mu (1-\gamma^5) e][\bar{e}\gamma_\mu (1-\gamma_5)\nu_e] \tag{1.11}$$

and becomes

$$\mathcal{L}_{CC} = \frac{G_F}{\sqrt{2}}[\bar{\nu}_e \gamma^\mu (1-\gamma^5) \nu_e][\bar{e}\gamma_\mu (1-\gamma_5) e] \tag{1.12}$$

after a Fierz transformation [20]. Since in the medium in which neutrinos are propagating we have not single particles but an electron number density N_e, we can define the electron density matrix

$$\rho_e = \frac{1}{2}\sum_s \int d^3p \frac{|e(\vec{p},s)\rangle \langle e(\vec{p},s)|}{2p_0} N_e f(p,T) \tag{1.13}$$

where f is the normalized statistical momentum distribution of electrons at a given temperature T. Thus, we can integrate out the electrons in the lagrangian using this density matrix in the following way

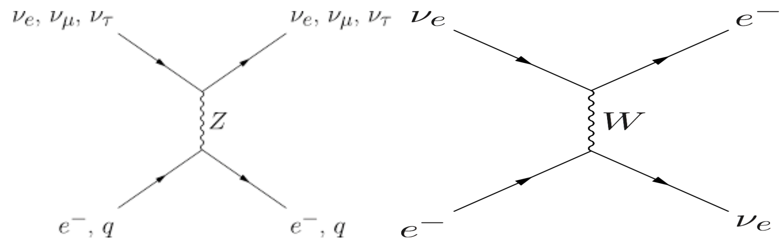

Figure 1.1: Feynman diagrams of the neutral current (left) and charged current (right) neutrino interactions with matter.

$$\begin{aligned}
\mathcal{L}_{CC}^{eff} &= Tr(\mathcal{L}_{CC}\rho_e) = \qquad (1.14)\\
&= -\frac{G_F}{\sqrt{2}}[\bar{\nu}_e\gamma^\mu(1-\gamma^5)\nu_e]\frac{N_e}{2}\sum_s\int\frac{d^3p}{2p_0}\langle e(\vec{p},s)|\,\bar{e}\gamma_\mu(1-\gamma^5)e\,|e(\vec{p},s)\rangle f(p,T) =\\
&= -\frac{G_F N_e}{2\sqrt{2}}[\bar{\nu}_e\gamma^\mu(1-\gamma^5)\nu_e]\int d^3pTr\left[\frac{\not{p}+m}{2p_0}\gamma_\mu(1-\gamma^5)\right]f(p,T) =\\
&= -\frac{G_F N_e}{\sqrt{2}}[\bar{\nu}_e\gamma^\mu(1-\gamma^5)\nu_e]\int d^3p\frac{p_\mu}{p_0}f(p,T).
\end{aligned}$$

In the rest frame of the matter medium the momentum distribution can be considered an even function. Thus, the integral vanishes unless $\mu = 0$. Using the normalization of the distribution, we finally obtain

$$\mathcal{L}_{CC}^{eff} = -\frac{G_F N_e}{\sqrt{2}}[\bar{\nu}_e\gamma^0(1-\gamma^5)\nu_e]\,. \qquad (1.15)$$

This term, linear in the weak coupling G_F, becomes a new contribution to the neutrino self energy that can be written as $\xi_{CC} = \sqrt{2}G_F N_e\gamma^0 P_L$ where $P_L = \frac{1-\gamma^5}{2}$ is the operator which picks only the left handed neutrino component. The dispersion relation thus becomes

$$(E-\sqrt{2}G_F N_e)^2 = m^2 + p^2 \qquad (1.16)$$

that, in the ultra-relativistic limit, can be written as

$$E \sim p + \frac{m^2}{2p} + \sqrt{2}G_F N_e. \qquad (1.17)$$

If we consider the existence of three different neutrino flavors, the Hamiltonian is therefore modified with the addition of the term

$$H_{CC} = \sqrt{2}G_F N_e\,\mathrm{diag}(1,0,0) \qquad (1.18)$$

since only the first neutrino flavor, namely the electron one, can undergo CC interactions during the propagation. If we consider antineutrinos, p_0 is negative; for this reason, the matter potential term in the Hamiltonian changes sign in this case. Thus, the matter potential, together with the PMNS matrix phase, are the only parameters responsible for the differences between neutrino and antineutrino oscillation probabilities. Let us now consider the NC contribution. Such interactions can involve any neutrino flavor and any matter particle. If we are in a neutral medium, electrons and protons are in equal number and for this reason their contributions (which have opposite signs) cancel out. The only remaining term is due to the neutrons density. Considering the NC lagrangian and repeating the same procedure discussed for the CC interactions, we obtain a new contribution to the neutrino Hamiltonian

$$H_{NC} = -\frac{G_F N_n}{\sqrt{2}} \operatorname{diag}(1,1,1) \tag{1.19}$$

where N_n is the neutron number density. In this case, since the neutral current interactions are flavor independent, this contribution does not affect the oscillations, since it is proportional to the identity and can be subtracted from the Hamiltonian. However, if there are sterile neutrinos or if we consider other exotic physics this term can be important and can affect oscillations.
If the electron density is constant through the medium, we only have an additional term in the Hamiltonian which changes its eigenstates and eigenvalues. Thus, the matrix is no longer diagonalized in the flavor basis by the PMNS matrix, but by a new matrix $\tilde{U}$ that depends on the mixing angles and phases and on the matter potential. On the other hand, if the electron density is not constant, the matter neutrino eigenstates in matter will become time-dependent. In the flavor basis the time evolution equation is in this case

$$i\frac{d\nu_f}{dt} = H_f \nu_f \quad \longrightarrow \quad i\frac{d(\tilde{U}\tilde{\nu})}{dt} = \tilde{U} H_d \tilde{U}^\dagger \tilde{U}\tilde{\nu} \tag{1.20}$$

where $\tilde{\nu}$ are the new matter eigenstates and $H_d = \tilde{U}^\dagger H_f \tilde{U}$ is the diagonalized effective Hamiltonian. Since now both the matrix $\tilde{U}$ and the eigenstates are time dependent, the equation becomes

$$i\tilde{U}\frac{d\tilde{\nu}}{dt} + i\frac{d\tilde{U}}{dt}\tilde{\nu} = \tilde{U} H_d \tilde{\nu} \quad \longrightarrow \quad i\frac{d\tilde{\nu}}{dt} = \left(\tilde{U} - i\tilde{U}^\dagger \frac{d\tilde{U}}{dt}\right)\tilde{\nu}. \tag{1.21}$$

From this time evolution equation it is possible to extract the oscillation probabilities in the most general way.

1.1.3 Two flavors oscillations

In nature we know that neutrinos can assume three different flavors (or at least three different active flavors, since we have hints of the presence of sterile neutrinos, but we have not discovered them yet). However, it can be useful to study neutrino oscillations in the two flavors approximation. In this case the transition probabilities are easier to handle (in the full framework the expressions can be very cumbersome, as we will discuss later) and can explain different features of the phenomenon. Moreover, given the two measured values of the mass splittings (which are very different one to each other), in certain circumstances, it is possible to decouple fast oscillations from slow oscillations and study the experimental results using the two flavors formulae. The two-flavors neutrino mixing matrix can be parameterized using only one angle and can be written as

$$U = \begin{pmatrix} \cos\theta & \sin\theta \\ -\sin\theta & \cos\theta \end{pmatrix}. \tag{1.22}$$

Thus, there are no complex phases and for this reason we cannot expect CP violation. The only mass splitting is $\Delta m^2 = m_2^2 - m_1^2$, and the neutrino Hamiltonian (in vacuum) is

$$H_f = \frac{\Delta m^2}{2E} \begin{pmatrix} \cos\theta & \sin\theta \\ -\sin\theta & \cos\theta \end{pmatrix} \begin{pmatrix} 0 & 0 \\ 0 & 1 \end{pmatrix} \begin{pmatrix} \cos\theta & -\sin\theta \\ \sin\theta & \cos\theta \end{pmatrix}. \tag{1.23}$$

which becomes

$$H_f = \frac{\Delta m^2}{2E} \begin{pmatrix} \sin^2\theta & \sin\theta\cos\theta \\ \sin\theta\cos\theta & \cos^2\theta \end{pmatrix}. \tag{1.24}$$

Since we can subtract a contribution proportional to the identity without changing the oscillation probabilities, we can write the Hamiltonian also as

$$H_f = \frac{\Delta m^2}{4E} \begin{pmatrix} -\cos(2\theta) & \sin(2\theta) \\ \sin(2\theta) & \cos(2\theta) \end{pmatrix} \tag{1.25}$$

that allows us to obtain the oscillation probabilities very easily. The two eigenvalues of the Hamiltonian in this basis are indeed just $E_{1/2} = \pm\Delta m^2/4E$, while the two eigenvectors are $\nu_1 = (\cos\theta, \sin\theta)$ and $\nu_2 = (\sin\theta, -\cos\theta)$. Thus, at a given time t (or distance L), the neutrino flavor states are

$$\begin{aligned} |\nu_\alpha\rangle &= \cos\theta e^{-i\frac{\Delta m^2 L}{4E}} |\nu_1\rangle + \sin\theta e^{i\frac{\Delta m^2 L}{4E}} |\nu_2\rangle \qquad (1.26) \\ |\nu_\beta\rangle &= \sin\theta e^{-i\frac{\Delta m^2 L}{4E}} |\nu_1\rangle - \cos\theta e^{i\frac{\Delta m^2 L}{4E}} |\nu_2\rangle \end{aligned}$$

and the transition amplitude is simply

$$A_{\alpha\beta} = \langle \nu_\beta(L)|\nu_\alpha(0)\rangle = \sin\theta\cos\theta\left(e^{i\frac{\Delta m^2 L}{4E}} - e^{-i\frac{\Delta m^2 L}{4E}}\right) = \\ i\sin(2\theta)\sin\left(\frac{\Delta m^2 L}{4E}\right). \tag{1.27}$$

Squaring it we obtain the probability that a neutrino of energy E changes its flavor after a distance L, which is

$$P_{\alpha\beta} = \sin^2(2\theta)\sin^2\left(\frac{\Delta m^2 L}{4E}\right). \tag{1.28}$$

We usually refer to this probability as the ν_β *appearance*. We can obtain the same result using the general formula written in terms of entries of the mixing matrix (see eq. 1.8). It is possible to notice that the mixing angle θ define the amplitude of the oscillations. Thus, if the angle is very small, the appearance probability is very close to zero, while if it is maximal ($\pi/4$), then the probability can easily reach 1 when the oscillating term is maximized. In particular, we can define an oscillation length

$$L_0 = \frac{2\pi E}{\Delta m^2} \tag{1.29}$$

that refers to the distance that a neutrino of energy E should travel to have the maximum probability of a flavor change, namely $P_{\alpha\beta}^{max} = \sin^2(2\theta)$. Every odd multiples of the length L_0 gives maximum probability, while every even multiples the probability is zero. Moreover, since the mixing matrix is real, it is easy to demonstrate that $P_{\alpha\beta} = P_{\beta\alpha}$. Given a neutrino of flavor α, the relation

$$\sum_f P_{\alpha f} = 1 \tag{1.30}$$

must hold, where $f = \alpha, \beta$ is the final flavor. This is a direct consequence of the unitarity of the time evolution operator, but it is also easy to understand from a practical point of view. From this relation we can obtain the so called *disappearance probabilities*

$$P_{\alpha\alpha} = P_{\beta\beta} = 1 - \sin^2(2\theta)\sin^2\left(\frac{\Delta m^2 L}{4E}\right) \tag{1.31}$$

that refers to the probability that a neutrino does not change its flavor after travelling a distance L (or, the probability that a neutrino of a given flavor does not disappear). When the appearance probability is maximum, the disappearance is minimum. Thus, for odd multiples of the length L_0, the disappearance probability is zero. Notice that in the literature, the argument of the oscillating sine function can be written in terms of the Δ parameter defined as

$$\Delta = \frac{\Delta m^2 L}{4E} \tag{1.32}$$

that, if we want to express Δm^2 in eV^2, L in km and E in GeV, corresponds to

$$\Delta = 1.27 \frac{\Delta m^2[eV]\, L[km]}{E\, [GeV]}. \tag{1.33}$$

1.1.4 Three flavors oscillations

The addition of one single flavor to the previous case makes the computation of the oscillation probabilities more complicated. Let us first give a look at the mixing matrix in the 3 flavors case. A 3×3 mixing matrix can be written in terms of three rotation angles and one complex phase, as already shown in section 1.1.1

$$\begin{aligned} U_{PMNS} &= \begin{pmatrix} 1 & 0 & 0 \\ 0 & c_{23} & s_{23} \\ 0 & -s_{23} & c_{23} \end{pmatrix} \begin{pmatrix} c_{13} & 0 & s_{13}e^{-i\delta} \\ 0 & 1 & 0 \\ -s_{13}e^{i\delta} & 0 & c_{13} \end{pmatrix} \begin{pmatrix} c_{12} & s_{12} & 0 \\ -s_{12} & c_{12} & 0 \\ 0 & 0 & 1 \end{pmatrix} \\ &= \begin{pmatrix} c_{12}c_{13} & s_{12}c_{13} & s_{13}e^{-i\delta} \\ -s_{12}c_{23} - c_{12}s_{23}s_{13}e^{i\delta} & c_{12}c_{23} - s_{12}s_{23}s_{13}e^{i\delta} & s_{23}c_{13} \\ s_{12}s_{23} - c_{12}c_{23}s_{13}e^{i\delta} & -c_{12}s_{23} - s_{12}c_{23}s_{13}e^{i\delta} & c_{23}c_{13} \end{pmatrix} \end{aligned} \tag{1.34}$$

where $s_{ij} = \sin\theta_{ij}$, $c_{ij} = \cos\theta_{ij}$ where δ=δ_{CP} is responsible for CP violation. It is clear that the full oscillation probabilities become very cumbersome since each term contains the product of four different mixing matrix entries. However, if one of the mass splittings is zero (or can be neglected) the general oscillation probability reduces to the two flavors one, where now θ is an effective mixing angle which can be written in terms of the three θ_{ij}. Moreover, also if one of the elements of the mixing matrix is zero, some of the probabilities can be simplified and written in terms of two-flavors oscillations. For instance, $s_{13} \ll 1$; thus, U_{e3} is very small. Neglecting it, we obtain that all the mixing matrices combinations which appear in eq. (1.46) where $\alpha = e$ and/or $\beta = e$ are zero. For this reason, all the probabilities which involve the electron flavor can be written in the form

$$P_{\alpha\beta} = \delta_{\alpha\beta} + [1 - 2\delta_{\alpha\beta}\sin^2(2\theta_{eff})]\sin^2\left(\Delta\frac{m^2_{21}L}{4E}\right). \tag{1.35}$$

Such equations can be used in some approximations and can be very useful, even though they are not exact and are not catching all the features of the 3-flavors oscillations. Another approximation that is used in some oscillations regimes, is the fast oscillation one. We will discuss later that one of the mass splittings (Δm^2_{31}) is bigger than the other (Δm^2_{21}). Thus, if we are observing oscillations driven by the latter, the ones driven by the former can be averaged out since they are very fast. Defining $K^{ij}_{\alpha\beta} = U_{\beta i}U^*_{\alpha i}U^*_{\beta j}U_{\alpha j}$, the oscillation probabilities become

$$\begin{aligned} P_{\alpha\beta} = \delta_{\alpha\beta} - 2\Re(K^{13}_{\alpha\beta} + K^{23}_{\alpha\beta}) - 4\Re(K^{12}_{\alpha\beta})\sin^2\left(\frac{\Delta m^2_{21}L}{4E}\right) \\ -2\Im(K^{12}_{\alpha\beta})\sin\left(\frac{\Delta m^2_{21}L}{2E}\right) \end{aligned} \tag{1.36}$$

which is much easier to handle than full probabilities. When we are at shorter distances, on the other hand, we can neglect the slow oscillations driven by Δm^2_{21} and we can choose a basis in which we observe two flavors oscillations between two neutrino states $\nu'_1 = \nu_e$ and $\nu'_3 = s_{23}\nu_\mu + c_{23}\nu_\tau$. The oscillation probabilities can be obtained from the two flavors one substituting the mixing angle with θ_{13} and the mass splitting with Δm^2_{31}.

It is worth to mention that, differently from the two flavors case, in the three neutrinos framework, due to the presence of the PMNS matrix phase, the CP symmetry cannot be conserved unless $\delta_{CP} = 0, \pi$. If we assume CPT conservation, however, we have that $\bar{P}_{\alpha\beta} = P_{\beta\alpha}$. We can therefore in principle define three different CP (or equivalently T) asymmetries as $P_{\alpha\beta} - P_{\beta\alpha} = P_{\alpha\beta} - \bar{P}_{\alpha\beta}$. However, the unitarity of the probabilities imposes that there exists only one independent asymmetry that can be written as

$$P_{\mu e} - P_{e\mu} = -4J\left[\sin\left(\frac{\Delta m^2_{32}L}{2E}\right) + \sin\left(\frac{\Delta m^2_{13}L}{2E}\right) + \sin\left(\frac{\Delta m^2_{21}L}{2E}\right)\right] \tag{1.37}$$

where J is the so called Jarlskog invariant defined as

$$J = c^2_{13}s_{13}s_{12}c_{12}s_{23}c_{23}\sin\delta \tag{1.38}$$

which encodes all the vacuum effects of the CP violation in the oscillations.

1.1.5 Measurements of oscillation parameters

Many neutrino oscillation experiments have been realized in the last 30 years. They used (and use) neutrinos from different sources to measure the six oscillation parameters θ_{12}, θ_{13}, θ_{23}, δ_{CP}, Δm^2_{21} and Δm^2_{31}. In particular, the categories of experiments which have been used so far to measure the oscillations parameters are: solar neutrinos experiment, atmospheric experiments, accelerator experiments and reactor experiments. The different types of neutrino oscillation experiments are traditionally classified based on the average value of L/E, which determines their sensitivity to a given Δm^2. Typical values of baselines, energy ranges, and corresponding sensitivity to Δm^2 are reported in Table 1.1.

Type of experiment	Baseline L	Energy E	Δm^2 sensitivity $[eV^2]$
Reactor SBL	~ 10 m	$\sim 1\,\text{MeV}$	~ 0.1
Reactor LBL	$\sim 1 - 100$ km	$\sim 1\,\text{MeV}$	$\sim 10^{-3} - 10^{-5}$
Accelerator SBL	$\sim 0.1 - 1$ km	$\geq 1\,\text{GeV}$	≥ 1
Accelerator LBL	$\sim 100 - 1000$ km	$\geq 1\,\text{GeV}$	$\sim 10^{-2} - 10^{-3}$
Atmospheric	$\sim 10 - 10^4$ km	$0.5 - 10^2\,\text{GeV}$	$\sim 10^{-3} - 10^{-4}$
Solar	$\sim 10^{11}$ km	$0.2 - 15\,\text{MeV}$	$\sim 10^{-12}$

Table 1.1: Types of neutrino oscillation experiments with their tipical source-detector distance, energy and sensitivity to Δm^2. The acronyms SBL and LBL stand for Short Baseline and Long Baseline, respectively.

The oscillation probabilities $P_{\alpha\beta}$ associated with channels where $\alpha \neq \beta$ are commonly referred to as transition probabilities. Conversely, the oscillation probabilities linked to channels where $\alpha = \beta$ are typically known as survival probabilities. Oscillation experiments follow a similar distinction, outlined in the following paragraphs.

Appearance experiments

They measure transitions between distinct neutrino flavors. If the final flavor to be detected is absent in the initial beam, the background noise can be effectively minimized. The primary signal sought in such experiments is the observation of a non-zero count of this different neutrino flavor. This configuration enables experiments to exhibit high sensitivity even to relatively small values of the mixing angle. Neutrino appearance experiments typically employ beams predominantly consisting of a single type of neutrino and aim to detect neutrinos of different flavors. However, their sensitivity is often hindered by uncertainties in the knowledge of beam contamination at the source. For instance, accelerator-generated muon-neutrino beams are not completely pure and contain a small fraction of electron neutrinos, typically around 1%, and particle identification in detectors may not be 100% efficient. On the other hand, the presence of tau neutrino contamination at the source is negligible, as observed by the OPERA experiment [21]. However, the sensitivity of muon-to-tau neutrino appearance experiments is limited either by statistical constraints or by the ability to accurately identify tau particles. In practice, appearance experiments using an accelerator-generated muon-neutrino beam are always disappearance experiments as well: this is due to the similarity between the squared mass differences Δm^2_{32} and Δm^2_{31}. Consequently, an experiment designed to observe the appearance of electron or tau neutrinos will also possess sensitivity to the disappearance of muon neutrinos. For example, the OPERA experiment used a muon-neutrino beam produced by CERN Neutrinos to Gran Sasso (CNGS) facility. Despite the appearance of ν_τ being its primary goal, OPERA was also sensitive to the disappearance of ν_μ during their propagation. Accelerator experiments that produced crucial results by studying muon (anti)neutrino disappearance and electron (anti)neutrino appearance are, for example, the MINOS (Main Injector Neutrino Oscillation Search) [22] and the T2K (Tokai to Kamioka) [23] experiments.

Disappearance experiments

These are designed to measure the survival probability of a neutrino flavor. The distinctive oscillation signal manifests as a deficit in the observed event count. However, due to statistical fluctuations inherent in the number of detected events, even in the absence of oscillations, uncovering a subtle disappearance becomes challenging. Reactor neutrino experiments are always disappearance experiments, because the energies of the produced electron antineutrinos, typically of the order of few MeV, are not sufficient to create muons or taus, and therefore ν_μ and ν_τ cannot be seen in charged-current reactions. For low-energy neutrinos, the only viable approach for conducting appearance experiments is through a direct comparison between neutral-current and charged-current reactions, as done by the Sudbury Neutrino Observatory (SNO) experiment [24]. Disappearance experiments have yielded significant results in the study of neutrino oscillations. SNO provided compelling evidence for neutrino oscillations and confirmed the existence of the phenomenon. It observed a deficit in the number of solar electron neutrinos compared to expectations based on solar models. This deficit indicated that electron neutrinos from the Sun had oscillated into other neutrino flavors during their journey to Earth . The KamLAND (Kamioka Liquid Scintillator Antineutrino Detector) experiment [25] similarly observed a deficit in the number of electron antineutrinos emitted by nuclear reactors, providing further confirmation of neutrino oscillations. The Borexino experiment played a key role in the field by performing direct measurements of solar electron neutrinos survival probability [26]. The Daya Bay [27] and RENO (REactor Neutrino Oscillation) [28] experiments provided precise measurements of the mixing angle θ_{13}, determining its non-zero value.

1.1.6 Neutrino Mass Ordering

Neutrino oscillation experiments are only sensitive to the squared mass differences Δm^2_{ij}, but not to the absolute mass scale. Thanks to matter effects in the Sun, we know that $\Delta m^2_{21} > 0$. Contrariwise, the sign of Δm^2_{31}, or equivalently Δm^2_{32}, still remains undetermined. As a consequence, there are two possible scenarios for the mass ordering (MO):

- **Normal Ordering (NO)**: $\Delta m^2_{31} > 0$.
- **Inverted Ordering (IO)**: $\Delta m^2_{31} < 0$.

The two mentioned hierarchical neutrino mass spectra are shown in Figure 1.2, providing a graphical representation of the neutrino flavor content of each mass eigenstate. Its determination thus relies on the precise measurement of Δm^2_{31} and Δm^2_{32} and can be experimentally addressed via different techniques:

(1) Long baseline (LBL) accelerator experiments

(2) Atmospheric neutrino experiments

(3) Medium baseline reactor experiments (i.e., JUNO [29])

Matter effects introduce discrepancies in the oscillation probabilities for neutrinos and antineutrinos: in the case of NO, the electron neutrino appearance is enhanced and the electron antineutrino appearance is suppressed (while for IO the configuration is opposite), thus manifesting as an effective pseudo CP-violating effect. In LBL beam experiments, the sensitivity to the matter effect relies on the appearance channel, specifically the transitions $\nu_\mu \to \nu_e$ and $\bar{\nu}_\mu \to \bar{\nu}_e$. However, it is important to note that LBL experiments are also sensitive to the genuine CP-violating phase, making it nontrivial to distinguish the asymmetry caused by CP violation and the different mass orderings. A similar approach, based on the MSW effect, is

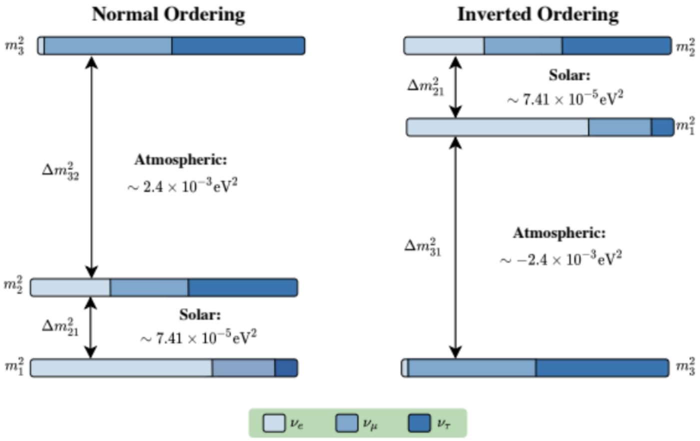

Figure 1.2: *The two possible neutrino mass ordering scheme*

pursued by atmospheric neutrino experiments, which exploit (anti)neutrinos with a wide range of baselines ($\sim$ 10 - 104 Km) and energies. In contrast, JUNO stands out as the only experiment currently capable of resolving the mass ordering through dominant vacuum oscillations. This unique characteristic grants JUNO unparalleled insight and capability in the study of mass ordering within the neutrino oscillation framework. JUNO's MO sensitivity relies on high-precision spectral analysis of reactor antineutrinos, that will be discussed in section 1.2.

1.1.7 Latest results on mixing parameters

As shown in equation 2.41 the neutrino oscillation is parametrized by three angles, a phase and two quadratic mass differences of the neutrino eigenstates. Table 1.2 shows the latest global fit results on data as of September 2024 from NuFit [30], for normal ordering and inverted ordering. For each hypothesis a best-fit point (bfp) as well as the 1σ and the 3σ ranges are given. The data includes Super-Kamiokande [31], IceCube/DeepCore [32], MINOS, NOνa [33], T2K , KamLand, Borexino, SNO, Daya Bay, RENO and DoubleChooz [34] to name a few. The parameters Δm_{21}^2 and θ_{12} are commonly referred to as the *solar parameters*. Similarly, the parameters Δm_{3l}^2 and θ_{23} are known as the *atmospheric parameters*.

	Normal Ordering		Inverted ordering	
	Best fit ±1σ	3σ range	Best fit ±1σ	3σ range
$\sin^2\theta_{12}$	$0.308^{+0.012}_{-0.011}$	$0.275 \to 0.345$	$0.308^{+0.012}_{-0.011}$	$0.275 \to 0.345$
$\theta_{12}/^\circ$	$33.68^{+0.73}_{-0.70}$	$31.63 \to 35.95$	$33.68^{+0.73}_{-0.70}$	$31.63 \to 35.95$
$\sin^2\theta_{23}$	$0.470^{+0.017}_{-0.013}$	$0.435 \to 0.585$	$0.550^{+0.012}_{-0.015}$	$0.440 \to 0.584$
$\theta_{23}/^\circ$	$43.3^{+1.0}_{-0.8}$	$41.3 \to 49.9$	$47.9^{+0.7}_{-0.9}$	$41.5 \to 49.8$
$\sin^2\theta_{13}$	$0.02215^{+0.00056}_{-0.00058}$	$0.02030 \to 0.02388$	$0.02231^{+0.00056}_{-0.00056}$	$0.02060 \to 0.02409$
$\theta_{13}/^\circ$	$8.56^{+0.11}_{-0.11}$	$8.19 \to 8.89$	$8.59^{+0.11}_{-0.11}$	$8.25 \to 8.93$
$\delta_{CP}/^\circ$	212^{+26}_{-41}	$124 \to 364$	274^{+22}_{-25}	$201 \to 335$
$\frac{\Delta m^2_{21}}{10^{-5}eV^2}$	$7.49^{+0.19}_{-0.19}$	$6.92 \to 8.05$	$7.49^{+0.19}_{-0.19}$	$6.92 \to 8.95$
$\frac{\Delta m^2_{3l}}{10^{-3}eV^2}$	$+2.513^{+0.021}_{-0.019}$	$+2.451 \to +2.578.95$	$-2.484^{+0.020}_{-0.020}$	$-2.547 \to -2.421$

Table 1.2: Table of latest global fit results on neutrino parameters by NuFit 2024.

1.2 Reactor Neutrinos

Nuclear reactors are intense, isotropic sources of electron antineutrinos, produced through the β-decays of fission secondaries $n \to p + e^+ + \bar{\nu}_e$. To accurately predict the reactor $\bar{\nu}_e$ energy spectrum, several factors must be taken into consideration, including the source, interaction, and subsequent detection of the involved particles. The source of interest in this context is the reactor antineutrino flux.

1.2.1 Reactor antineutrino flux

In the case of modern pressurized water reactors (PWRs), antineutrinos are emitted by the fission fragments of mainly four isotopes: two Uranium isotopes, ^{235}U and ^{238}U, and two Plutonium isotopes, ^{239}Pu and ^{241}Pu. These isotopes contribute over 99% of the thermal power and total neutrino flux. The antineutrino flux at time t is predicted by:

$$\phi(E_{\bar{\nu}_e}, t) = \sum_r \frac{P_{\bar{\nu}_e \to \bar{\nu}_e(E_{\bar{\nu}_e}, L_r)}}{4\pi L_r^2} \frac{W_r(t)}{\sum_i f_{ir}(t) e_i} \sum_i f_{ir}(t) s_i(E_{\bar{\nu}_e}), \tag{1.39}$$

where r is the reactor index, $P_{\bar{\nu}_e \to \bar{\nu}_e(E_{\bar{\nu}_e}, L_r)}$ is the $\bar{\nu}_e$ survival provability of the electron antineutrino (obtainable from the general expression in eq 1.46) at a distance L_r from reactor r, $W_r(t)$ is the reactor thermal power, $f_{ir}(t)$ is the fission fraction of one isotope i among the four previously discussed, e_i is

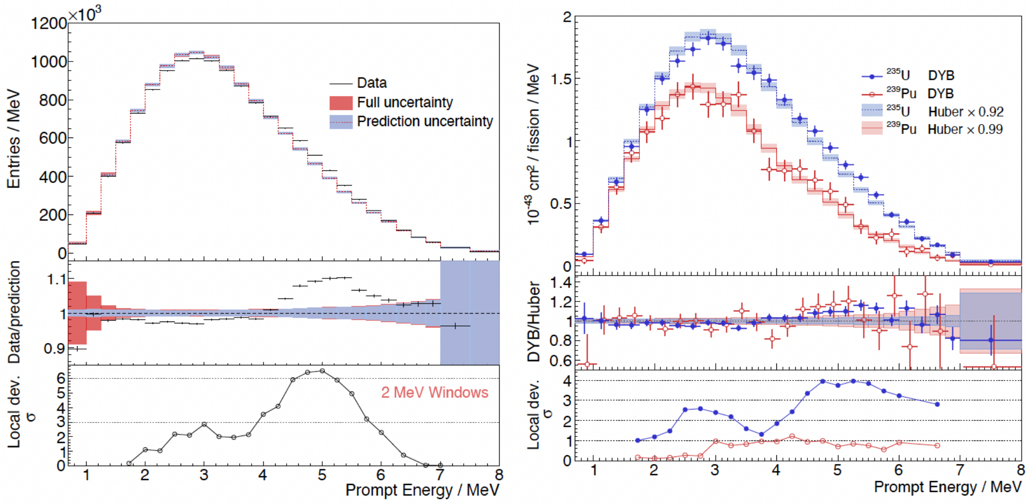

Figure 1.3: *The figure compares the observed reactor antineutrino spectrum to Huber-Mueller model predictions. The Left panel shows the predicted and measured prompt energy spectra. On the right panel the extracted spectra of* ^{235}U *and* ^{239}Pu *is compared to model predictions (using best-fit normalization factors (0.92 and 0.99)). Figures are taken from Daya Bay [41]*

the mean energy released per fission for isotope i, and $s_i(E_{\bar{\nu}_e})$ is the antineutrino energy spectrum per fission for each isotope. The energy spectrum per fission for each isotope has been estimated in literature [35, 36] by two main approaches. One is the summation method [37, 36] which sums all the antineutrino energy spectra corresponding to thousands of beta decay branches for about 1000 isotopes in the fission products, with information in nuclear databases. The other method is the beta conversion method [35, 38] which converts the measured β energy spectra from the individual fission isotopes ^{235}U, ^{238}U, ^{239}Pu, and ^{241}Pu to the corresponding antineutrino energy spectra using a set of virtual beta spectra. The most known conversion model is the Hubert-Mueller method [39, 40], and is the most used model for the theoretical estimation of the energy spectrum per fission.

1.2.2 Reactor antineutrino anomalies

The observed antineutrino yield per fission shows a $\sim 5\%$ deficit compared with the model predictions, which is referred to as the reactor antineutrino anomaly (RAA) [42]. The recent reactor antineutrino experiments, Daya Bay, RENO, Double Chooz and others confirmed the reactor antineutrino anomaly and observed a new discrepancy in the Huber-Mueller model predictions. Specifically, an excess of neutrino events around 5 MeV, the so-called reactor bump, is observed [43]. Figure 1.3 shows the prompt energy spectrum compared with the model predictions at the Daya Bay experiment. The plot shows a comparison of measured and predicted prompt energy spectra indicating the observed deficits. The obtained spectrum and its prediction by the Huber-Mueller model together with uncertainties are displayed in the left panel. The ratio of the measured-to-predicted spectra and the deviation from the local mean are pointed out, respectively, in the middle and in the bottom regions of the left panel. The right panel of the figure shows the obtained ^{235}U and ^{241}Pu spectra compared to Huber-Muller model predictions, with the best normalization factors to match shapes. The lower and middle panels on the right show the extracted-to-predicted ratio of spectra and local deviations for each isotope respectively. The figure shows deficit of the observed fluxes, particularly around 5 MeV where an excess of antineutrinos. To address this issue the reactor antineutrino experiments use near detectors that can provide a reference spectrum. However, the current resolutions obtained from them are insufficient to address the fine structure. This is one of the primary goal of the Taishan Antineutrino Observatory [44], to provide a precise antineutrino energy spectrum with unprecedented energy resolution that can aid in understanding reactor anomalies and neutrino physics.

1.2.3 Reactor antineutrino detection

Reactor antineutrinos in liquid scintillator experiments like JUNO are detected through the Inverse Beta Decay (IBD), $\bar{\nu}_e + p \to n + e^+$, specifically by measuring the produced positron energy spectrum, since it retains almost all of the incoming antineutrino kinetic energy. The electron antineutrino interacts with a proton (p) in the liquid scintillator, generating a positron (e^+) and a neutron (n). The positron quickly deposits its energy and annihilates into two 0.511 MeV photons, producing a prompt signal containing both the positron kinetic energy T_{e^+} and the 1.022 MeV annihilation energy. The neutron then makes a random walk and is thermalized in the detector medium by successive scattering events after an average time of $220\mu s$. It is finally captured either by a free proton in the LS ($\sim$ 99% probability) or by carbon ($\sim$ 1%), subsequently emitting a 2.22 MeV or 4.95 MeV γ-ray, respectively, and giving rise to a delayed signal. As we will see in detail later, in the Taishan Antineutrino Observatory we have a different scenario for neutron capture and consequently for delayed signal, since TAO liquid scintillator is doped with a small fraction of Gadolinium which changes the average capture time and the emitted photon energy. A sketch, depicting the general IBD kinematics from the emission of both particles to their annihilation or

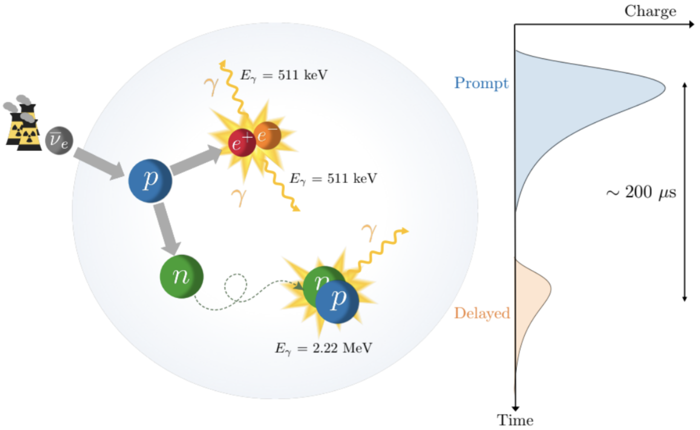

Figure 1.4: *Schematic illustration of an IBD reaction in the LS. The electron antineutrino interacts with a proton* (p) *in the LS, creating a positron* (e^+) *and a neutron* (n)*. The positron deposits its energy and annihilates into two* 0.511 *MeV photons* (γ)*, producing a prompt signal. After a random walk, the neutron is captured mainly by a free proton in the LS, emitting a* 2.22 *MeV* γ*-ray, and giving rise to a delayed signal. The time-charge diagram is not in scale.*

capture, is shown in Figure 1.4. The IBD kinematical threshold is roughly 1.8 MeV. In the IBD reaction the incident antineutrino energy $E_{\bar{\nu}_e}$ is given by:

$$E_{\bar{\nu}_e} \simeq T_{e^+} + T_n + \Delta_{np} + m_{e^+}, \tag{1.40}$$

where T_{e^+} and T_n are the positron and neutron kinetic energies, $\Delta_{np} = m_n - m_p = 1.293$ MeV is the mass difference between neutron and proton, and m_{e^+} is the positron mass. T_n ranges from 0 to tens of KeV, thus the neutron recoil energy is often considered to be fairly negligible with respect to the $O(1MeV)$ energy scales of the reaction. Under this recoilless approximation, the positron energy is directly related to the antineutrino energy, i.e., $E_{\bar{\nu}_e} \simeq E_{e^+} + \Delta_{np}$ [45], with $E_{e^+} = T_{e^+} + m_{e^+}$. The deposited energy ($E_{dep}$) for the IBD prompt signal is thus defined as the sum of the positron kinetic energy T_{e^+} and the annihilation energy generating two 0.511 MeV photons:

$$E_{dep} = T_{e^+} + 2 \times 0.511MeV = E_{e^+} + m_{e^+} \tag{1.41}$$

As a result, $E_{e^+} + m_{e^+} \sim E_{\bar{\nu}_e} - 0.782MeV$, or equivalently:

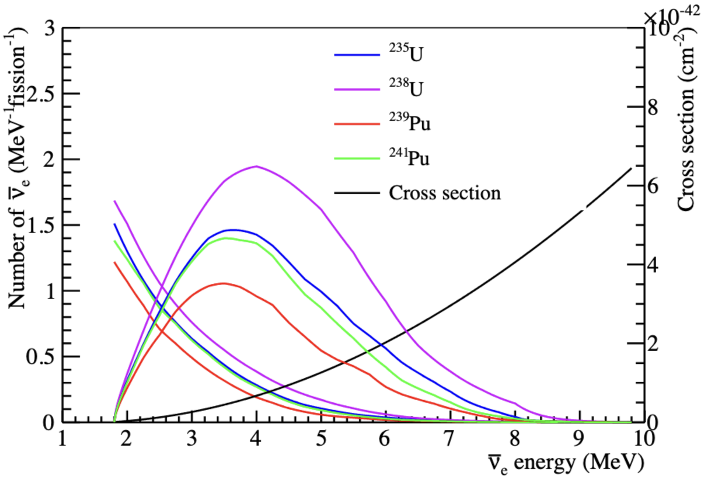

Figure 1.5: *Antineutrino energy spectrum per fission in a commercial reactor weighted by the inverse beta decay cross section*

$$E_{dep} \simeq E_{\bar{\nu}_e} - 0.782 MeV \tag{1.42}$$

E_{dep} is assumed to be fully deposited in the detector since energy losses due to escaping secondary particles generated by Compton scattering and pair production only affect less than 1% of the IBD events. Therefore, the measured positron spectrum corresponds to the antineutrino spectrum, shifted in energy and weighted by the IBD differential cross section $\frac{d\sigma}{d\cos\theta}(E_{\bar{\nu}_e}, \cos\theta)$, which is a function of the neutrino energy and the scattering angle [46], and accounts for the interaction probability. The detectable reactor electron antineutrino spectrum is depicted in Figure 1.5 as a convolution of the IBD cross-section [46] and the flux of the $\bar{\nu}_e$ (based on Hubert-Muller model).

Chapter 2

The JUNO–TAO Experiment

The Jiangmen Underground Neutrino Observatory (JUNO) [47], is a multipurpose liquid scintillator (LS) detector currently taking data in the Guandong province in South China. JUNO has been designed primarily for the determination of the neutrino mass ordering with reactor antineutrinos $\bar{\nu}_e$, emitted from the Taishan and Yangjiang nuclear power plants (NPPs), both located at a baseline of about 52.5 km from the experimental site. To resolve the fine oscillation structure necessary for determining the NMO, JUNO has been designed to achieve an energy resolution of 3% at 1 MeV [48], unprecedented for a detector of this scale. In order to achieve accurate results, JUNO relies on precise knowledge of the unoscillated reactor antineutrino spectrum shape. To accomplish this, a dedicated satellite detector called Taishan Antineutrino Observatory [44] (TAO or JUNO-TAO) has been installed at a distance of 44 m from one of the Taishan reactors, and it is currently finishing the commissioning phase. TAO will measure the spectrum with a record energy resolution below the 2% at 1 MeV, serving as a data-driven reference to constrain the spectra of the other reactor cores. Figure 2.1 shows a schematic that illustrates the location of JUNO and TAO. In this chapter the JUNO and TAO experiments will be described, with particular focus on the latter. In the first section a general overview of the JUNO experiment will be provided. Then in the following sections several topics about the TAO experiment will be covered: the physics goals, the design of the detector, signals and backgrounds and energy resolution.

Figure 2.1: *Location of the JUNO and TAO experiments in South China. The main 20 kton LS detector, JUNO, is located 700 m underground at a baseline of* ~ 52.5 *km from six 2.9 GW thermal power (GWth) reactor cores in the Yangjiang NPP and two 4.6 GWth cores in the Taishan NPP. The 2.8 ton JUNO-TAO detector is located about* 44 *meters away from one of the Taishan reactor cores.*

2.1 The JUNO Experiment

With its 20kt of liquid scintillator as a target for neutrino detection, JUNO is the largest LS detector ever built. The installation of the detector was completed in August 2025, and, after a period of commissioning, it started the data acquisition the 26th of August. As shown in Figure 2.2, JUNO detector components include a Central Detector (CD), a water Cherenkov detector and the Top Tracker (TT). The Central Detector is the key component of the JUNO detector, serving the purpose of detecting physics events covering the experiment's comprehensive physics program [47], including reactor, solar, atmospheric and supernovae neutrinos and antineutrinos. The CD is a 35.4 m diameter acrylic sphere, supported by a 40.1 m diameter Stainless Steel (SS) structure, containing 20 kton of liquid scintillator. The recipe of the LS is a very important factor for the performance of the detector. It contains linear alkylbenzene (LAB) as a solvent, due to its excellent transparency, high flash point, and low chemical reactivity and good light yield. In addition, the LS contains 2.5 g/L 2,5-diphenyloxazole (PPO) as the fluor and 3 mg/L p-bis-(o-methylstyryl)-benzene (bis-MSB) as wavelength shifter. To achieve the unprecedented energy resolution (for a LS-based experiment) of $3\%/\sqrt{E(MeV)}$, the detector incorporates a sophisticated photo-detection

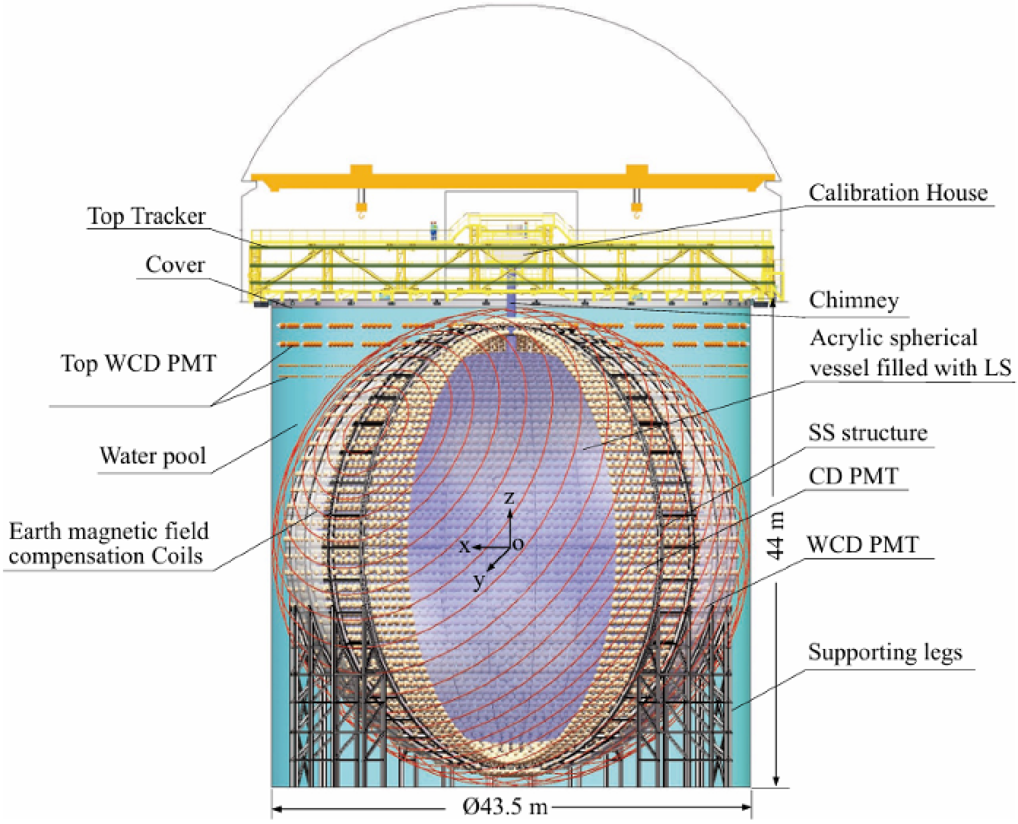

Figure 2.2: *Schematic of the main JUNO detector. An acrylic sphere filled with 20 kton of liquid scintillator is immersed in a water tank and surrounded by 17612 large (20-inch) and 25600 small (3-inch) PMTs, the LPMTs and sPMT systems respectively. The water pool is instrumented with 2400 20-inch PMTs providing shielding and cosmic-ray muon tagging. A top tracker system consisting of three layers of plastic scintillator covers about* 60% *of the surface above the water pool and provides precision tracking of cosmic-ray muons entering the central detector. On top of the CD there is the Calibration House.*

system consisting of 17612 20-inch (or Large) photomultiplier tubes (PMTs) and 25600 3-inch (or Small) PMTs. These PMTs point inward and are attached to the surrounding SS structure. This configuration provides an extensive total photo-coverage of $\sim 78\%$, granting a high photoelectron (PE) statistics of about 1400 PE / MeV. To decrease muon-induced backgrounds, the CD is located in an experimental hall with approximately 690 m of rock overburden (1800 meters-water-equivalent), which provides natural shielding from cosmic rays. Nevertheless, due to the large size of the detector, the residual muon rate is still high, amounting to approximately $0.004 Hz/m^2$. For this reason, the experiment is equipped with two veto systems acting as efficient taggers for cosmic muons. The CD is housed within a cylindrical water pool (WP), with a height of 44 m and a diameter of 43.5 m, filled with 35 kton of ultra-pure water. The WP is instrumented with 2400 20-inch PMTs attached to the outer part of the SS shell and pointing outwards, thereby acting as a Cherenkov veto detector for cosmic muons. Furthermore, a water buffer connected to the outer Cherenkov detector acts as a shielding layer for the natural radioactivity of the surrounding rock. The second muon veto system , the Top Tracker, is placed on top of the WP. It consists of plastic scintillator strips from the Target Tracker of the OPERA experiment [21] arranged in three horizontal layers. The TT is centrally placed on top of the WP, covering about 60% of the top surface of the JUNO CD. A chimney connects the CD to the outside and will be used to deploy calibration sources into the detector. The calibration operations are carried out in the Calibration House.

The main goal of JUNO is to determine the NMO up to 3σ within 6 years of data collection, and to measure the oscillation parameters with precision below 1%. The analysis procedure is to detect the energy dependent reactor electron antineutrino oscillation spectrum from the associated power plants with a 52.5 km baseline, focusing on electron antineutrino disappearance. As discussed in section 1.2.3, neutrino detection occurs through IBD reaction, which for reactor $\bar{\nu}_e$ has a rate of 60 IBDs/day in JUNO. Starting from Eq. 1.46, the $\bar{\nu}_e$ survival probability in JUNO is the following:

$$P(\bar{\nu}_e \to \bar{\nu}_e) = 1 - \sin^2 2\theta_{13}(\cos^2\theta_{12}\sin^2\Delta_{31} + sin^2\theta_{12}\sin^2\Delta_{32}) - \cos^4\theta_{13}\sin^2 2\theta_{12}\sin^2\Delta_{21}, \quad (2.1)$$

where $\Delta_{ij} \equiv \frac{\Delta m^2_{ij} L}{4E}$. The expected reactor antineutrino spectra for the different mass orderings are shown in Figure 2.3. Therefore, in JUNO's location, the energy spectrum will be distorted by a slow (low frequency) oscillation driven by Δm^2_{21} and modulated by $sin^2 2\theta_{12}$, as well as by a fast (high frequency) oscillation regulated by Δm^2_{31} and modulated by $sin^2 2\theta_{13}$. To able to extract the information on the mass ordering, a resolution as or better than the size of $\frac{\Delta m^2_{31}}{|\Delta m^2_{31}|}$ is required [48]. Therefore, the existing energy resolution may not be sufficient to accurately measure the oscillation probabilities of reactor antineutrinos and solve the NMO with 3σ. These probabilities are sensitive to the reactor antineutrino flux and spectrum, which can be subject to significant uncertainties. Some of these uncertainties arise from differences in the nuclear processes that lead to the production of antineutrinos, and others are due to the current model limitations that predict the antineutrino spectrum from reactors. In addition, the capability of resolving the neutrino mass ordering relies on the precise measurement of the fine oscillatory pattern imprinted in the reactor antineutrino energy spectrum. Several sources of uncertainty can affect this measurement. The most critical one is the detector energy resolution, which must be sufficiently small to resolve the interference pattern generated by the oscillation terms driven by Δm^2_{31} and Δm^2_{32}. Uncertainties related to the absolute energy scale and possible nonlinearities in the detector response may also distort the reconstructed spectrum. Finally, the precision with which the oscillation parameters are known, as well as the presence of residual backgrounds, can further affect the determination of the mass ordering.

To help address these challenges, the Taishan Antineutrino Observatory will play a fundamental role [49], as we will see in detail in the next section. TAO is designed to perform high-precision measurement of the reactor antineutrino spectrum directly from the Taishan Nuclear Power Plant, with an energy resolution better than 2% at 1 MeV. The accurate understanding of the antineutrino spectrum allows for better characterization of oscillation effects thereby improving the sensitivity of JUNO in determining the NMO.

Beyond the determination of the mass ordering, achieving such a level of precision in the measurement of oscillation parameters also has broader implications for neutrino physics. In particular, high-precision measurements of parameters such as $sin^2\theta_{12}$ and Δm^2_{21} provide stringent tests of the standard three-flavor oscillation framework and of the internal consistency of the PMNS mixing paradigm. Measurements at the percent or sub-percent level allow global analyses to verify the compatibility among different experimental results and to search for possible deviations from the expected oscillation pattern. Improving the experimental precision well beyond the current level also reduces parameter degeneracies and enhances the sensitivity of other neutrino oscillation experiments. In this context, pushing the uncertainty on oscillation parameters from the order of ten percent to the percent or sub-percent level opens the possibility of probing subtle effects that could

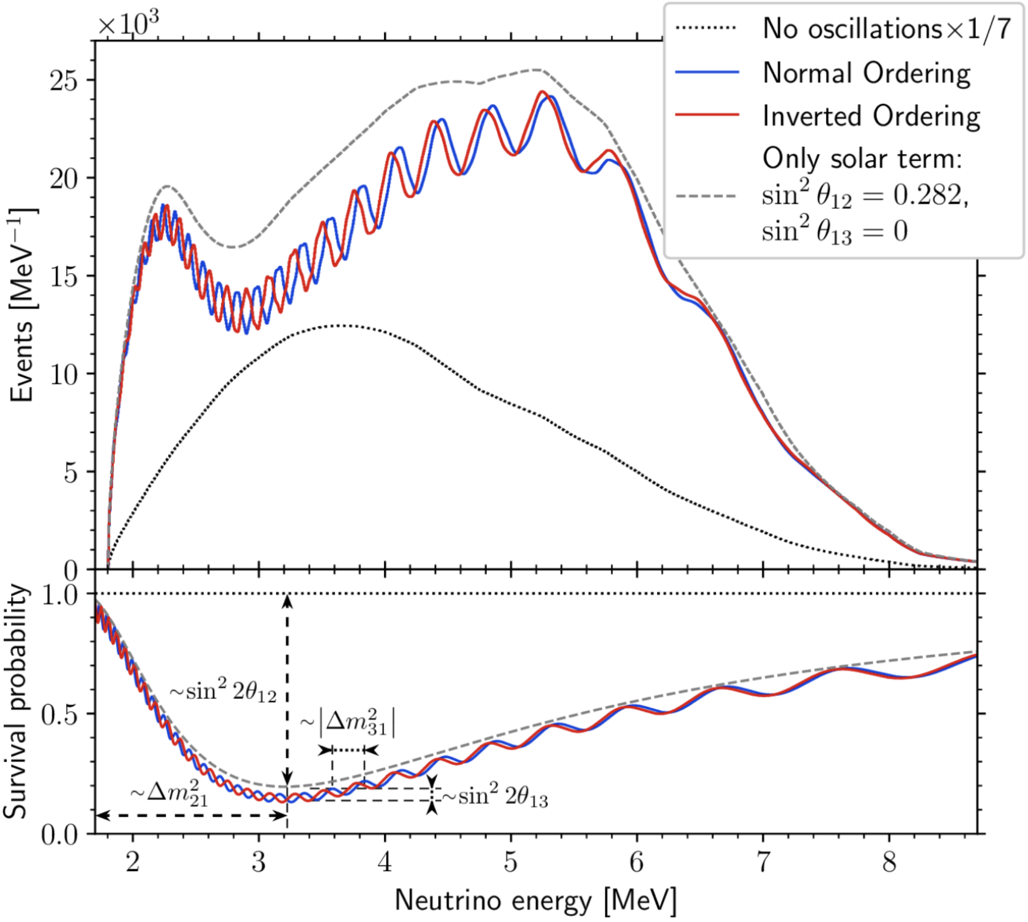

Figure 2.3: *Spectrum of reactor electron anti-neutrinos and the respective survival probability for JUNO from associated power plants, within 6 years of data taking, from the JUNO collaboration. The black dotted line displays the unoscillated reactor electron anti-neutrino spectrum with a factor of 1/7, while the blue and red line show the oscillated results with NO and IO. The gray dashed line represents the spectrum only taking the solar term into account. Additionally, the influence of the oscillation parameters* $sin^2 2\theta_{12}$, $sin^2 2\theta_{13}$, Δm^2_{21}, Δm^2_{31} *is also shown.*

reveal limitations of the standard three-neutrino description. In addition, several extensions of the Standard Model predict the existence of additional neutrino states that do not interact through the weak interaction, commonly referred to as sterile neutrinos. If such states exist and mix with the three active neutrinos, they would modify the standard oscillation pattern by introducing additional oscillation frequencies and distortions in the observed energy spectrum. Precision measurements of reactor antineutrino spectra therefore provide a powerful tool to probe these scenarios. Deviations from the expected spectral structure, or inconsistencies in the determination of oscillation parameters across different experiments, could represent indirect evidence for the presence of sterile neutrinos or other new physics effects beyond the Standard Model.

Since the beginning of data acquisition, the 26th of August 2025, with just 59.1 effective days of data taking (corresponding to 69 calendar days), JUNO already managed to perform a measurement of the solar oscillation parameters $sin^2\theta_{12}$ and Δm^2_{21} with world leading precision [50], showcasing the detector's incredible performances. The oscillation analysis yielded the following results for the solar parameters for normal mass ordering scenario:

- $sin^2\theta_{12} = 0.3092 \pm 0.0087$
- $\Delta m^2_{21} = (7.50 \pm 0.12) \times 10^{-5} eV^2$

This incredible result yields the most precise and simultaneous measurement of solar oscillation parameters Δm^2_{21} and $sin^2\theta_{12}$ to date, improving the precision of both parameters by a factor of 1.6 relative to the combination of all previous measurements. The measured energy spectrum is shown in Figure 2.4 and the results of solar oscillation parameters are shown in Figure 2.5.

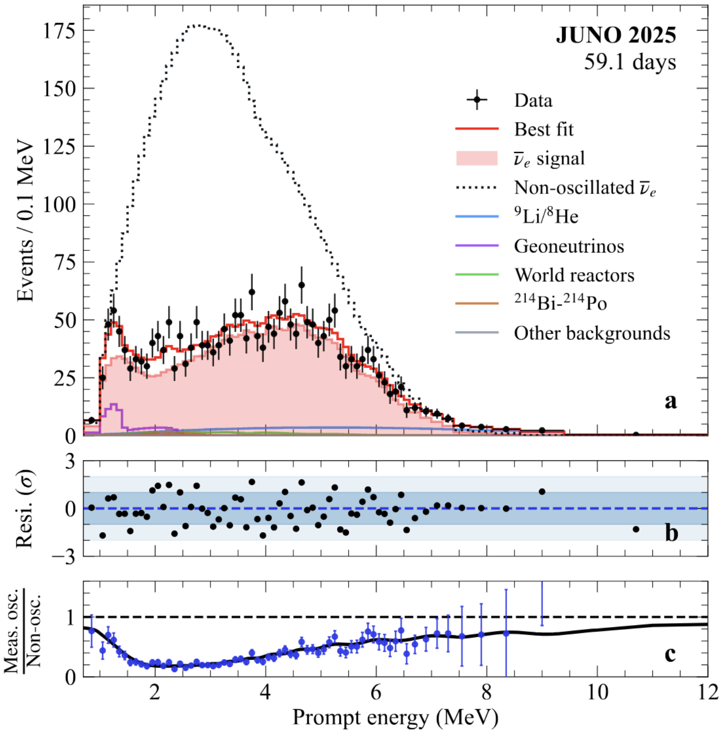

Figure 2.4: **Measured energy spectrum of prompt IBD candidates. a,** *Black points show measured data with statistical error bars, with the red curve indicating the best-fit oscillation model. Shaded red region represents expected antineutrino signal. Black dotted line represents non-oscillated reactor neutrino expectation. Backgrounds are indicated by other solid color lines.* **b,** *Residuals quantifying the statistical consistency between data and the complete model.* **c,** *Ratio of the measured oscillated spectrum to non-oscillated prediction.*

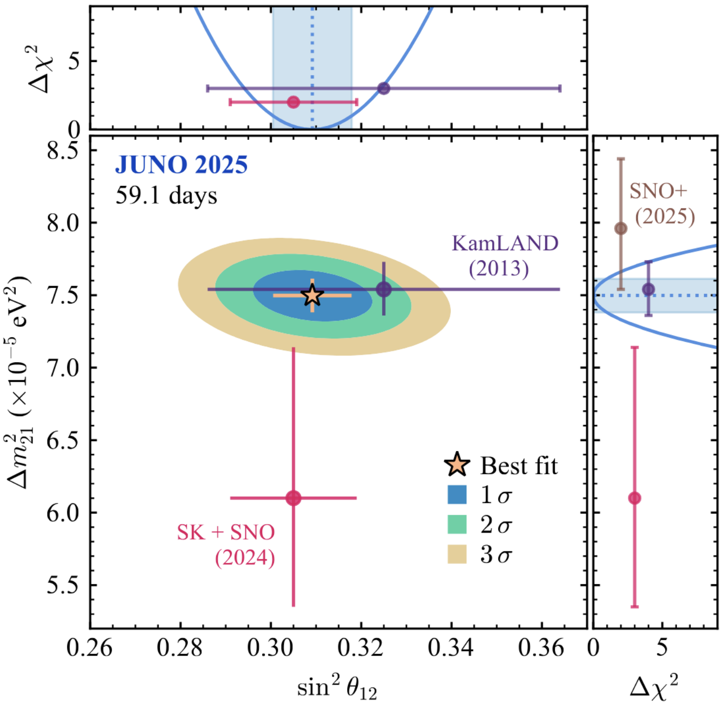

Figure 2.5: **Results on solar oscillation parameters:** *Confidence intervals of sin*$^2\theta_{12}$ *and* Δm^2_{21} *from a spectral fit of measured prompt antineutrino energy spectrum shown in Figure 2.5. Shaded elliptically-shaped areas correspond to* 1σ, 2σ, *and* 3σ *confidence levels. The upper panel provides the one dimensional* $\Delta\chi^2$ *for sin*$^2\theta_{12}$ *obtained by profiling* Δm^2_{21} *(blue line) and the blue shaded region as the corresponding* 1σ *interval. The right panel is the same, but for* Δm^2_{21}, *with sin*$^2\theta_{12}$ *profiled. The star marks the best fit values of JUNO, and the error bars show their one-dimensional* 1σ *confidence intervals. Results from other measurements of reactor neutrinos (KamLAND and SNO+) and solar neutrinos (combined SuperKamiokande+SNO) are shown for comparison.*

2.2 The TAO Experiment

The Taishan Antineutrino Observatory [44] (TAO, also known as JUNO-TAO) is a satellite experiment of the Jiangmen Underground Neutrino Observatory (JUNO) [47]. TAO consists of a spherical ton-level Gadolinium-doped Liquid Scintillator (Gd-LS) detector of 1.8 m diameter, placed at ~ 44 meters from one reactor core (TS-C1) of the Taishan Nuclear Power Plant. To fully contain the energy deposition of gammas from the IBD positron annihilation, a 25 cm selection cut is applied, resulting in 1 ton of fiducial mass. By means of 10 m^2 of Silicon Photomultipliers (SiPMs), resulting in $\sim 95\%$ coverage, operating at a temperature of $-50\,^{\circ}\mathrm{C}$, TAO aims to reach an energy resolution below the 2% at 1 MeV, approaching the limit of LS detectors. The detector installation was completed in November and is currently finishing the commissioning phase.

2.2.1 Physics goals

The TAO experiment will deliver a precise antineutrino energy spectrum measurement with unprecedented energy resolution, providing new and important data. With this new data, TAO can achieve several physics goals:

- Measurement of a high-resolution antineutrino energy spectrum, which serves as a benchmark to test nuclear databases, provides increased reliability in measured isotopic antineutrino yields, and gives an opportunity to improve nuclear physics knowledge of neutron-rich isotopes
- Provide the reference spectrum for JUNO to reduce the model dependence on the reactor antineutrino spectrum;
- Search for light sterile neutrinos with a mass scale around 1 eV;
- Reactor monitoring for reactor status and fuel.

Fine structure measurement

In a reactor, the energy spectrum of antineutrinos arise from multiple beta decay branches, each exhibiting a sharp edge due to Coulomb correction. These corrections create sharp edges in the spectra as they distort the beta decay branches due to electromagnetic interaction between the emitted beta particle and their daughter nucleus's charge, modifying the particle's energy distribution. This creates fine structure in the spectrum. Figure 2.6 illustrates this with clear cutoffs at decay branch edges of the listed fission products calculated using summation method. However, the exact shape and

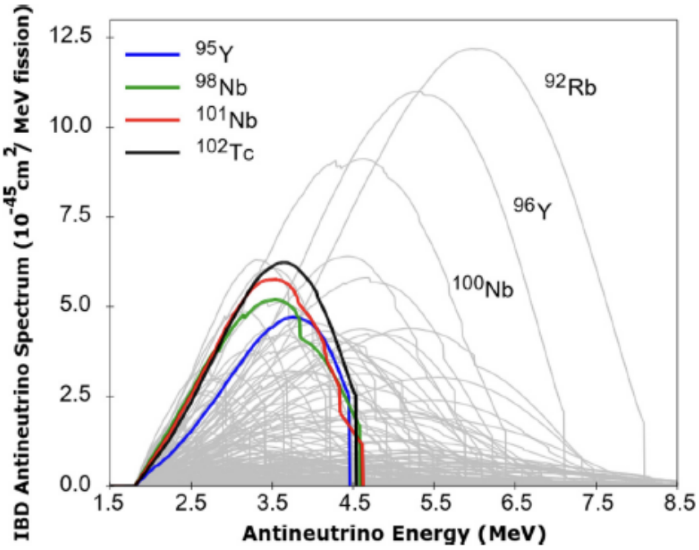

Figure 2.6: *Calculated antineutrino energy spectra from many fission products in a commercial reactor [51]*

amplitude of this fine structure remains challenging due to limited data owing to the low event rates and the fluctuations introduced from the reactor operations. The TAO experiment will provide a benchmark to validate the summation spectrum calculation. A statistical uncertainty below 1% in the energy range of 2.5 − 6 MeV will allow to constrain the fine structure to better than 1%.

Reference spectrum for JUNO

TAO will provide a precise reference spectrum for JUNO with resolution $< 2\%$, and the event rate will be ~ 20 times higher than JUNO because of the short baseline of 44 m. TAO has the capability to accurately map its measured spectrum onto the expected unoscillated spectrum in JUNO, considering detector effects such as energy resolution. This mapping enables the direct application of TAO reference spectrum to JUNO without requiring prior knowledge of the underlying neutrino spectrum [49]. Using TAO spectrum as input, the predicted antineutrino energy spectrum for JUNO without oscillations can be expressed as:

$$S_{JUNO}(E_\nu) = S_{TAO}(E_\nu) + \sum_i \Delta f_i S_i(E_\nu), \tag{2.2}$$

where $S_{TAO}(E_\nu)$ is the reference antineutrino energy spectrum from TAO, Δf_i is the difference of fission fractions for the four major isotopes, and

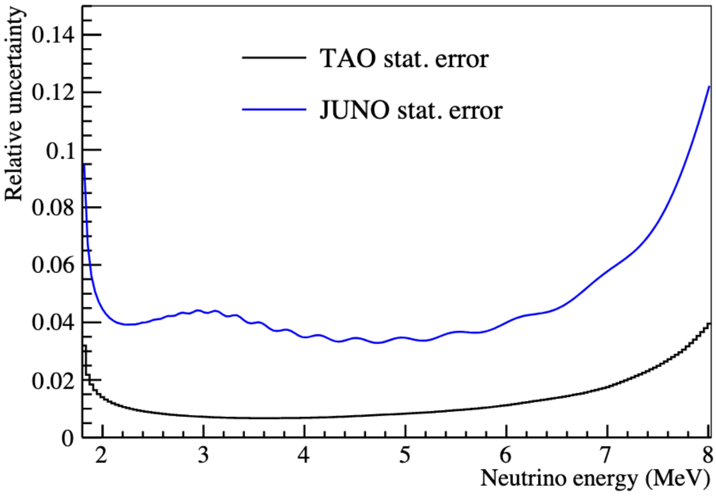

Figure 2.7: *The statistical uncertainty of TAO and JUNO with three and six year's of data taking respectively*

$S_i(E_\nu)$ is the antineutrino spectrum for each isotope. Evaluation of Δf_i for ^{235}U, ^{238}U, ^{239}Pu and ^{241}Pu in eq. 2.2 is a crucial aspect to assess the $\bar{\nu}_e$ flux differences between JUNO and TAO, since TAO detects antineutrinos mainly from the TS-C1 core while JUNO receives $\bar{\nu}_e$ from both the Taishan reactors and the six Yangjiang reactors. Taishan and Yangjiang nuclear power plants have different types of reactors, with 4.6 GW and 2.9 GW thermal power respectively, and will also face different running and refueling time periods, making the evaluation of Δf_i a fundamental point for mapping reactor neutrino spectra from TAO to JUNO. TAO statistical uncertainty will influence JUNO bin-to-bin spectral shape uncertainty, which refers to the differences in the measured values from one energy bin to another due to statistical fluctuations. Figure 2.7 illustrates the statistical uncertainty of TAO in three years of data, compared to JUNO uncertainty derived from six years of data. TAO maintains a statistical uncertainty below 1% in most energy regions of interest. Assuming a 10% difference in fission fractions between TAO and JUNO, the bin-to-bin uncertainty from the reference spectrum is around 1%. The energy dependence of the statistical uncertainty mainly reflects the variation of the detected event rate across the antineutrino spectrum. In the energy region where the reactor antineutrino flux is largest, roughly between 3 and 5 MeV, the higher event statistics lead to smaller uncertainties, while larger uncertainties appear at the edges of the spectrum where the event rate decreases. However, this behavior does not significantly affect the capability of TAO to provide a precise reference spectrum for JUNO, since in the energy region most relevant for the determination of the neutrino mass ordering the statistical uncertainty remains well below the percent level. It should be noted that Figure 2.7 illustrates only the statistical component of the uncertainty. In a realistic oscillation analysis, additional systematic uncertainties must also be considered, including reactor spectrum modeling, detector energy scale calibration, liquid scintillator non-linearity, and detector response effects such as energy leakage. These effects may introduce energy-dependent distortions of the reconstructed spectrum and modify the predicted antineutrino flux shape, as we will see later. In this context, the high-statistics measurement provided by TAO plays a crucial role in constraining the reactor spectrum shape and reducing the associated bin-to-bin spectral uncertainties. Also, a study on the sensitivity of the mass ordering of JUNO vs inputs bin-bin shape [48], as illustrated in Figure 2.8, clearly shows that incorporating TAO data (black marker), the mass ordering sensitivity χ^2 improves by approximately 1.5 compared to using the Daya Bay reference spectrum (blue marker). By offering a high-precision and model-independent reference spectrum, TAO will significantly contribute to JUNO objective of precisely measure neutrino oscillation parameters and in determining the neutrino mass ordering. TAO reference spectrum will play a crucial role in minimizing systematic uncertainties in JUNO oscillation analysis.

Search for light sterile neutrinos

As discussed in section 1.2.2, recent reactor antineutrino experiments observed a $\bar{\nu}_e$ deficit with respect to the prediction of antineutrino yield per fission models, the so-called Reactor Antineutrino Anomaly (RAA). Furthermore, anomalous $\bar{\nu}_e$ appearance in the $\bar{\nu}_\mu$ beam at the LSND [52] and MiniBooNE [53, 54] experiments and deficit in number of ν_e from radioactive calibration source in gallium experiments [55] were observed. All these observations could be explained if we extend our three-flavor neutrino mixing model, parametrized by the PMNS matrix, by an additional fourth neutrino with a mass splitting of approximately 1 eV^2. The corresponding flavor state would not participate in the weak interactions, since there are only three light active neutrinos [56], and thus it is called sterile. Nevertheless, it can still mix with the active ones and demonstrates its presence via neutrino oscillations. If a sterile neutrino state exists and mixes with the three active neutrinos, the observed reactor antineutrino spectrum would exhibit additional oscillatory distortions superimposed on the standard three-flavor oscillation pattern. These distortions would appear as energy-dependent modulations of the detected spectrum, whose frequency is determined by the additional mass splitting Δm^2_{41}. For values of Δm^2_{41} of the order of 1 eV^2, the oscillation length becomes very short, leading to rapid spectral variations as

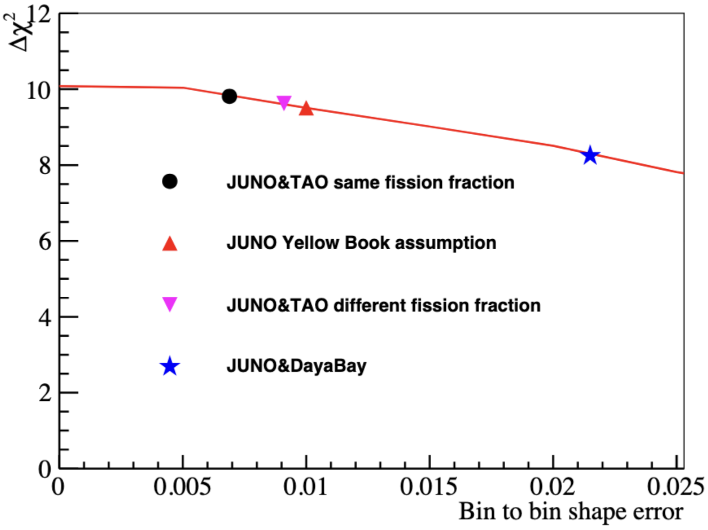

Figure 2.8: *The plot shows mass ordering sensitivity for different reference spectra (represented by different markers) for JUNO. The* $\Delta\chi^2$ *quantifies the sensitivity, where higher values indicate better discrimination between normal and inverted ordering. The Yellow Book assumption refers to the baseline detector and systematic uncertainty assumptions adopted in the JUNO Conceptual Design Report.*

a function of the neutrino energy. In a detector located at a short baseline such as TAO, these effects could appear as small periodic deviations from the smooth spectrum predicted by the standard three-flavor oscillation model. In the framework of simple a 3+1 neutrino flavour model which contains an additional sterile state, the oscillation probability for $\bar{\nu}_e$ disappearance can be approximated as:

$$P_{\bar{\nu}_e \to \bar{\nu}_e}(L, E) = 1 - 4 \sum_{i=1}^{3} |U_{ei}|^2 |U_{e4}|^2 \sin^2 \frac{\Delta m^2_{4i} L}{4E}, \tag{2.3}$$

where the mass splittings are defined as $\Delta m^2_{ij} = m^2_i - m^2_j$, m_i being the mass of the i-th neutrino state, and $|U_{ei}|^2$ are the elements of the extended 4×4 unitary mixing matrix. By accounting for background noise and systematic uncertainties, the discrepancy between observed and expected spectra will be evaluated statistically using the Confidence Level with signal hypotesis CL_s method [57, 58]. Exploiting its unique features, TAO complements existing experiments and holds promise for setting new limits on sterile neutrinos, expecting to set the best sterile neutrino limits around $\Delta m^2_{41} = 0.5 eV^2$.

Reactor monitoring

Antineutrino detectors can provide real-time monitoring of nuclear reactor power and fuel mixture, complementing standard methods and providing a safeguard against unauthorized nuclear activities. In addition to its primary role as a reference detector for JUNO, TAO will give valuable information for reactor monitoring. The reactor activity will be monitored by TAO using the overall antineutrino energy spectrum which varies for different isotopes based on their fission fraction, as discussed in previous sections. Changes in fuel composition affect flux and spectrum evolution. Precise measurement of these parameters is critical, especially given recent antineutrino experiments that have highlighted discrepancies from theoretical predictions [59]. The main aim of the safeguard is to determine the amount of plutonium produced in the reactor, since it could be nonetheless subject of interest for military purposes, and reveal its eventual removal through fuel reprocessing. This, as well as reactor monitoring in general, can be done from the overall neutrino flux and antineutrino energy spectrum measurements. TAO aims to bring precision in the spectral measurements that can serve as input for reactor monitoring and safeguard studies.

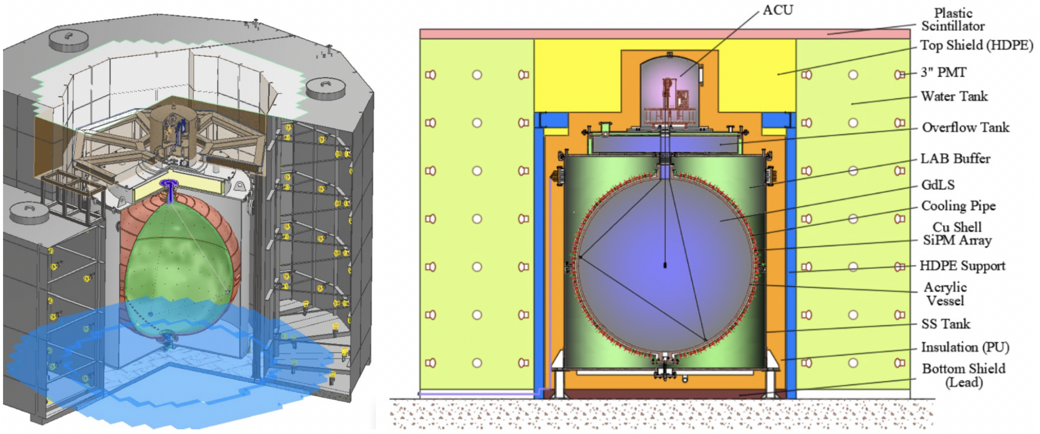

Figure 2.9: *Schematic view of the TAO detector, which consists of a Central Detector (CD) and Water Tanks (WT) and Top Veto Tracker (TVT) as veto system. The CD consists of 2.8 ton gadolinium-doped LS filled in a spherical acrylic vessel and viewed by* 10 m^2 *SiPMs, a spherical copper shell that supports the SiPMs, 3.45 ton buffer liquid, and a cylindrical stainless steel tank. The WT provides muon veto and consist of 1.2 m thick water in the surrounding tanks. Further shielding is provided by 1 m High Density Polyethylene (HDPE) on the top, and 10 cm lead at the bottom. On top, arrays of plastic scintillator form the TVT for muon veto, and Automatic Control Unit (ACU) serve for calibration.*

2.2.2 Detector overview

TAO is located inside the Taishan NPP in a basement 9.6 m underground approximately 44 m from one reactor core (TS-C1) of the Taishan NPP and approximately 217 m from the other reactor core (TS-C2). These two Taishan reactor cores contribute more than 99.99% of TAO antineutrino signal, with TS-C2 contributing 4%. Figure 2.9 shows a sketch of the detector. TAO consists of a Central Detector (CD) and two muon veto systems, a Water Tank (WT) and a Top Veto Tracker (TVT). The CD houses the LS and the SiPMs. The surrounding copper shell provides mechanical support and also thermal stability for the SiPMs. The copper shell is installed within the stainless steel tank that is filled with buffer liquid and maintained at -50°C. The WT surrounding it acts as shielding from natural radioactivity and from cosmogenic neutrinos, and also as a Cherenkov detector for muon veto. Further shielding is provided by 10 cm layer of lead bricks placed below the CD, and about 1 m of High Density Polyethylene (HDPE) coverage. On top there is the TVT, which provides muon detection using a plastic scintillator array, and the Automated Calibration Unit (ACU) used for calibration.

Central detector

The CD comprises of two layers. The inner layer is the LS housed within a spherical acrylic vessel. The 2.8 tons Gadolinium-doped liquid scintillator (Gd-LS) will serve as the neutrino target facilitating the detection of a distinct delayed signal of IBD resulting from neutron capture on Gd hence reducing accidental background. The LS recipe is the same as JUNO, 2 g/L 2,5-Diphenyloxazole, PPO (primary fluor), 1 mg/L 1,4-Bis(2-methylstyryl)benzene (secondary wavelength shifter), with the addition of 0.43 g/L ethanol (co-solvent to improve solubility at low temperatures) and 0.1% Gadolinium by weight (for neutron capture). This composition is engineered to provide excellent optical properties and extremely high radiopurity. In particular, contamination from long-lived radioactive isotopes such as ^{238}U and ^{232}Th is required to be at the level of about 10^{-15} g/g, while the concentration of ^{40}K must be reduced to around 10^{-16} g/g. Achieving such radiopurity is essential to suppress internal radioactive backgrounds and to ensure the precise measurement of the reactor antineutrino spectrum, which is necessary to reach the target energy resolution of better than 2% at 1 MeV. Surrounding it is the acrylic vessel that has an inner diameter of 1800 mm and a thickness of 20 mm. A copper sphere surrounds the acrylic vessel, offering mechanical support to ensure the SiPM tiles are directed towards the center of the detector. The external surface of the copper sphere is utilized for the readout electronics and accommodating the cooling pipes. The outer layer contains the buffer liquid, 3.45 tons of Linear Alkylbenzene (LAB), the same as the liquid scintillator solvent, held in a Stainless Steel Tank (SST). LAB's water content can precipitate at low temperatures, reducing transparency, necessitating extensive drying. Adding Dipropylenglykol-n-butylethe (DPnB) as a freezing inhibitor and antioxidant addresses this. The stainless steel tank is insulated with 20 cm thick Polyurethane (PU), and supports all components within the SST. It ensures an air-tight environment for the LAB, maintaining a temperature of −50 °C inside the SST while requiring insulation to regulate room temperature outside. TAO uses large-area SiPM tiles produced by Hamamatsu with each tile integrated with 32 chips of dimension 12 mm x 6 mm [60]. These SiPM tiles has a photon detection efficiency (PDE) exceeding 50%. To keep the dark noise rate within acceptable bounds, which is defined as the rate of spurious pulses generated by the SiPM in absence of incident light, the SiPMs operate at cryogenic temperatures of −50 °C. SiPM photosensors are mounted on a spherical copper shell surrounding the acrylic vessel, with a distance of 18 mm between the SiPM surface and the acrylic vessel. Each SiPM tile connects to a Front-End Board (FEB) for readout. A total of 4024 SiPM tiles provide a $\sim$ 95% coverage of the detector area. Further details of the SiPMs and the front-end electronics will be given in the next chapter. A specialized Data Acquisition (DAQ) system will filter and capture events.

Water tanks

Surrounding the CD, there are three irregular water tanks that form a dodecagon with 1.2 m thickness serving as both passive shielding (from environmental radioactivity from rock and air) and active Cherenkov muon detectors (effectively serving as a veto detector). The tanks are equipped with 3 inch PMTs to detect Cherenkov light from muons. Approximately 300 PMTs are evenly spread, averaging 1 PMT per 0.5 m^2, providing about 0.8% surface coverage. These 3-inch PMTs, along with their bases, potting, and electronic readout, will use the same technology as the JUNO small PMT system. The PMTs require a time resolution of approximately 2 nanoseconds to accurately establish the veto window timing. The dodecagon shape, chosen for TAO, accommodates space constraints and contains approximately 70 tons of water in total. The tanks are lined with reflective Tyvek film and hold PMTs in place with stainless steel frames. A purification system maintains the clarity of the water and reduces radioactivity. Circulation ensures water turnover in a day.

Top veto tracker

On top of the detector there is the TAO Veto Tracker (TVT). The system is composed of 160 layers of plastic scintillator strips, where each layer consists of parallel scintillator bars forming independent detection channels, arranged in successive planes covering the entire upper surface of the detector. The scintillator strips in each plane are aligned parallel to each other, while consecutive planes are oriented orthogonally, forming an X–Y tracking configuration. Each module consists of long, narrow scintillator bars that form independent detection channels, allowing the tracker to reconstruct the passage of muons through the detector. The scintillation light produced in the strips is collected through wavelength-shifting fibers and read out by silicon photomultipliers (SiPMs). The modular design ensures uniform response over the entire area and provides redundancy against local inefficiencies. The top tracker significantly improves the veto performance for near-vertical muons, enabling the rejection of cosmogenic backgrounds such as fast neutrons. Together with the surrounding water-Cherenkov detector, it forms an integrated muon-tagging system that achieves the high efficiency needed for TAO low-background operation.

DAQ and trigger

The data acquisition architecture of TAO is designed to efficiently record energy depositions produced by reactor antineutrino interactions while suppressing noise-induced signals originating from the SiPM photosensors. The central detector adopts a quasi-triggerless readout scheme in which the SiPM signals are continuously digitized by the front-end electronics. However, only signals satisfying predefined selection conditions are transmitted to the data acquisition system in order to limit the data throughput. The digitized waveforms are processed in the data acquisition system, where pulses corresponding to signals are identified and grouped in time to reconstruct physical events. Event candidates are then selected by requiring a minimum multiplicity of SiPM hits within a predefined time window of the order of a few hundred nanoseconds. In the TAO trigger scheme this multiplicity threshold is of the order of 10^2 channels, corresponding to about 170 coincident SiPM hits. Such a requirement efficiently suppresses accidental triggers induced by the intrinsic dark noise of the SiPMs while preserving high efficiency for energy depositions in the MeV range typical of inverse beta decay interactions.

Automatic calibration unit

The TAO Automated Calibration Unit (ACU), based on a similar system used in the Daya Bay experiment [61], allows the precise installation of radioactive sources for detector calibration. The ACU is a system that can mount a variety of radioactive sources, including the ^{68}Ge source, combined gamma-emitting isotopes (^{137}Cs, ^{54}Mn, ^{40}K, ^{60}Co), and a neutron source ($^{241}\mathrm{Am}-{}^{13}\mathrm{C}$). Placed on top of the detector and using two stepper motors, the ACU is able to move these sources inside the detector with sub-millimeter precision based on glued anchors on the inner wall of the acrylic vessel. The ACU also includes an ultraviolet LED calibration system and Cable Loop System (CLS). The ultraviolet LED is used to monitor SiPMS and for precise timing calibration. The CLS facilitates the use of radioactive sources at varying detector positions and enables the accurate mapping of energy-response distributions across various geometries of the detector.

Detector installation

A neutrino lab has been built at the Taishan Nuclear power plant at a distance of 44 meters from the TS-C1 reactor core. The layout includes space for the TAO detector and it's related facilities, which are constrained by a height of 3.85 m. The CD assembly included liquid filling, integrating SiPM tiles and Front-End Electronics (FEE) with the copper shell, bonding acrylic pieces, and building the stainless steel tank. Following the CD installation, the ACU has been mounted on the SST, protected by a thermal insulation hat made up of HDPE. The veto and shielding setup comprise of a lead bottom shield for the CD, three water tanks encircling the CD, HDPE shielding material positioned above the CD, and plastic scintillator detectors situated at the top the HDPE shielding.

During my PhD, in June 2025, I contributed to the installation of the central detector. Figures 2.10, 2.11, 2.12, 2.13, and 2.14 show the mounting of the different components: SiPMs, FEBs, acrylic sphere, cabling and stainless steel tank mounting and insulation. The TAO detector installation has been completed in November 2025. Currently, the detector is finishing the commissioning phase. Data taking is expected to start at the beginning of 2026.

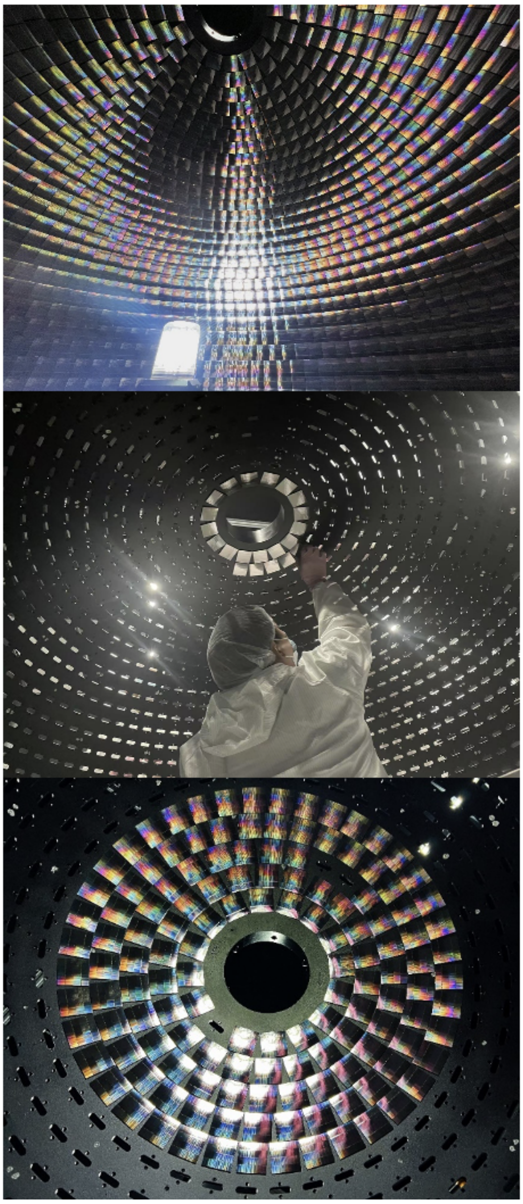

Figure 2.10: *Pictures of the installation of the 4024 SiPM tiles inside the copper shell.*

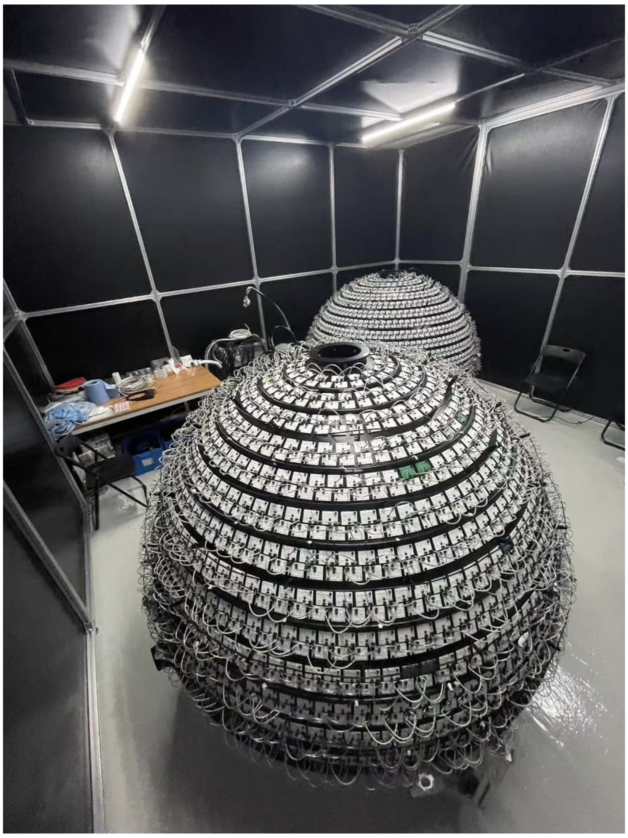

Figure 2.11: *Picture of the installation of the 4024 Front-End boards tiles outside the copper shell.*

Figure 2.12: *Pictures of the installation of the acrylic sphere inside the copper shell.*

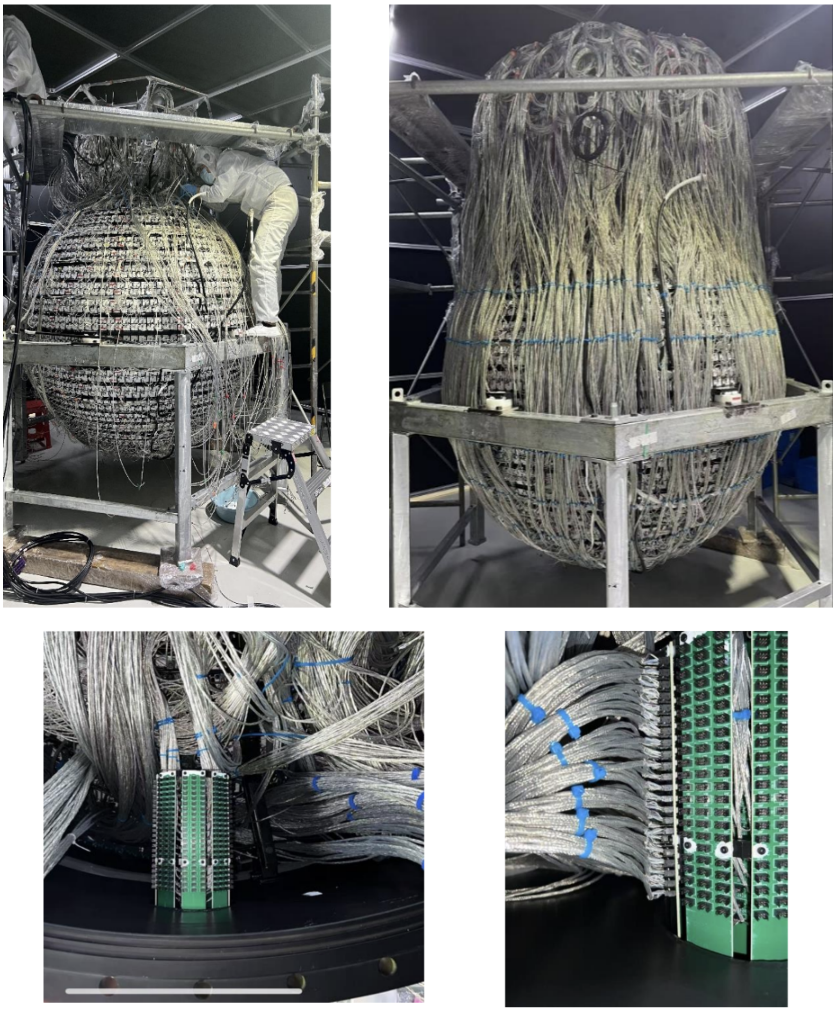

Figure 2.13: *On top, pictures of the cabling of the Front-End boards. At bottom, pictures of the flanges cabling.*

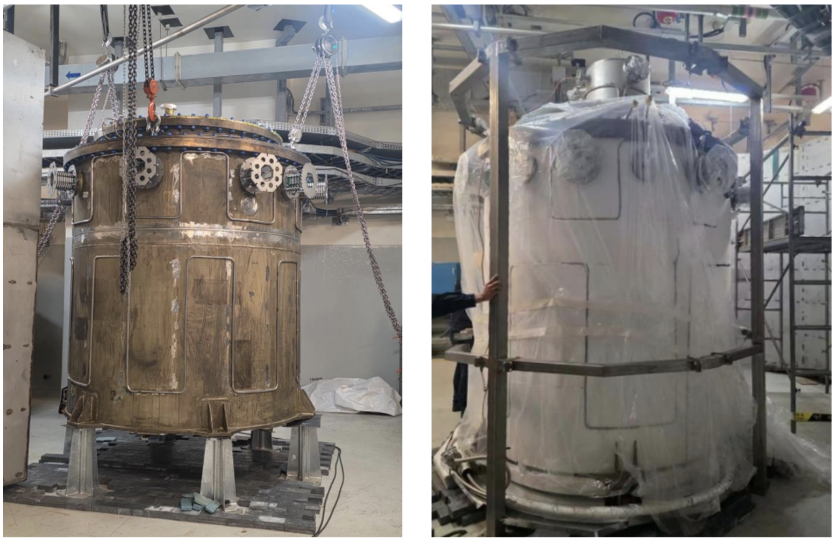

Figure 2.14: *On the left, a picture of the stainless steel tank installed. On the right, the SST after the insulation with 20 cm thick Polyurethane.*

2.2.3 Signal and backgrounds

Signal

As discussed in section 1.2, reactor antineutrinos $\bar{\nu}_e$ are generated from the fission products of four major isotopes,^{235}U, ^{238}U, ^{239}Pu and ^{241}Pu. The $\bar{\nu}_e$ are detected in TAO through IBD reaction in the gadolinuim-doped LS. The antineutrino spectrum from a commercial reactor decreases with increasing energy, therefore the resulting IBD spectrum has a bell shape with the maximum around $3.5 - 4.0$ MeV, as shown in Figure 1.5. The positron deposits its energy in the scintillator and annihilates with an electron creating two 0.511 MeV gamma rays giving a prompt signal. Neutrons are predominantly captured by hydrogen (H) emitting one 2.2 MeV gamma or by gadolinium (Gd) emitting several gammas with a total energy of about 8 MeV. The average neutron capture time in TAO is about $30\mu s$ with 0.1% loaded Gd by mass, giving a peculiar delayed signal. The coincidence of the prompt scintillation generated by the e^+ with the delayed neutron capture on Gd provides a distinctive $\bar{\nu}_e$ signature, as showed in Figure 2.15. In fact, IBD signals are selected based on the tagging of the $\sim$ 8 MeV signal of neutron capture on Gd as the delayed signal. The H capture signal with a lower energy of 2.2 MeV is not considered in the IBD selection, otherwise the background rate will increase by about one order of magnitude. The overall detection efficiency with a set of selection cuts is about 50% in the 1 ton fiducial volume (FV). The IBD detection efficiency can be broken down to the following:

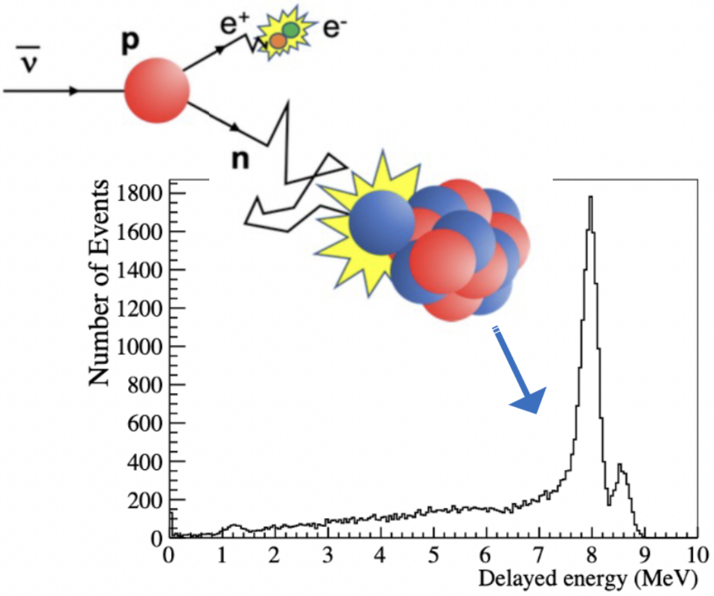

Figure 2.15: *The delayed energy distribution in the detector for the Gd-capture events in the FV. Two peaks around 8 MeV correspond to captures on two natural isotopes of Gd, 7.94 MeV for* ^{157}Gd *and 8.54 MeV for* ^{155}Gd.

- The IBD neutrons are mostly captured by Gd and H. The Gd capture fraction is 87%, which is the main detection channel. The H capture fraction is 13%, and the C capture fraction is less than 0.1%.
- To select the $\sim$ 8 MeV delayed signal of neutron capture on Gd, a 7–9 MeV energy cut is applied, and this yields a 59% detection efficiency.
- The efficiency for the prompt energy cut ($>$ 0.9 MeV) is 99.8%.
- The efficiency for the prompt-delayed coincidence time cut ($1\mu s < \Delta T < 100\mu s$) is about 97%.

The TAO detector will detect about 1000 IBD events per day in the fiducial volume based on the selection cuts.

Type	Rate per day
Signal	1000
Fast neutron	86
^{9}Li/^{8}He	54
Accidental	190

Table 2.1: TAO signal and background rates per day in the fiducial volume.

Backgrounds

Background is one of the critical concerns of TAO since the overburden is just 10 m-w-e in the 9.6 m underground basement. The correlation of the prompt and delayed signals in TAO is a powerful signature to tag the reactor antineutrino signal and suppress backgrounds. Backgrounds are usually classified into correlated and uncorrelated backgrounds. A correlated background refers to a pair of prompt and delayed events coming from the same source, while an uncorrelated background refers to the prompt and delayed events coming from different origins but falling into the time window accidentally, thus is also called an accidental background. An energetic neutron entering the detector can form a fast-neutron background by recoiling off a proton before being captured. Multiple neutrons produced by the same muon may be captured in the detector and form a prompt-delay pair in the IBD event selection window, referred as a double-neutron background. Furthermore, cosmic muons that interact with carbon present in the liquid scintillator may generate isotopes such as ^{9}Li and ^{8}He, contributing to correlated background. The most impacting backgrounds are the uncorrelated ones, in particular the cosmogenic neutron background, typically arising from natural radioactivity. Applying further strategies, like selecting the events in the fiducial volume, doping Gadolinium in the LAB buffer liquid and optimizing of the veto strategy reduce the neutron background-to-signal ratio from an initial estimate of about 10% [44] to approximately 2% [62]. Table 2.1 shows TAO signal and background rates per day in the fiducial volume.

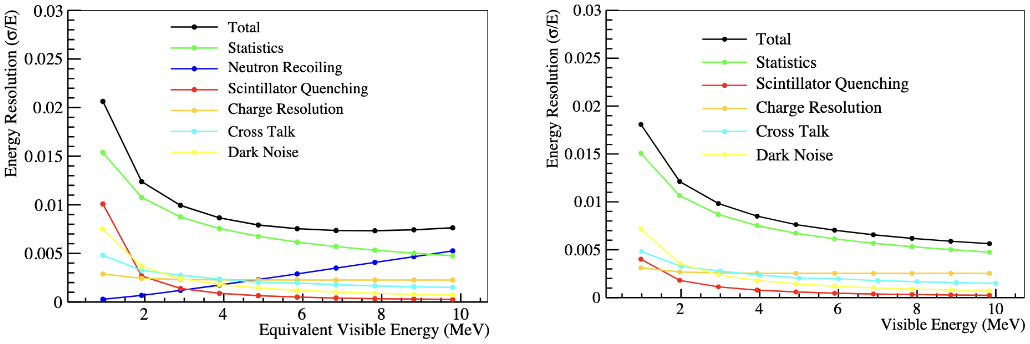

Figure 2.16: *Expected energy resolution of the TAO detector. Left: energy resolution for reactor antineutrinos versus equivalent visible energy defined as the reconstructed neutrino energy minus a constant shift of 0.78 MeV due to the IBD reaction kinetics. It includes the effect from the spread of the neutron kinetic energy in the IBD reaction. Right: energy resolution for positrons without the effect of neutron kinetic energy.*

2.2.4 Energy resolution

The energy resolution is a key parameter for the TAO experiment. It is predominantly determined by the statistics of the collected photoelectrons (p.e.). Compared with the ∼ 1400 p.e./MeV in the JUNO experiment, a photoelectron yield of ∼ 4500 p.e./MeV is expected in TAO considering the following improvements with-respect-to (w.r.t) JUNO:

- The coverage of photon sensors is improved to ∼ 95% w.r.t ∼ 78% in JUNO
- The photon detection efficiency is improved to ∼ 50% using SiPMs w.r.t ∼ 27% with PMTs in JUNO.
- Smaller dimension of the TAO detector w.r.t JUNO increases the photoelectron statistics by ∼ 40% due to less photons absorbed in the liquid scintillator.
- Low temperature of $-50\,^{\circ}$C increase the photon yield of LS by ∼ 25% w.r.t JUNO, reaching $>$ 12000 photons per MeV.

The expected energy resolution as a function of energy obtained from the TAO detector simulation is shown in Figure 2.16. It takes into account several detector effects: photoelectron statistics, neutron recoil, scintillator quenching and SiPM-correlated effects such as charge resolution, cross talk and dark noise, as we will see in the next chapter. Scintillator quenching refers to the reduction of light yield in organic scintillators for particles with high ionization density, which leads to a non-linear relation between deposited energy and produced scintillation light. The performances of the SiPMs play an important role in reaching an energy resolution better than $2\%/\sqrt{1MeV}$, which is fundamental to reach the physics goals for TAO.

2.2.5 Expected energy spectra

The expected energy spectra at TAO are obtained starting from the theoretical inverse beta decay (IBD) spectrum, calculated as the convolution of the reactor antineutrino flux with the IBD cross section, as discussed in 1.2.3. This spectrum describes the distribution of the true neutrino energies before detector effects are taken into account. Since the detector measures the visible energy produced by the positron in the scintillator rather than the neutrino energy itself, several detector effects must be considered in order to obtain the spectrum that is actually observed. In particular, two detector effects play an important role in shaping the reconstructed energy spectrum. The first one is the energy leakage effect, which occurs when a fraction of the energy released by the prompt event escapes the active scintillator volume and therefore does not contribute to the detected signal. This effect is especially relevant for compact detectors such as TAO, where secondary particles produced in electromagnetic showers may partially deposit their energy in non-active detector regions. The second important effect is the liquid scintillator non-linearity (LNSL). In organic scintillators the relation between the deposited energy and the number of produced scintillation photons is not strictly linear. This non-linearity arises mainly from quenching effects associated with particles of high ionization density, as well as from detector-related effects such as the response of the photodetection system and the electronics. As a consequence, the reconstructed visible energy differs from the true deposited energy. After including these detector effects, the resulting visible-energy spectrum is further modified by the finite energy resolution of the detector and by the presence of background contributions. The effect of the detector energy resolution is implemented by convolving the visible-energy spectrum with the detector response function, which is typically modeled as a Gaussian distribution whose width is determined by the detector energy resolution. This procedure accounts for statistical fluctuations in the detected number of photoelectrons and results in a smearing of the reconstructed energy spectrum. The predicted energy spectra after incorporating these effects are shown in Figure 2.17.

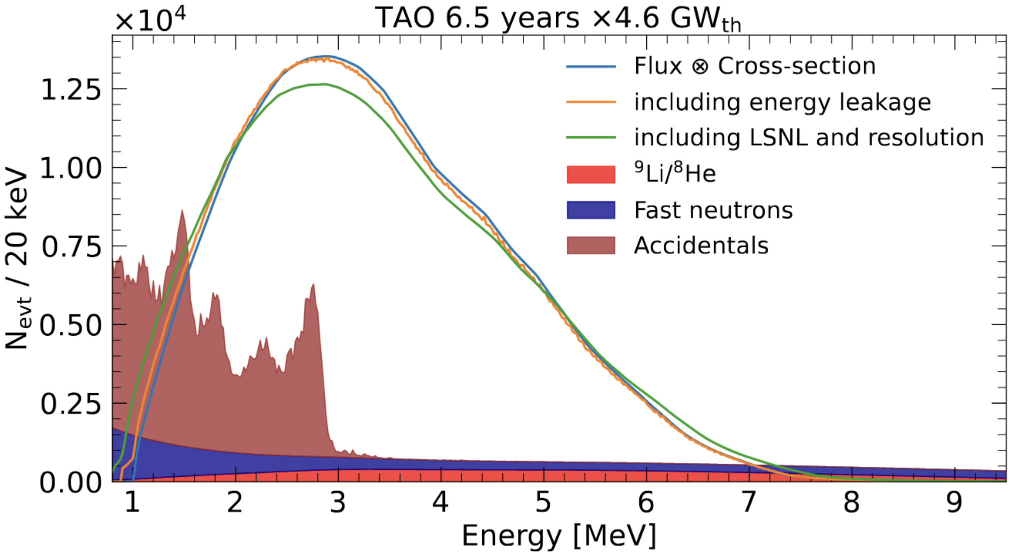

Figure 2.17: *Energy spectra of expected IBD signals in TAO from both TS-C1 and TS-C2 with energy leakage, LSNL, and energy resolution effects applied. The reconstructed energy spectra expected for the three major backgrounds are represented by the filled histograms. All spectra corresponds to an exposure of* 6.5 *years* × 4.6 GW_{th}.

Chapter 3

Characterization of TAO Silicon Photomultipliers and Front-End Electronics

To achieve the target energy resolution below 2% at 1 MeV, required to meet its physics goals, TAO relies on photosensors with outstanding performance. In this context, Silicon Photomultipliers (SiPMs) represent a natural choice, as they can reach a Photon Detection Efficiency (PDE) significantly higher than that of conventional Photomultiplier Tubes (PMTs). To fully exploit the performance of the SiPMs, a state-of-the-art front-end electronics system is required.

Roma Tre University played a key role in this effort, being responsible for the design and development of two fundamental components of the TAO front-end electronics: the Front-End Boards (FEBs), directly coupled to the SiPMs, and the Analog-to-Digital Converters (ADCs).

During my Ph.D., I studied the performance of the TAO SiPMs coupled with a set of pre-production FEBs. The characterization focused on validating the correct behavior of the system, with particular attention to four figures of merit directly impacting the detector energy resolution. In the final phase of my Ph.D., I also contributed to the mass testing campaign of the produced FEB and ADC boards.

This chapter is organized as follows. The first part introduces the operating principles and main characteristics of SiPMs, followed by a description of the TAO photosensors and front-end electronics. The second part presents the characterization of the SiPMs coupled with the pre-production FEBs, performed at the INFN laboratories (Istituto Nazionale di Fisica Nucleare) of Roma Tre University.

3.1 Silicon Photomultipliers

The Silicon PhotoMultiplier (SiPM), also known as Multi Pixel Photon Counter (MPPC), is a solid-state photo-detector made of an array of integrated Single-Photon Avalanche Diodes (SPADs) also called micro-cells or pixels. A SiPM detects photons by converting them into electron-hole (e-h) pairs, multiplying these e-h pairs, and finally collecting them as a large electric signal by summing all the signals from single micro-cells [63]. One of the most important properties of the SiPM is the ability to detect and count photons with high resolution and single-photon sensitivity. Moreover, the internal avalanche amplification is fast enough to obtain a very good timing resolution. These properties, along with advantages such as low operation voltage, compactness, and robustness, make the SiPM an excellent device for light detection, especially when the fast timing and high Photon-Detection Efficiency (PDE) are required. This kind of photo-detector sensor is used in different scientific research as well as in the commercial and medical fields: Time Of Flight Positron Emission Tomography (TOF-PET) [64], lifetime fluorescence spectroscopy [65], distance measurements in LIDAR applications [66], astrophysics, quantum-cryptography and related applications [67], neutrino detectors [44], ground-based and spaceborne high-energy astrophysics [68] as well as in calorimetry for high-energy physics [69].

3.1.1 SiPM operation principles

The building block of a SiPM is the SPAD that exists in two different types: a n-doped region on a p-doped layer and vice versa. Due to the reverse biasing, electrons flow in the direction of the n-doped region. A schematization of a SPAD is shown in Figure 3.1. When a photon interacts with the SPAD generates a large electric output signal due to internal avalanche multiplication. So, the avalanche-triggering probability is the probability that an electron or hole passes the p-n junction to generate enough secondary e-h pairs in order to trigger a self-sustainable avalanche. This probability depends on the SPAD configuration and the applied electric field, and it is higher for electrons: this means that electrons predominantly produce the avalanche. The absorption length of photons in Silicon is well known and strictly depends on the wavelength. The result is that near-UV photons are absorbed closer to the surface of the SPAD, whereas near-IR photons are absorbed deeper. Consequently, the p-on-n SPAD is more sensitive in the near-UV region whereas the n-on-p is more sensitive in the near-IR one. Depending on the applied reversed voltage, there are three different operational regions: photodiode mode, avalanche photodiode (APD) mode and Geiger

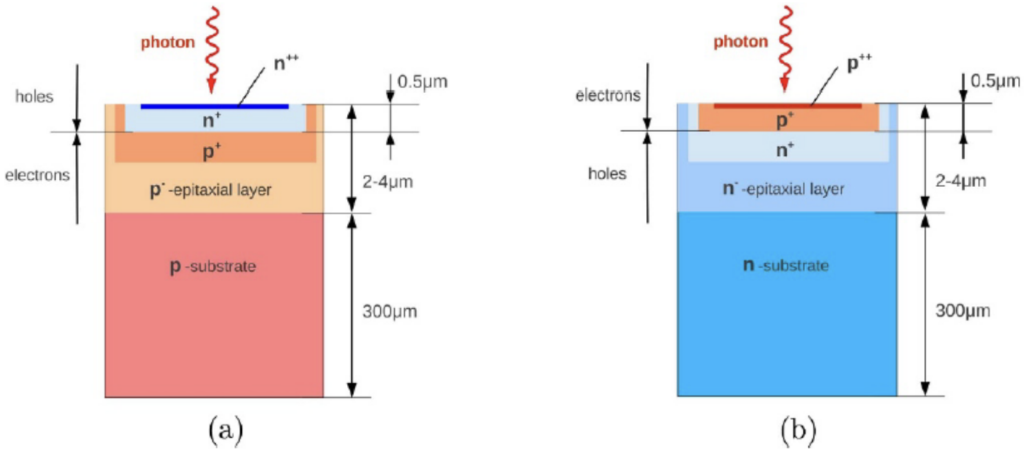

Figure 3.1: *(a), the n-on-p SPAD structure is more sensitive to the red light while on the right (b) the p-on-n SPAD structure is more sensitive to the blue and near UV wavelength.*

mode. In the first region, the voltage is low and there is no multiplication of e-h pairs. In this case, the pairs are separated by the electric field and a current proportional to the intensity of light can be measured. In the avalanche regime, primary electrons can gain enough energy to create secondary e-h pairs, due to the higher electric field when increasing the applied reverse voltage. Since only electrons can create additional e-h pairs, the avalanche is self-quenched and flows only in one direction. Due to their higher mass, holes need a larger electric field to generate secondary e-h pairs. The Geiger mode regime can be obtained by increasing the applied reversed voltage over a certain value, called breakdown voltage V_{bd}. The value of V_{bd} depends on the internal structure of the diode, the doping profiles at the p-n junction, and the temperature. In this regime, holes gain enough velocity to create secondary e-h pairs. This is the regime of the SPAD used in SiPMs. Under such conditions, the current increases very rapidly, resulting in a very precise timing. Moreover, the avalanche that originates is self-sustaining, and, in a SiPM, quenching is achieved by using a large resistance in series with the diode. In fact, the current produced by the avalanche creates a voltage drop across the quenching resistance R_q, that stops the avalanche when the voltage across the diode reaches V_{bd}. The operating regime and the voltage dependencies are shown in Figure 3.2. It is often convenient to introduce the overvoltage V_{ov}, which is defined as the difference between the bias voltage (i.e., the actual applied voltage V_{bias}) and the breakdown voltage (V_{bd}):

$$V_{ov} = V_{bias} - V_{bd} \tag{3.1}$$

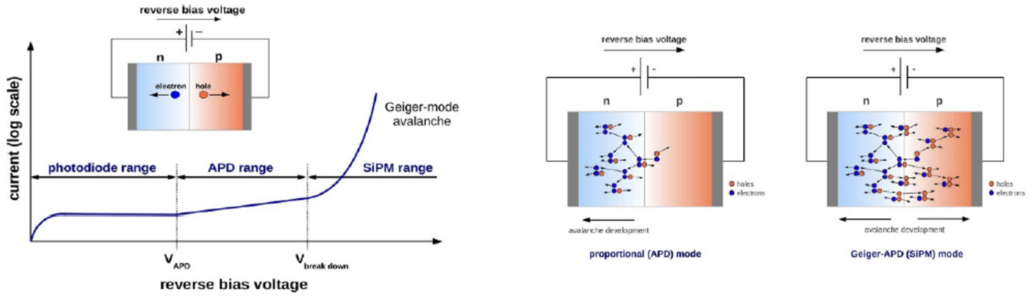

Figure 3.2: *(a), the operation regimes of the solid-state p-n junction, i.e. photodiode, avalanche photodiode, and SPAD or SiPM range. On the abscissa, there is the supply voltage while on the ordinate there is the current in a logarithmic scale. (b), the proportional diode regime and the Geiger regime are sketched with a focus on the carriers. In the APD only electrons can sustain the avalanche, whereas in a SPAD holes will perform impact ionization as well.*

Once the over-voltage of the SiPM has been fixed, it is possible to illuminate the SiPM in order to extract the signal amplitude distribution also known as the multi-photon spectrum. Under weak pulsed illumination, the SiPM charge spectrum displays a sequence of Gaussian peaks associated with the detection of 0, 1, .. , n photoelectrons (p.e.). Since each avalanche microcell delivers a nearly identical charge, the spectrum is quantized: the pedestal corresponds to no fired cells, i.e. electronic noise, while higher-order peaks arise from multiple simultaneous avalanches. A typical multi-photon spectrum of a SiPM is depicted in Figure 3.3, with the corresponding gaussian fit applied on the single photoelectron peaks. This multi-photoelectron structure is a key diagnostic tool for characterizing SiPM behavior, as we will see in detail later.

The gain of a SiPM is defined as the number of elementary charges collected following the interaction of a single photon. It can be expressed by the following relation:

$$G = \frac{C \cdot V_{OV}}{e} \tag{3.2}$$

where C is the internal capacitance of the SiPM and e is the elementary charge. From the previous equation, considering that the capacity of a pixel with a side of 50 μm is typically of the order of a few tens of fF and that the overvoltage used is usually about $2 \div 4\ V$, it is possible to obtain a gain in the range $10^5 \div 10^7$, of the same order as the gain obtainable with photomultiplier tubes. The gain can be evaluated by following two different procedures. The

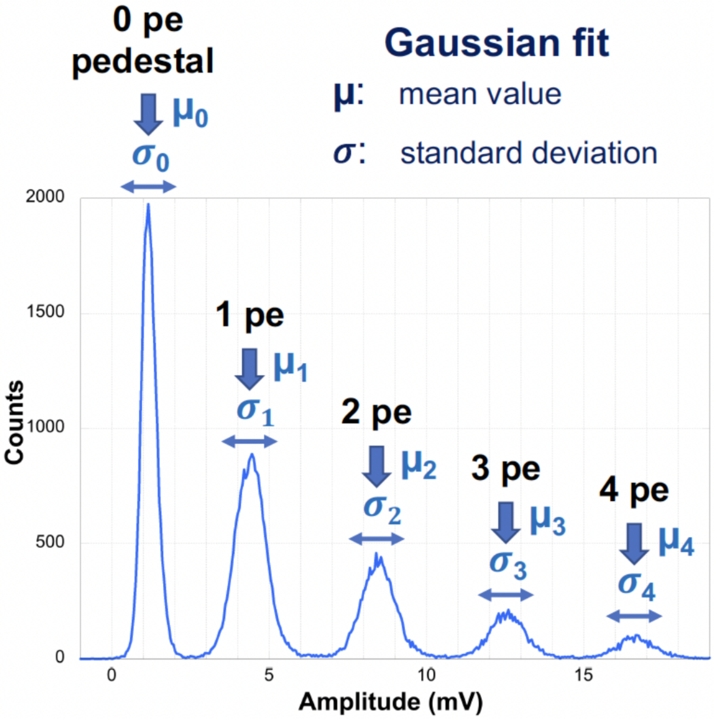

Figure 3.3: *The multi-photon spectrum of a SiPM tile. The first peak corresponds to 0 p.e. collected (pedestal), the second one to 1 p.e. and so on. The mean value μ and the standard deviation σ of the gaussian fit on each peak are also shown*

first procedure requires the evaluation of the linear coefficient of a linear fit of the centroids, obtained from a Gaussian fit of each peak in the multi-photon spectrum. The second one needs to extract the difference in ADC channels between two adjacent peaks in the same spectrum.

Photon detection efficiency (PDE) quantifies the ability of a single-photon detector to detect photons, that is the ratio between the number of detected photons and the photons arriving at the detector. The PDE of a SiPM is a function of the quantum efficiency QE of the individual APDs, of the probability that the avalanche multiplication phenomenon occurs $P_{trigger}$ and of the geometric *fill-factor* coefficient FF_{geom}:

$$PDE = QE \times P_{trigger} \times FF_{geom} \tag{3.3}$$

The quantum efficiency depends on the properties of Silicon and is a function of the wavelength of the incident photon. The probability $P_{trigger}$ depends on the intensity of the electric field inside the device and, therefore, on the overvoltage. Finally, the fill-factor FF_{geom} is given by the ratio between the active area of the SiPM and its total area; the space covered by the metal contacts present between the APDs, in fact, is not sensitive to photons and contributes to decreasing the active area of the device and consequently its efficiency. In modern SiPMs, the combined optimization of these three factors leads to photon detection efficiencies that can exceed 50% in the blue–near-UV region, where most liquid-scintillator emission is concentrated. Such high PDE values are essential in high-precision neutrino experiments, as they directly enhance photon statistics and enable the sub-percent energy resolution required for accurate spectral reconstruction.

3.1.2 SiPM noise effects

The noise effects in the SPADs and in the SiPMs can be divided in two categories:

- Thermal noise: avalanche pulse triggered by random thermally generated carriers, not related to the occurrence of a primary event.
- Correlated noise: avalanche pulses subsequent to a primary event, which are generated because of the primary ones, thus "correlated" to this one. These pulses are generated due to afterpulsing (in the same cell) or to optical crosstalk (in neighboring microcells of the SPAD-array or SiPM).

Thermal noise is a common problem for all solid-state devices. This type of noise is generated by thermal agitation phenomena that produce

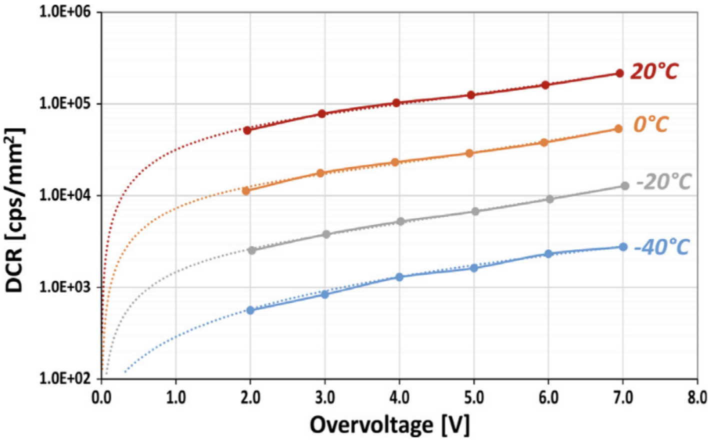

Figure 3.4: *Example of measured DCR of a SiPM as a function of overvoltage at different temperatures*

electron-hole pairs inside the semiconductor material. If these randomly generated carriers manage to reach the multiplication region, they can lead to an avalanche multiplication process. Furthermore, this effect cannot be distinguished from the pulses produced by real events. This means that the signal resulting from a photoelectron generated in the depletion region is identical to that resulting from a single random thermally-generated carrier. The dark count rate (DCR) is the frequency of false signals (counts) in the absence of light, and is caused mainly by thermal noise. The DCR depends on the overvoltage, on the temperature, and on the dimensions of the sensitive area of the SiPM. This last contribution places a strong limit on the realization of SiPMs with a large active surface. Decreasing the temperature significantly decreases the DCR, as shown in the example in Figure 3.4.

Correlated noise refers to secondary avalanche pulses that occur as a consequence of a previous (primary) avalanche. These additional avalanches may occur in the same microcell (afterpulsing) or in neighboring cells (optical crosstalk). Correlated noise increases the effective charge and fluctuations recorded per event, thereby degrading the signal-to-noise ratio of the SiPM. Afterpulsing is a correlated noise component of SPADs and SiPMs due to trapping and subsequent release of carriers in the high field region. After a primary event (dark count or detected photon), some of the carriers can be trapped and then released generating a secondary spurious avalanche. The afterpulsing probability depends on the number of effective traps in the high-field region and on their release time constant compared to the recharge time constant of the micro-cells. In order to reduce the afterpulse probabil-

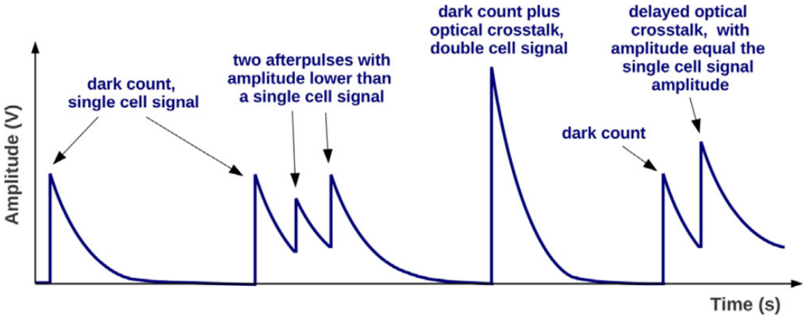

Figure 3.5: *Representation of the SiPM output signal of the different kinds of noise observable: primary events, prompt crosstalk, afterpulsing and delayed crosstalk events.*

ity (or at least its visible effect), the recharge time constant can be tuned so that most of the release of the trapped charge carrier happens when the cell is not fully recharged. Afterpulsing can also be optically induced. During each avalanche, secondary photons are also produced and some of them can be re-absorbed in the same micro-cell in the neutral region beneath the active region. This can photo-generate carriers that can reach via diffusion the depleted region, where they can trigger a secondary spurious avalanche. As described above, secondary photons are produced during the avalanche. This photon emission is isotropic and gives rise to absorption and photon-generated carriers in neighboring SPADs (neighboring cells in the SiPM). This phenomenon is the cause of the optical Cross-Talk. When a photon is detected in one cell, the avalanche pulse in this cell can trigger (with a certain probability) avalanches in the neighboring cells, thus, for example, creating pulses with two times or three times the single-cell amplitude in a SiPM, even though the hitting photon was only one. This type of optical Cross-Talk is also called direct or prompt optical Cross-Talk. The output signal of the SiPM is twice as high in amplitude as can be seen in Figure 3.5. Another type of optical Cross-Talk is the delayed optical Cross-Talk. It is caused by secondary photons generating an electron–hole pair in bulk, or generally in the neutral regions near the depleted one. The charge carriers will diffuse and some of them can reach the active region and trigger an avalanche with a delay of several nano-seconds to micro-seconds.

3.1.3 Analytical model of SiPM signal and noise

The signal produced by a SiPM in response to incident photons, as we have seen, is strongly contaminated by the noise effects correlated to it. In fact, the high gain of solid-state photomultipliers is intrinsically accompanied by the optical emission induced by the charge carriers and the trapping effects that cause crosstalk and afterpulsing, each of which, in turn, deteriorates the probability distribution of the output signals and causes an excess signal. The factor that takes into account the noise due to secondary phenomena is called Excess Noise Factor (ENF). In general, therefore, it is necessary to study and understand the ways in which crosstalk and afterpulse events contribute to the excess signal. The analytical expressions of the probability distributions and of the ENF caused by optical crosstalk and by afterpulses allow a complete knowledge of these stochastic processes [70].

In the measurements carried during my Ph.D., the use of SiPMs is aimed at studying the response in single photoelectron conditions, in which the individual avalanche photodiode (APD) pixels are activated by only one photon, as will happen for the TAO detector; more pixels active simultaneously lead to the measurement of more single photoelectrons. In this mode, the phenomenon that most affects the output signal is the optical crosstalk. It is important, therefore, to study the analytical models for the probability distributions of the signal due to photon and crosstalk events.

Let us consider a general case of SiPM output signal statistics. We assume that any output pulse produced by any single fired pixel, the so-called single electron response (SER), is identical regardless of the pixel triggering origin (dark count electron, photoelectron, crosstalk). The appearance of SER is further referenced as an event. Simultaneously fired pixels yield multiple SER events. We assume that crosstalk events, i.e. secondaries, appear simultaneously with the initially fired pixels, and primaries due to photoelectron or dark count electron triggering. The total number of output SER events initiated by N primary events (random variable X) includes all primaries and all secondaries as follows:

$$X = \sum_{i=1}^{N} (1 + C_i), \tag{3.4}$$

where C_i is the number of crosstalk events initiated by a single primary event i. C_i are assumed to be identically distributed random variables independent from N. To obtain a model for the output signal of a SiPM, it is therefore possible to study the probability distribution P(X = k), the mean E[X] and the variance Var[X] of the number of photoelectron events. For the excess noise factor of random events in output, two different circumstances are distinguished:

- The number of primary events N is a non-random fixed number (for example N = 1). This case corresponds, for example, to the measurement of SiPM output signal amplitude or charge histogram by triggering acquisition from 0.5 SER level (for example, measuring dark counts). Then X and ENF[X] can be expressed as:

$$X = 1 + C_i \tag{3.5}$$

$$ENF[X] = 1 + \frac{Var[X]}{E[X]^2} \tag{3.6}$$

This definition can be used, for example, for the avalanche multiplication process, because in APD we consider gain (equal to X) resulting from single electron initiation of an avalanche.

- The number of primary events N is distributed in a random way, as, for example, in photodetection. This implies that the primaries themselves are a noisy input, which produces more noisy output due to contribution of noisy secondaries. In this case, the excess noise factor is evaluated starting from the signal-to-noise ratio (SNR), which is defined as $SNR[X] = E[X]/\sqrt{Var[X]}$. With this approach, known for the characterization of amplifiers, the ENF is defined as the relative losses in signal to noise ratio from input N to output X:

  $$ENF[X] = \frac{SNR[N]^2}{SNR[X]^2} = \frac{E[N]^2/Var[N]}{E[X]^2/Var[X]} \tag{3.7}$$

  However, in the most common photodetection case, the number of photons and then the number of photoelectrons follow Poisson distribution, so E[N]=Var[N].

Let us now consider the production of secondary events and their modeling. If a single primary event (N = 1) produces a chain of secondary events all with the same probability p, then the total number of events in output X follows a geometric distribution. The basic hypothesis is, therefore, that a primary event can produce as a result only 0 or 1 for the next event (no double, triple, etc. event). This situation is shown in upper left scheme in Figure 3.6, as a single chain consisting of the single primary event (black circle) then the first and the second crosstalk events (red circles), and absence of the third crosstalk event (empty circle). This model works well for crosstalk events with low probability p and if the probability of a double event p^2 is considered negligible. In photon detection case, if the number of primary events N is a Poisson random variable with mean μ, then X follows a Compound Poisson distribution. Upper right scheme in Figure 3.6 reflects

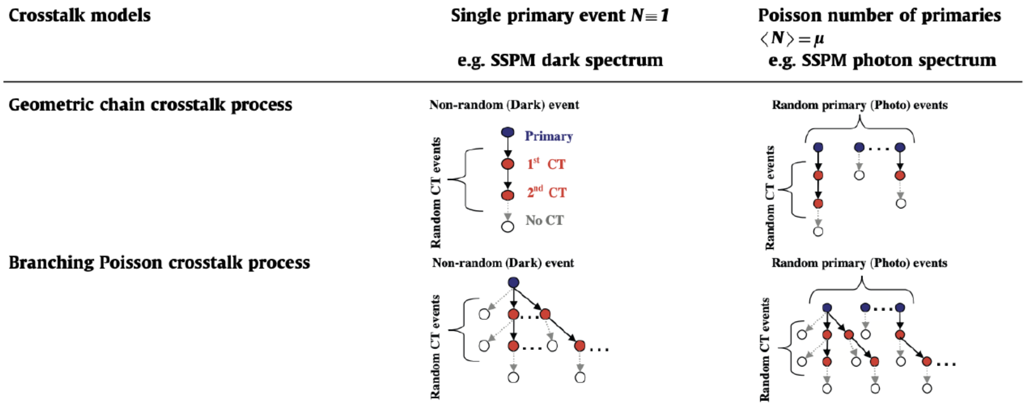

Figure 3.6: *Schematic overview of the crosstalk process models.*

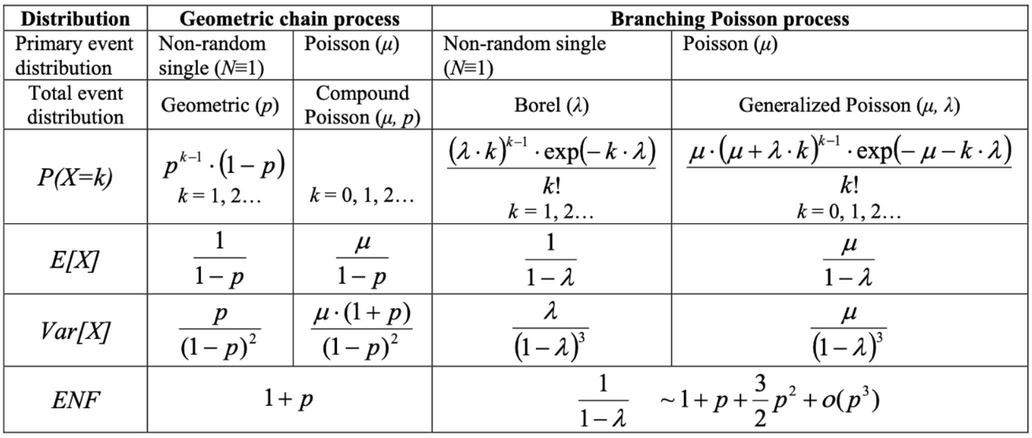

Distribution	Geometric chain process		Branching Poisson process	
Primary event distribution	Non-random single ($N\equiv1$)	Poisson (μ)	Non-random single ($N\equiv1$)	Poisson (μ)
Total event distribution	Geometric (p)	Compound Poisson (μ, p)	Borel (λ)	Generalized Poisson (μ, λ)
$P(X=k)$	$p^{k-1}\cdot(1-p)$ $k=1,2\ldots$	$k=0,1,2\ldots$	$\frac{(\lambda\cdot k)^{k-1}\cdot\exp(-k\cdot\lambda)}{k!}$ $k=1,2\ldots$	$\frac{\mu\cdot(\mu+\lambda\cdot k)^{k-1}\cdot\exp(-\mu-k\cdot\lambda)}{k!}$ $k=0,1,2\ldots$
$E[X]$	$\frac{1}{1-p}$	$\frac{\mu}{1-p}$	$\frac{1}{1-\lambda}$	$\frac{\mu}{1-\lambda}$
$Var[X]$	$\frac{p}{(1-p)^2}$	$\frac{\mu\cdot(1+p)}{(1-p)^2}$	$\frac{\lambda}{(1-\lambda)^3}$	$\frac{\mu}{(1-\lambda)^3}$
ENF	$1+p$		$\frac{1}{1-\lambda}\sim 1+p+\frac{3}{2}p^2+o(p^3)$	

Figure 3.7: *Summary of the essential analytical expressions for the crosstalk affected SiPM signals.*

this case as random number of geometric chains (1, 2, 3, ...) with random crosstalk events in each (0, 1, 2, ...). However, it would be reasonable to consider crosstalk events as a result of a large number of trials to trigger neighboring pixels with small probability of success in each trial, thus assuming Poisson distribution of the successful trials in a single (direct) generation of succeeding events. It means that one preceding event produces Poisson distributed random number of succeeding events and then again, until extinction, representing a branching Poisson process, as shown in lower left scheme in Figure 3.6. The probability distribution of X in branching processes may be found using recursive generating function approach. In the case where a single primary event (N = 1) generates a random number of secondary events Poisson distributed with mean λ, the distribution of the total number of events generated X follows the Borel distribution. If, instead, the number of primary events is Poisson distributed with mean μ, the total number of all events X is found to be a compound Poisson sum of Borel distributed random variables (lower right scheme in Figure 3.6). Thus, the statistics of X are governed by the Generalized (Lagrangian) Poisson distribution [71]. The essential expressions of our interest for both models are summarized in Figure 3.7.

The most direct way to compare the models with experimental results is a single-primary-event-initiated distribution analysis. It is often based on measurements of Dark Count Rate vs counter threshold level representing complementary cumulative distribution function of the crosstalk itself, if the overlapping of dark counts is negligible. The crosstalk probability p can be calculated from the experimental data in the following way:

$$p = \frac{DCR(1.5SER)}{DCR(0.5SER)} \tag{3.8}$$

3.1.4 SiPM impact on TAO energy resolution

As discussed in section 2.2.4, the performance of SiPMs plays a crucial role in reaching the required energy resolution below the $2\%/\sqrt{1MeV}$ in the TAO experiment, which is fundamental to achieve its physics goals. The energy resolution of a scintillation detector such as TAO can be written as the quadratic sum of three main contributions:

$$\left(\frac{\sigma_E}{E}\right)^2 = \frac{a^2}{E} + \frac{b^2}{E^2} + c^2, \tag{3.9}$$

where E is the deposited energy (typically expressed in MeV), and a,b, and c encode different physical effects. Several factors related to the SiPM have a direct impact on the different parameters of TAO energy resolution.

- **Stochastic term a^2/E :** The stochastic term originates from photoelectron statistics and correlated fluctuations in the photosensors:

$$\frac{a^2}{E} \simeq \frac{ENF}{N_{\mathrm{pe}}(E)} \tag{3.10}$$

  The photoelectron statistics $N_{\mathrm{pe}}(E)$ is given by:

$$N_{\mathrm{pe}}(E) = Y_\gamma \times E \times \varepsilon_{\mathrm{geom}} \times \varepsilon_{\mathrm{opt}} \times \mathrm{PDE}, \tag{3.11}$$

  where Y_γ is the scintillation light yield ($\sim$ 12.000 photons/MeV), $\varepsilon_{\mathrm{geom}}$ is the geometrical photosensor coverage ($\sim$ 95%), $\varepsilon_{\mathrm{opt}}$ is optical transport efficiency, i.e the fraction of scintillation photons produced in the liquid scintillator that actually reach the photosensors ($\sim$ 90%), and PDE is the photon detection efficiency of the SiPMs. In order to reach a photoelectron statistics of $\sim$ 4500 photoelectrons/MeV, TAO SiPMs have to exhibit a PDE $\sim$ 50%. Thanks to the very high detected light yield, the stochastic term dominates the energy resolution over a wide energy range. Without the excess noise factor, the purely Poisson stochastic limit at 1 MeV would be:

$$\left(\frac{\sigma_E}{E}\right)_{Poisson} \approx \frac{1}{\sqrt{4500}} \approx 1.5\% \tag{3.12}$$

  Nevertheless, as we have seen in the previous section, the excess noise factor acts as an effective degradation of photon statistics. In TAO, the dominant contributors to ENF are the optical crosstalk between neighboring SiPM microcells, delayed crosstalk and (to a much lesser extent) afterpulsing, gain and charge fluctuations of the SiPM–electronics chain. Optical crosstalk is the leading effect. In order to control the degradation of the photon statistics the requirement on the crosstalk probability is $p \leq 10\%$. This requirement refers to the nominal detector operating conditions optimized for physics data taking. During the SiPM characterization phase, a looser criterion ($p < 20\%$) was adopted in order to study device behavior over an extended range of overvoltage and operating conditions, to account for production spread, and to ensure sufficient performance margins.

- **Noise term b^2/E^2 :** The noise term represents energy-independent additive fluctuations, mainly arising from SiPM dark counts, electronic noise and baseline fluctuations. The main contribution to the noise term is due to the dark count rate, which is required to be $DCR < 100$ Hz/mm^2 at −50 °C. Other contributions come from the charge resolution, i.e the precision with which each SiPM channel and the front-end electronics can measure the integrated charge of a single photoelectron (signle photoelectron resolution, RES), and the signal-to noise ratio, which takes into account the baseline fluctuations due to the electronic noise. During the SiPM characterization, the criteria choosen for these two figures of merit are $RES < 15\%$ and $SNR > 10$.

- **Constant term c^2 :** The constant term accounts for energy-independent fractional effects and is dominated by residual non-uniformities and calibration systematics, such as imperfect corrections of light collection, SiPM gain and PDE variations, crosstalk modeling, and long-term stability of operating conditions.

The relative importance of these three contributions depends on the energy range. The stochastic term dominates at low energies, where the finite number of detected photoelectrons limits the resolution. The noise term becomes relevant at very low energies, where electronic noise and dark counts contribute significantly to the signal. The constant term, instead, becomes dominant at high energies, where energy-independent effects such as detector non-uniformities and calibration uncertainties set a lower bound to the achievable resolution. In the energy range relevant for reactor antineutrino detection, typically a few MeV, the resolution is mainly driven by the stochastic term, with smaller contributions from the other components.

3.1.5 TAO Silicon Photomultipliers

The purpose of the TAO experiment is to accurately measure the spectrum of primary antineutrinos originating from nuclear reactors. To achieve the required energy resolution of less than 2% at 1 MeV, it is crucial to maximize light detection efficiency and minimize noise levels. SiPMs operating at low temperature, in particular, are the most interesting application for the newly large particle detectors for neutrinos and dark matter experiments, being able to detect extremely weak light. Compared to conventional PhotoMultiplier Tubes, SiPMs exhibit several advantages, including excellent single Photon Detection Efficiency (PDE > 50 %), insensitivity to magnetic fields, good radiopurity, low operating voltage (∼50 V), and compact design. But, as we have seen in the previous section, they also have two drawbacks, namely the high dark count rate and the high probability of correlated avalanches (optical cross-talk and after-pulses), which could trigger the SPADs without impinging photons resulting in increasing noise, potentially compromising detector performance, in particular the energy resolution. In order to reduce the dark noise by about three orders of magnitude compared to room temperature, the TAO detector operates at a cryogenic temperature of −50 °C.

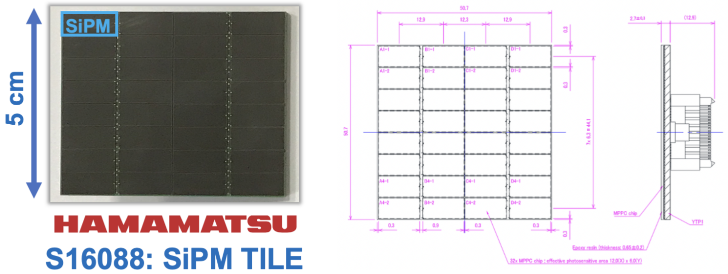

Figure 3.8: *Picture and schematization of the Hamamatsu S16088 SiPM tile employed for TAO.*

Given the large surface of $\sim 10\ m^2$ of the acrylic sphere containing the liquid scintillator, the SiPMs employed for the Central Detector have been specifically assembled by Hamamatsu Photonics K.K. [72] in 4024 large arrays (tiles) of 8x4 independent elements of $12 \times 6\ mm^2$ each (S16088 series). The overall area of the tiles is $50 \times 50\ mm^2$. Figure 3.8 shows a picture and the schematization of the assembled tile. Each SiPM element is covered by an epoxy resin window and includes 12,782 SPADs with a pixel pitch of 75 μm, a breakdown voltage around 50 V at +25 °C and a peak sensitivity wavelength at 450 nm [72]. Each microcell is equipped with an integrated quenching resistor, used to stop the Geiger discharge after avalanche triggering, of the order of 100–200 $k\Omega$.

3.2 TAO Front-end electronics

As previously mentioned, each SiPM tile consists of 32 elements. In order to reduce the number of readout channels, the outputs of different SiPM elements have to be coupled together and their outputs have to be merged into a single analog output by means of dedicated front-end electronics. In the electronics readout scheme, shown in Figure 3.9, the SiPM tiles are connected to the Front-End Boars (FEBs), which split them into 2 independent channels of 16 combined SiPM elements (corresponding to half tile), with serial/parallel connections, for 8,048 overall differential signals. Those are subsequently sampled and read by means of a custom ADC board, managed by the FPGA-based Front-End Controllers (FECs), which digitizes the signal coming from each channel and performs signal pre-processing. Each FEC will work as a White Rabbit (WR) node [73] to ensure synchronous acquisition from the whole detector. In order to simplify the connections, reduce the number of cables and allow the passage of the cables in and out of the cryogenic tank, there are dedicated flanges for the output signals and

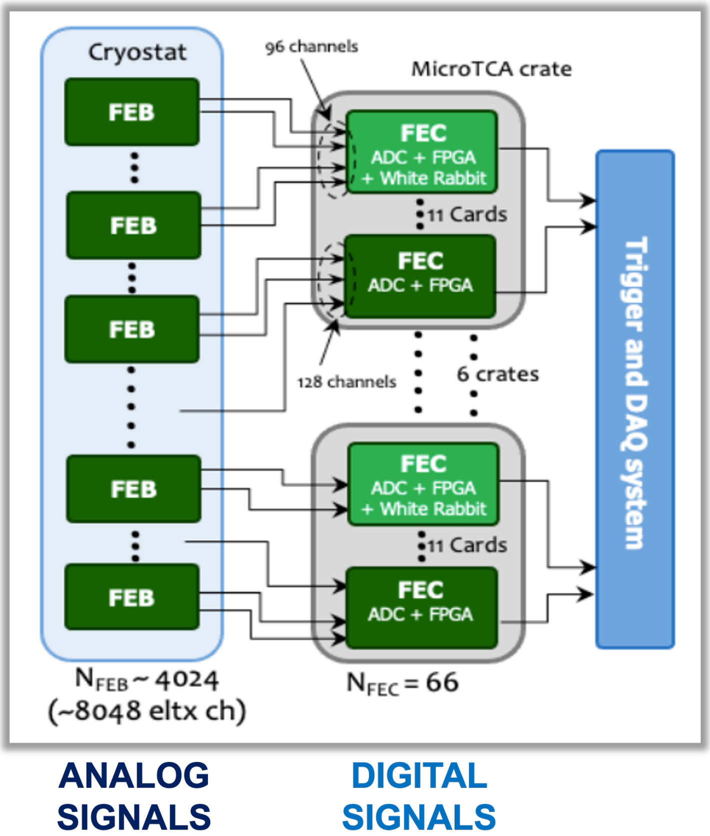

Figure 3.9: *Overall block design of the TAO readout electronics, mainly divided in Front-End Board interfaces, FPGA-based Front-End Controllers with ADC devices and Data Acquisition System.*

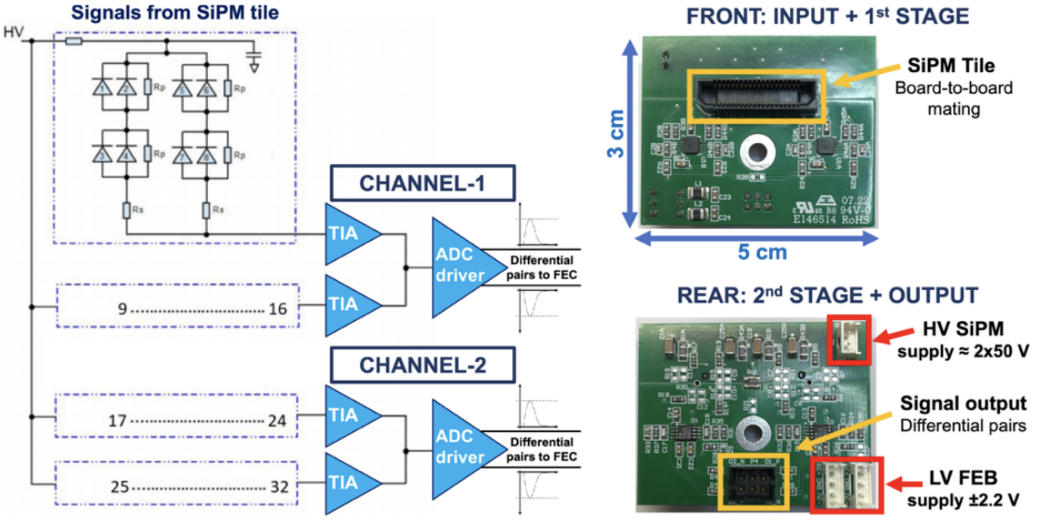

Figure 3.10: *Block scheme of the FEB connections and SiPM signals routing, and pictures of the front and rear side of the board,with input and output connectors highlighted.*

the power supply for the FEBs. The raw data, in terms of charge and time information ($Q\&T$), will be collected through optical fiber connections by the Data Acquisition (DAQ) system, that will filter and record occurring events. The FECs and the Trigger-DAQ system are hosted on μTCA (Micro Telecommunications Computing Architecture) crates outside the cryostat.

3.2.1 Front-End Board

The Front-End Board (FEB), directly coupled to the 25 cm^2 SiPM tile, supplies power to the photosensors and amplifies the output signals at cryogenic temperature. It consists of a 2-stage amplifier: a TransImpedance Amplifier (TIA: Analog Devices LTC6269, Dual 500 MHz Ultra-Low Bias Current FET Input OpAmp [74]) and a differential driver (Analog Devices LTC6405 Low Noise, Rail-to-Rail Input Differential Amplifier/Driver [75]). The overall amplification factor of the FEB is about 16 kV/A, resulting from the combination of the transimpedance stage (8.2 kV/A) and the subsequent voltage amplification stage (1.95 V/V). The tile is splitted in 4 quadrants (with 8 elements each, corresponding to the series of 4 SiPMs parallel-connected) and each quadrant is read-out with an independent TransImpedance Amplifier. The voltage signals coming from 2 TIAs (half-tile) are then summed and routed to one of the two differential drivers on the board, employed in order to output the signals as analog differential pairs, thus allowing the use of ~14

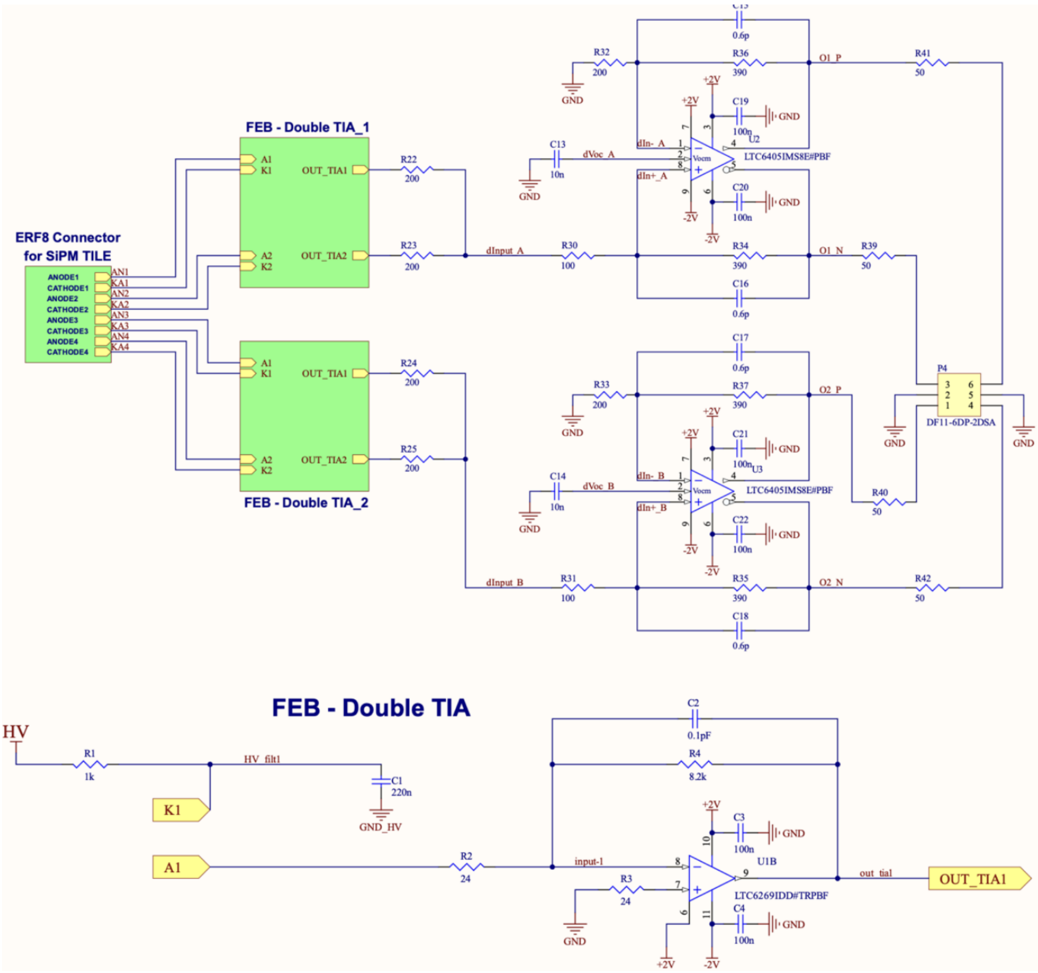

Figure 3.11: *Schematics of the Front-End Boards design: overall scheme and detailed TransImpedance Amplification stage.*

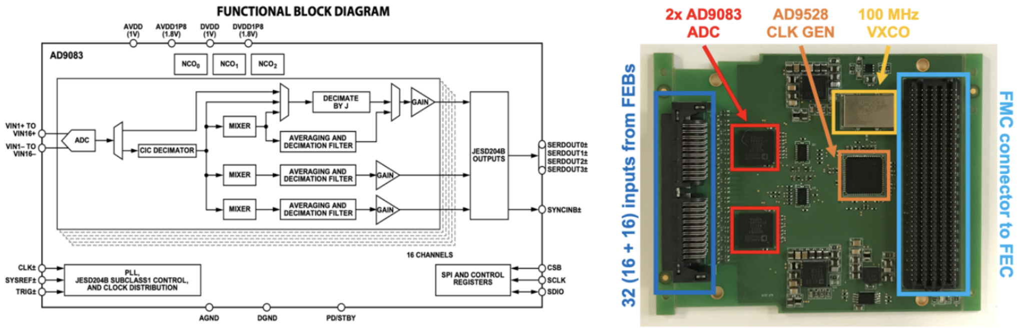

Figure 3.12: *AD9083 functional block and a picture of the front side of the ADC board with 32 differential inputs, 2 AD9083 devices and an FMC connector for the power supply and output signals.*

m twisted cable preventing additional noise. Figure 3.10 shows the simplified block scheme and the pictures of the front and rear side of the FEB, made with low radioactivity Aramid Printed Circuit Board (PCB) substrate. The board dimension is $50 \times 30\ mm^2$, so it can be perfectly arranged with the $50 \times 50\ mm^2$ Hamamatsu S16088 SiPM tile. The series/parallel connections between the independent SiPM elements of the tile are performed by the FEB itself, as well as the High-Voltage (HV) power supply of the photosensors. The recommended operating voltage (V_{OP}) for each element of the tile at $-50\,°\mathrm{C}$, corresponding to +3 V the SiPM breakdown voltage (V_{BR}), is ~ 50 V. Since there are series connections between the SiPM elements, the HV power supply must be doubled: $\sim 2 \times 52$ V. Moreover, each FEB is biased with a Low Voltage (LV) power supply at ±2.2 V to feed the TIAs and the differential drivers, with an absorption of ±80 mA at $-50\,°\mathrm{C}$. By means of the double LV connectors on the boards, they can be supplied in a row. Figure 3.11 shows the schematics of the Front-End Boards design, with the optimized values for the resistors and the capacitors. The implemented TIA scheme is a standard one with a small feedback capacitance (C2 in the figure) that can be added to compensate the effect of the input SiPM capacitance. The amplifier gain V/I can be modified by changing the feedback resistance value (R4 in the figure).

3.2.2 ADC and Front-End Controller

Outside the cryostat, the differential signals coming from the FEBs are digitized and collected by a custom ADC board, managed by the Front-End Controllers (FECs). The FEC is based on a Xilinx Kintex 7 UltraScale FPGA and can control up to eight 16-channel ADCs, for a total of 128 chan-

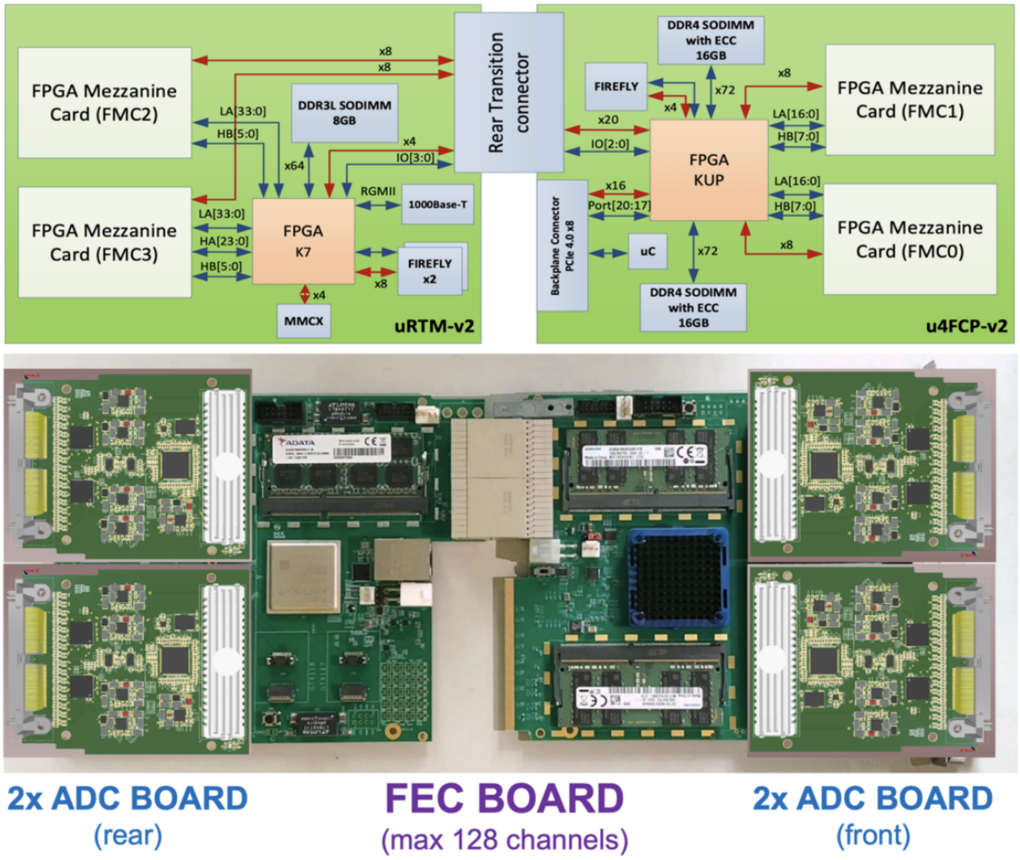

Figure 3.13: *Block design of the FPGA board, and the overall Front-End Controller with 4 ADC boards connected by means of the FMC connectors.*

nels. The design of the ADC board has been defined with 32 differential input channels and an FPGA Mezzanine Card (FMC) connector for the power supply and for the connection with the FEC. The ADC board is based on the AD9083 16-channel, 250 MS/s, 125 MHz bandwidth, Continuous Time SD (CTSD) ADC, by Analog Devices Inc. with 2 VPP differential input voltage [76]. The analog input and clock signals are differential inputs, whereas the 4 digital outputs are designed to the JEDEC standard JESD204B, a protocol to link the AD9083 to a digital processing device over a serial interface with lane rate of up to 16 Gbps. Moreover, by means of a Serial Peripheral Interface (SPI) it is possible to control various product features and functions to meet specific system requirements (e.g. power mode, digital filtering, data encoding and output interface configuration). As shown in Figure 3.12, there are 2 AD9083 on the PCB, thus a single board can read data from 16 SiPM tiles, with a maximum sampling rate of 250 MHz with 12-bit resolution (or

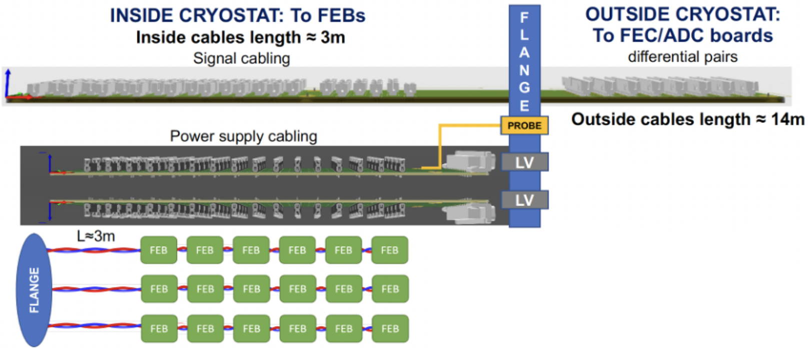

Figure 3.14: *Schematization of the flange cabling used in the TAO experiment.*

16 bits at 125 MHz). All the ADCs will work in free running mode and the collected data will be analyzed and pre-processed on the FPGA itself searching for the pulses related to the collected photoelectrons. Each FEC can control up to 4 ADC board, by means of the High Pin Count FPGA Mezzanine Cards (HPC-FMCs). 128 FECs are needed for the 4024 SiPM tiles. All the FPGA boards will act as White Rabbit nodes to ensure sub-nanosecond synchronization. Digitized data collected by the FPGA is sent outside the cryostat via an optical fiber link. Figure 3.13 shows the block design of the FPGA board (details in [77]), and a representation of the overall Front-End Controller with 4 ADC boards connected by means of the 4 HPC-202 FMCs on the board.

Flange cabling

To decrease the number of cables and to simplify the connections in the TAO central detector, 8 flanges with 8 signal PCB boards and 2 power supply PCB boards each are used. Figure 3.14 shows a schematization of the flange cabling. Since the number of differential pairs for signal readout is 8048 (2 channels per FEB), there are 8 overall flanges with 1006 differential pairs each. On each flange there are 8 signal feedthrough PCBs and 2 power feedthrough PCBs. Each flanges supplies 512 FEBs, so FEBs are subdivided in $\sim$ 86 rows with 6 FEBs each.

3.3 First tests on FEBs with SiPM tiles

After finalizing the design of the Front-End boards, several preliminary tests were performed on the FEBs coupled with TAO SiPM tiles, Hamamatsu S16088 [72], at a criogenic temperature of −50 °C to emulate the working conditions of the TAO detector. The tests were carried out in the laboratories of the National Institute of Nuclear Physics (INFN) at Roma Tre University in collaboration with the JUNO group of Roma Tre. The goal of this first characterization was to show the correct behavior of the SiPM tiles coupled with the finalized FEBs. In particular, the breakdown voltage of the SiPM tile has been derived through the voltage-current characteristic. Then, we studied the response of the SiPM tile coupled with the Front-End boards in laser and dark conditions, performing preliminary analysis on the multi-photon spectrum in order to derive important figures of merit of the SiPMs such as the signal-to-noise ratio, the single photoelectron resolution and the crosstalk rate. Finally, the dark count rate of the SiPM tile has been measured.

3.3.1 Experimental setup

The experimental setup used for the preliminary tests is shown in Figure 3.15. During the tests, one FEB and one SiPM tile was tested at one time, resulting in two overall channels. The setup consisted of:

- A climate chamber from ACS, model DY200 C, which allows operating at cryogenic temperatures up to −70 °C.
- A very low intensity UV light-pulser from Hamamatsu, model C8898. The photons are emitted with $\lambda = 407$ nm, in the range of typical scintillation photon wavelengths, with a pulse duration of 80 picoseconds. The laser is coupled to an optical fiber, through which the SiPM tiles are illuminated.
- Two power supplies: a high-voltage (HV) generator from Elind, model 180 P5, for the SiPM tiles supply ($\sim$ 100 V at −50 °C), and a low-voltage (LV) generator from Elind, model 32DP16, for biasing the integrated circuits on the board (±2.2 V).
- 1 $\sim$14 m twisted cable for carrying the FEB output differential signals and a transformer to recombine the FEB output differential signals.
- A digital oscilloscope from Teledyne-Lecroy, model WavePro804HD, for data acquisition and preliminary analysis.

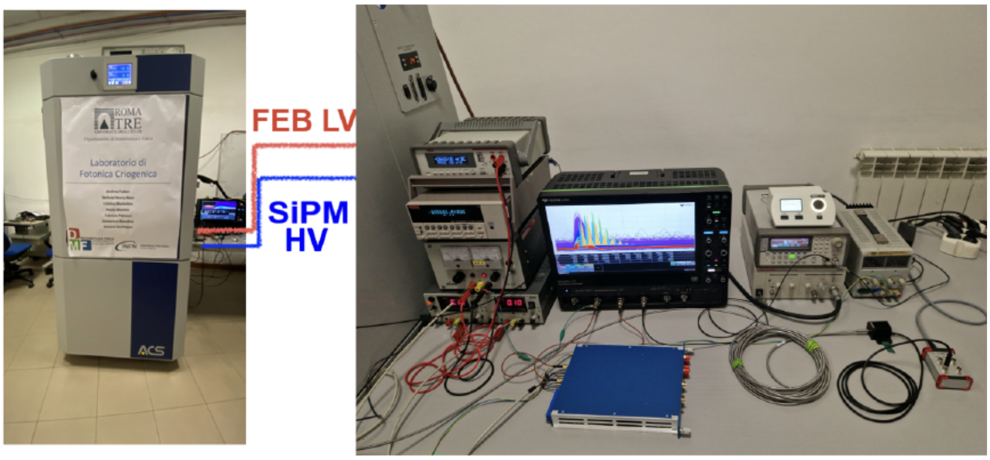

Figure 3.15: *Pictures of the experimental setup used for the first characterization of the FEBs coupled with the SiPM tile. On the left, the climate chamber used to operate at* $-50\,^{\circ}\mathrm{C}$*. On the right, the supply and readout system.*

3.3.2 Voltage-current characteristic

The first step in these preliminary measurements was to identify the breakdown voltage of the SiPM tiles. To do it, the voltage-current (V-I) characteristic, which is the trend of the current generated by the SiPM as a function of the applied supply voltage V_{bias}, was investigated. The V-I characteristic can be obtained by placing the SiPM in a dark environment and measuring the current produced as a function of the voltage supplied. For low values of the reverse bias voltage, the current varies linearly with V_{bias}. Once a certain threshold is exceeded, which coincides with the breakdown voltage V_{BD}, the current intensity increases significantly, thus allowing greater amplification. The dependence of the current on the reverse bias voltage near the breakdown voltage is of quadratic type since both the gain and the thermal noise frequency depend linearly on the overvoltage:

$$I = \frac{\Delta Q}{\Delta t} = Gain \times e \times DCR \propto \Delta V^2 \tag{3.13}$$

Moreover, the breakdown voltage of a SiPM decreases with decreasing temperature, since impact ionization in silicon becomes more efficient at lower temperatures, allowing charge carriers to gain higher kinetic energy between collisions. Consequently, a lower electric field, and therefore a lower bias voltage, is sufficient to trigger the avalanche. Figure 3.16 shows the voltage-current characteristics for one of the two readout channels of the S16088 SiPM tile, at room temperature (25 °C) and at −50 °C. The breakdown voltage is then obtained as the starting point of the parabolic trend of the V-I curve:

- $V_{bd} \simeq 51$ V at 25 °C
- $V_{bd} \simeq 47$ V at −50 °C

Using this approach, we derived a temperature coefficient of 54 mV/°, which allows the breakdown voltage of the single SiPMs to be obtained at different temperatures:

$$V_{bd}(-50°\text{C}) = V_{bd}(25°\text{C}) - 0.054V/°\text{C} \times 75°\text{C} \tag{3.14}$$

In the following measurements, the SiPM tiles have been biased with an overvoltage of $V_{ov} = +3V$, leading to an overall operative bias of $V_{OP} \simeq 100V$ for the whole SiPM tile.

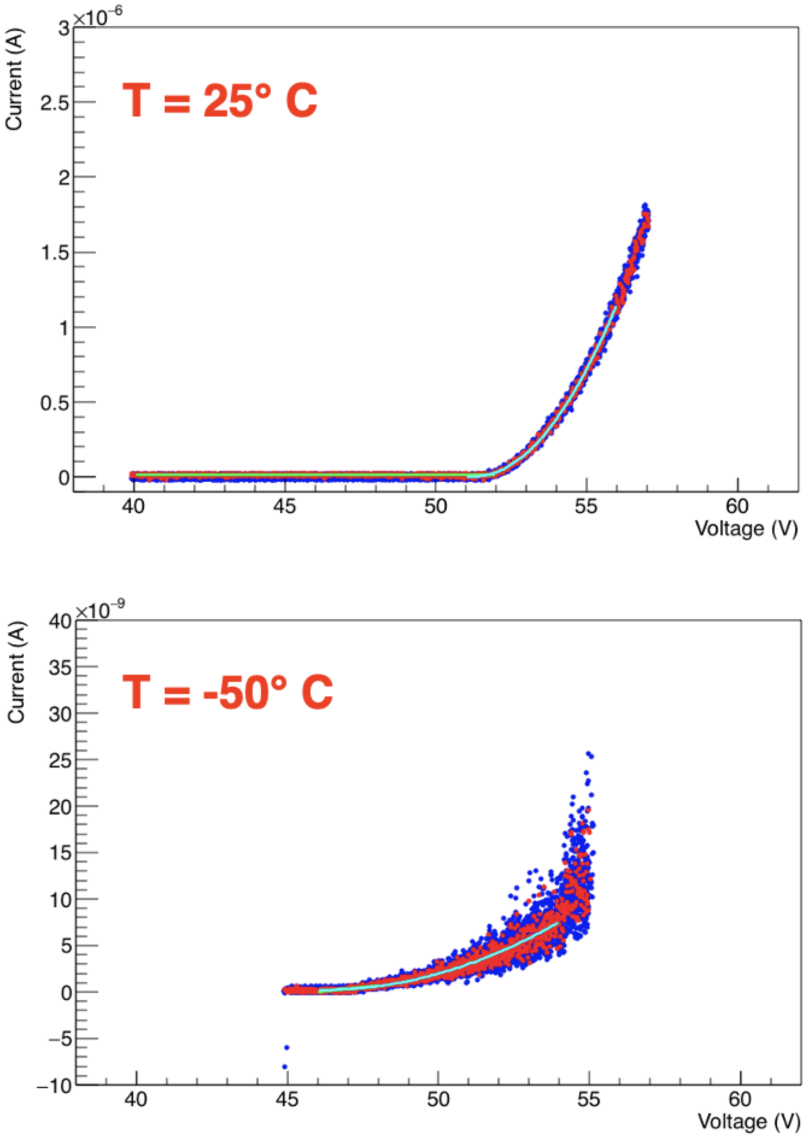

Figure 3.16: *Voltage-current characteristics of the Hamamatsu S16088 SiPM tile, at* 25 °C *and* −50 °C*. The breakdown voltage is obtained as the starting point of the parabola.*

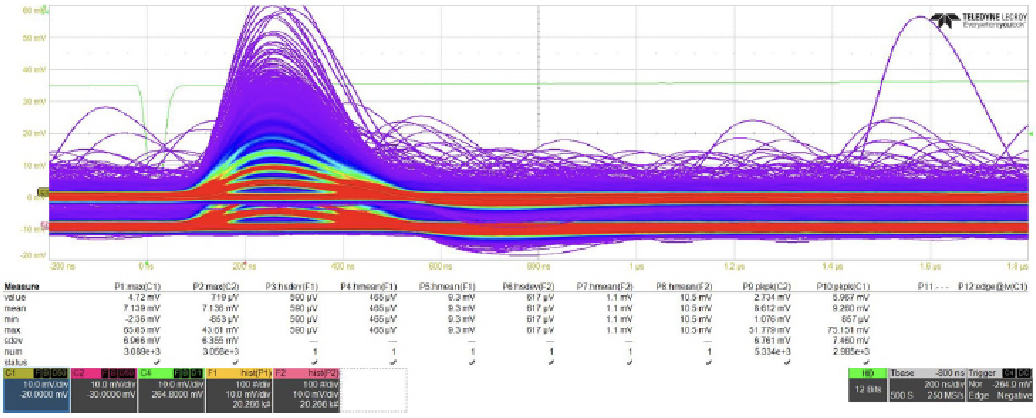

Measure	P1:max(C1)	P2:max(C2)	P3:hsdev(F1)	P4:hmean(F1)	P5:hmean(F1)	P6:hsdev(F2)	P7:hmean(F2)	P8:hmean(F2)	P9:pkpk(C2)	P10:pkpk(C1)	P11:---	P12:edge@lv(C1)
value	4.72 mV	719 µV	580 µV	465 µV	9.3 mV	817 µV	1.1 mV	10.5 mV	2.734 mV	5.967 mV		
mean	7.139 mV	7.136 mV	580 µV	465 µV	9.3 mV	817 µV	1.1 mV	10.5 mV	8.612 mV	9.260 mV		
min	-2.38 mV	-863 µV	580 µV	465 µV	9.3 mV	817 µV	1.1 mV	10.5 mV	1.076 mV	867 µV		
max	63.65 mV	43.61 mV	580 µV	465 µV	9.3 mV	817 µV	1.1 mV	10.5 mV	51.779 mV	75.151 mV		
sdev	6.966 mV	6.355 mV	---	---	---	---	---	---	6.761 mV	7.460 mV		
num	3.089e+3	3.056e+3	1	1	1	1	1	1	5.334e+3	2.985e+3		
status	✓	✓	✓	✓	✓	✓	✓	✓	✓	✓		

C1 10.0 mV/div -20.0000 mV
C2 10.0 mV/div -30.0000 mV
C4 10.0 mV/div 264.8000 mV
F1 hist(P1) 100 #/div 10.0 mV/div 20.266 k#
F2 hist(P2) 100 #/div 10.0 mV/div 20.266 k#
HD 12 Bits
Tbase -800 ns 200 ns/div 500 S 250 MS/s
Trigger C4 DC Nor -264.0 mV Edge Negative

Figure 3.17: *Visualization through a digital oscilloscope of the SiPM tile's response to a photon beam at* $T = -50\,^{\circ}\mathrm{C}$

3.3.3 Response spectra with laser

The signal formation in the SiPM–front-end chain can be described as follows. Incident scintillation photons generate avalanches in the SiPM microcells, producing fast current pulses. These signals are shaped and amplified by the front-end electronics, resulting in a voltage waveform as a function of time. The total collected charge is obtained by integrating this waveform over a predefined time interval (integration window). This integrated charge is proportional to the number of detected photoelectrons and represents the fundamental observable used to build the response spectra discussed in this section. The measurement was performed in photon-counting mode, counting the number of pulses linked to avalanches generated by incident photons. Using the Hamamatsu laser at minimum power, pulses containing very few photons were sent to the SiPM tile at a frequency of 200 kHz. The laser was also used to send the trigger to the digital oscilloscope, through which the output voltage from the FEB is displayed as a function of time. Figure 3.17 shows the response of the tile to the low-intensity beam of incident photons displayed on the digital oscilloscope. As can be seen from the Figure, the typical duration of charge and discharge processes of the SiPM tile in response to impinging photons is $\sim$ 500 ns. Using the oscilloscope, the voltage maximums were sampled in the $\sim$ 500 ns time window for each trigger. Counting the number of times that the maximums occur we obtain the multi-photon spectrum (so-called finger plot). The voltage corresponding to the production of a single photoelectron is of the order of millivolts, in our case $\sim$ 5 mV. Therefore, several peaks appear in the finger plots: the first, called the pedestal, is due to the electronic noise of the FEB, and therefore represents a count of 0 photons per trigger; the second peak corresponds to the number of counts of 1 photoelectron produced per trigger, the third peak to 2 photoelectrons, and so on. Multi-photon spectrum analysis, as discussed in section 3.1.1, consists of performing Gaussian fits of the peaks corresponding to the number of counts of the collected photoelectrons for each trigger. Two important quantities can be evaluated through this type of analysis in laser condition:

- **Signal-to-noise ratio (SNR):** Given the distributions of the counts corresponding to 1 photoelectron and to the pedestal, it is defined as the ratio of the distance between the mean values of the two peaks and the standard deviation of the pedestal:

$$SNR = \frac{\mu_1 - \mu_0}{\sigma_0} \tag{3.15}$$

- **Single photoelectron resolution (RES):** From the distribution of the counts of 1 photoelectron, it can be evaluated as the ratio between the mean and the standard deviation of the gaussian fit of the peak:

$$RES = \frac{\sigma_1}{\mu_1} \times 100 \tag{3.16}$$

In these preliminary analysis, 5 FEBs were tested, coupled with the same SiPM tile. Figure 3.18 shows, as an example, two finger plots of the two output channels of one of the tested FEBs, obtained illuminating the SiPM tile coupled with the Front-End boards. The average values of the signal-to-noise ratio and of the single photoelectron resolution obtained from the gaussian fits performed on all the 10 multi-photon spectra are the following.

- $\langle \text{SNR} \rangle = 7.51 \pm 0.36$
- $\langle \text{RES} \rangle = (14.65\% \pm 0.91)\%$

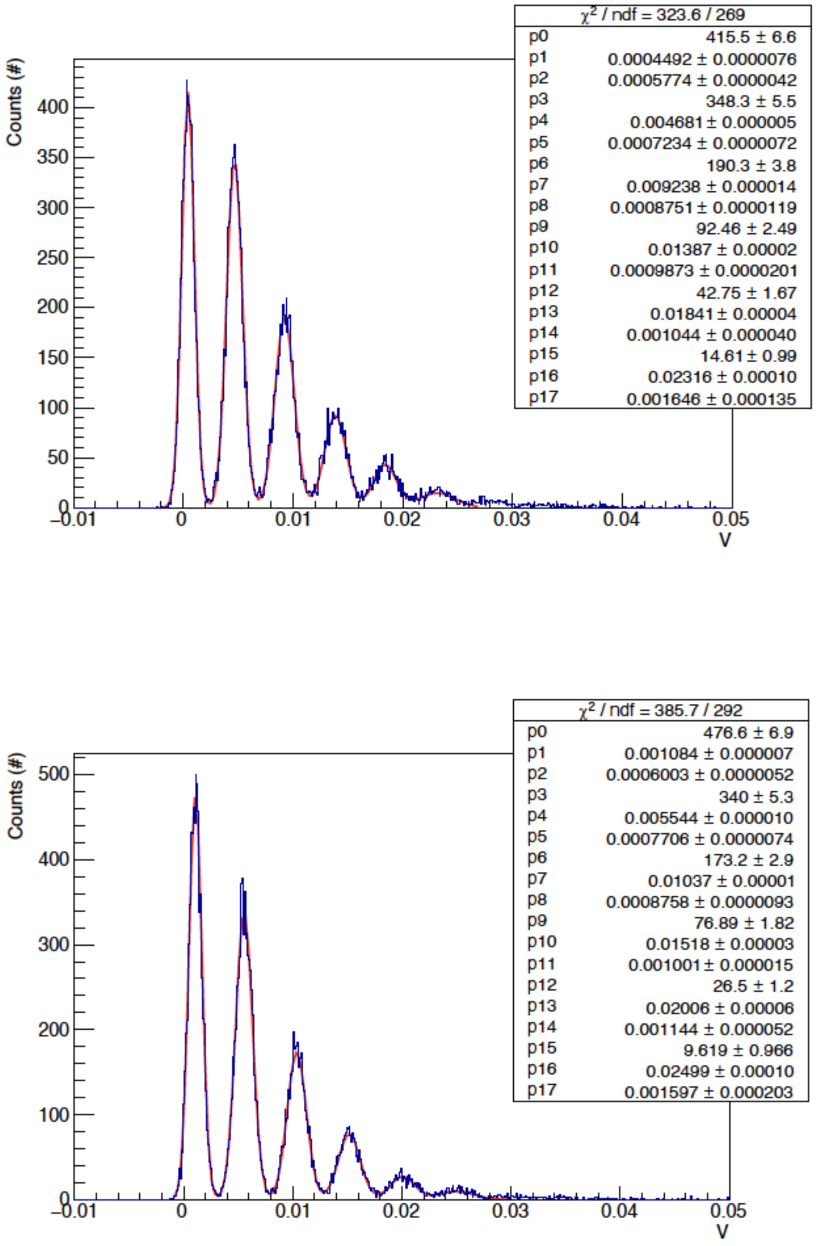

Figure 3.18: *Example of finger plots of two channels of a tested SiPM tile coupled with the FEB in laser condition at −50 °C. On each peak a gaussian fit is performed.*

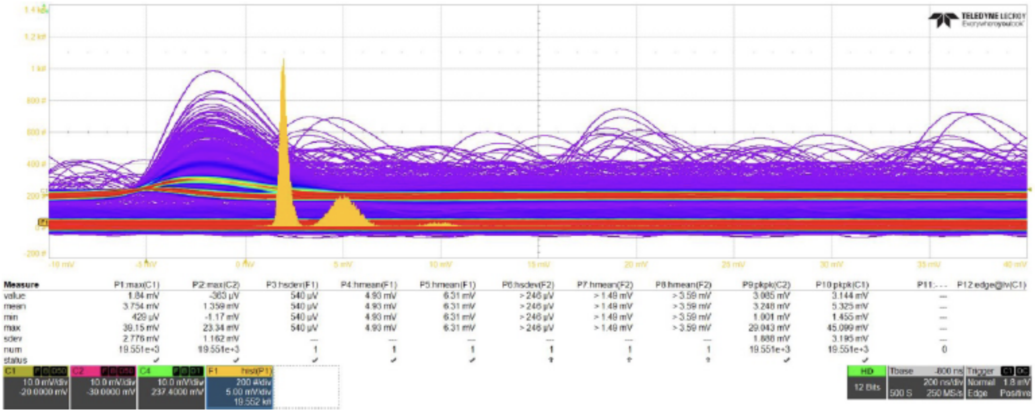

Measure	P1:max(C1)	P2:max(C2)	P3:hsdev(F1)	P4:hmean(F1)	P5:hmean(F1)	P6:hsdev(F2)	P7:hmean(F2)	P8:hmean(F2)	P9:pkpk(C2)	P10:pkpk(C1)	P11:---	P12:edge@lv(C1)
value	1.84 mV	-363 µV	540 µV	4.93 mV	6.31 mV	> 246 µV	> 1.49 mV	> 3.59 mV	3.085 mV	3.144 mV	---	
mean	3.754 mV	1.359 mV	540 µV	4.93 mV	6.31 mV	> 246 µV	> 1.49 mV	> 3.59 mV	3.248 mV	5.325 mV	---	
min	429 µV	-1.17 mV	540 µV	4.93 mV	6.31 mV	> 246 µV	> 1.49 mV	> 3.59 mV	1.001 mV	1.455 mV	---	
max	39.15 mV	23.34 mV	540 µV	4.93 mV	6.31 mV	> 246 µV	> 1.49 mV	> 3.59 mV	29.043 mV	45.099 mV	---	
sdev	2.776 mV	1.162 mV	---	---	---	---	---	---	1.888 mV	3.195 mV	---	
num	19.551e+3	19.551e+3	1	1	1	1	1	1	19.551e+3	19.551e+3	0	
status	✓	✓	✓	✓	✓	↑	↑	↑	✓	✓		

Figure 3.19: *Visualization through a digital oscilloscope of the SiPM tile output signal in dark conditions at* $T = -50\,^{\circ}\mathrm{C}$ *and the corresponding histogram of the maximums.*

3.3.4 Response spectra in darkness

Another very important measure is the study of the response of the SiPM tile in dark conditions. In this case, in addition to the signal-to-noise ratio and the resolution on the single photoelectron, it is possible to quantify the contribution of the optical crosstalk, as we saw in section 3.1.3. In fact, with some frequency, the thermal noise causes the production of a dark photoelectron, which can subsequently produce one or more secondary photoelectrons by activating adjacent cells through optical crosstalk. Without any incident photon, the occurrence of this correlated noise can be evaluated. Figure 3.19 shows the output signal of the tile in dark condition displayed on the digital oscilloscope, as well as the histogram of the maximums. In this case, measurements of the output signal of the SiPM tile in dark conditions were made by setting a manual self-trigger of the FEB on the oscilloscope, equal to ~1/4 of a photoelectron, corresponding to 1.8 mV in our case. In the same way as for the laser condition, in the dark configuration the voltage maximums were sampled in the ~ 500 ns time window for each trigger. From the dark multi-photon spectrum it is therefore possible to evaluate the signal-to-noise ratio, the resolution on the single photoelectron and the optical crosstalk rate:

- **Signal-to-noise ratio (SNR):** Also for the dark configuration, the SNR is defined as the ratio of the distance between the mean values of the two peaks and the standard deviation of the pedestal:

$$SNR = \frac{\mu_1 - \mu_0}{\sigma_0} \tag{3.17}$$

- **Single photoelectron resolution (RES):** As well as for the laser configuration, the RES can be evaluated as the ratio between the mean and the standard deviation of the gaussian fit of the peak:

$$RES = \frac{\sigma_1}{\mu_1} \times 100 \tag{3.18}$$

- **Crosstalk rate (XTLK):** The optical crosstalk rate is evaluated by calculating the ratio between the areas of the last peaks ($A_{p>2}$) and the area of the second peak (A_{p2}), which are obtained as a result of the gaussian fit, and correspond to the fraction of the number of events in the peaks corresponding to two or more photoelectrons detected (N_{2+}) and the number of events in the peak of the first photoelectron (N_1).

$$XTLK = \frac{A_{p>2}}{A_{p2}} = \frac{N_{2+}}{N_1} \tag{3.19}$$

Also in this case, 5 FEBs have been tested, coupled with the same SiPM tile. Figure 3.20 shows, as an example, two finger plots obtained from the output channels of one of the tested FEBs coupled with the SiPM tile in darkness. The average values of the signal-to-noise ratio, of the single photoelectron resolution, and the cross talk rate obtained from the gaussian fit performed on the 10 channels are the following:

- $\langle \mathrm{SNR} \rangle = 13.55 \pm 0.93$
- $\langle \mathrm{RES} \rangle = (14.63 \pm 0.92)\%$
- $\langle \mathrm{XTLK} \rangle = (15.00 \pm 1.16)\%$

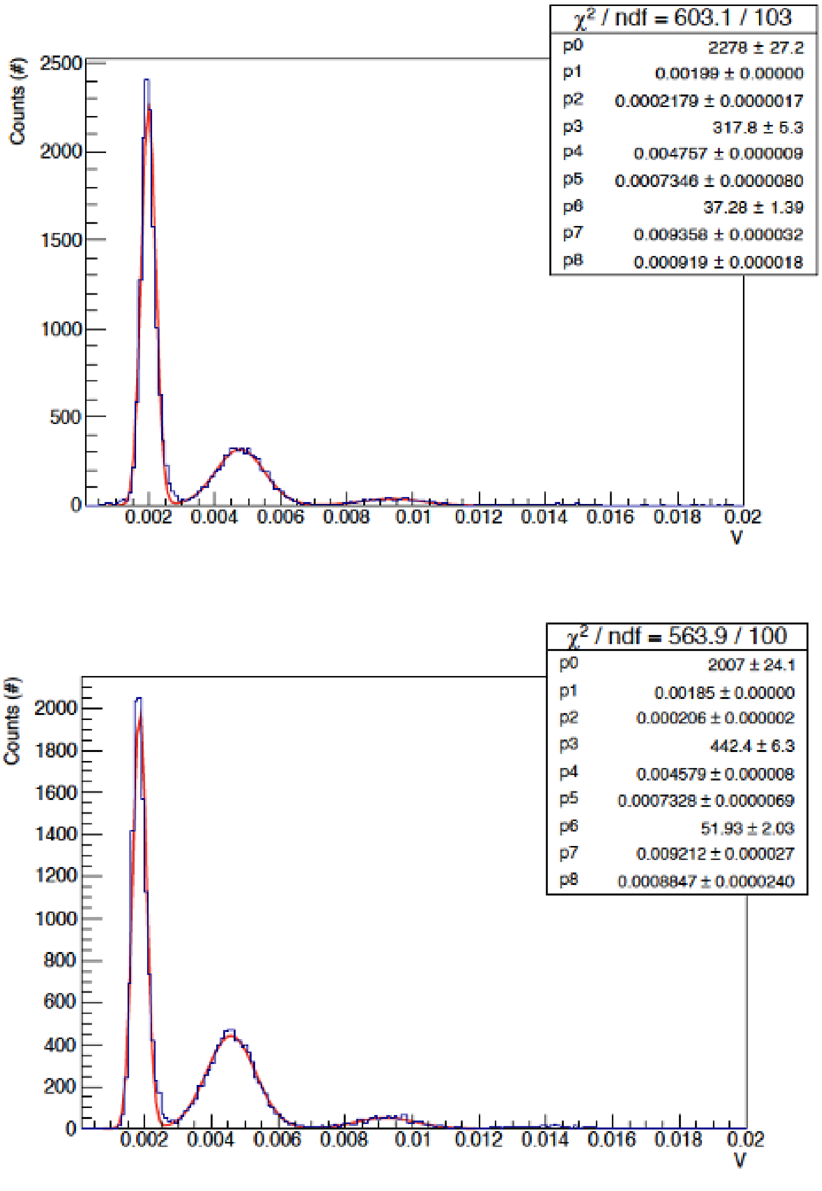

Figure 3.20: *Example of finger plots of the channels of a tested SiPM tile coupled with the FEB in dark conditions at −50 °C. On each peak a gaussian fit is performed.*

Measure	P1:max(C1)	P2:max(C2)	P3:edge@lv(C1)	P4:edge@lv(C2)	P5:hmean(F1)	P6:hsdev(F2)	P7:hmean(F2)	P8:hmean(F2)	P9:area(C2)	P10:area(C1)	P11:hmean(F6)	P12:hmean(F7)
value	5.85 mV	11.81 mV	26	38	---	> 298 µV	> 3.0 mV	> 6.2 mV	107.6680564 nWb	-28.2510658 nWb	-39.87 nWb	107.59 nWb
mean	> 8.208 mV	> 8.455 mV	30.147	34.555	---	> 298 µV	> 3.0 mV	> 6.2 mV	107.296 nWb	-39.715 nWb	< -39.87 nWb	107.59 nWb
min	> 1.90 mV	> 2.18 mV	12	10	---	> 298 µV	> 3.0 mV	> 6.2 mV	86.69012821 nWb	-112.641094 nWb	< -39.87 nWb	107.59 nWb
max	> 15.48 mV	> 15.48 mV	81	56	---	> 298 µV	> 3.0 mV	> 6.2 mV	123.1798382 nWb	-15.5404211 nWb	< -39.87 nWb	107.59 nWb
sdev	> 3.430 mV	> 3.403 mV	5.548	5.689	---	---	---	---	5.097 nWb	8.042 nWb	---	---
num	6.990e+3	6.990e+3	6.990e+3	6.990e+3	0	1	1	1	6.990e+3	6.990e+3	1	1
status	✓	✓	✓	✓	⚠	⚠	⚠	⚠	✓	✓	✓	✓

C1 F B D50 2.00 mV/div -1.20000 mV

C2 F B D50 2.00 mV/div -1.20000 mV

HD 12 Bits

Tbase -500 µs 100 µs/div 250 kS 250 MS/s

Trigger C1 DC Auto 2.40 mV Edge Positive

Figure 3.21: *Visualization of the dark counts of the two channels of the SiPM tile on the digital oscilloscope within the time window of 1 ms.*

3.3.5 Dark count rate

Another fundamental parameter for characterizing SiPMs is, as we have seen in section 3.1.2, the evaluation of the dark count rate. The DCR was measured by placing the tile and the FEB inside the climate chamber, under dark conditions, at $T = -50\,°\mathrm{C}$. To evaluate the frequency of dark counts, due to thermal noise and crosstalk effects, a special digital oscilloscope utility called edgelevel was used. The edgelevel function allows a time window to be set within which we count the number of times the output signal of the SiPM tile exceeds a certain threshold voltage value. The threshold was set to the voltage value at which occurs the separation between the first and second peak of the dark response spectra, corresponding to the pedestal and to the first photoelectron produced; in this way, in fact, it is certain that the edgelevel function only counts voltage values corresponding to the production of at least 1 dark photoelectron, and consequently, it never activates for voltage values corresponding to electronic noise. Therefore, by interpolating the finger plots obtained in the dark, the threshold voltage was found to be $V_{th} \simeq 2.6$ mV. Figure 3.21 shows a visualization of the dark counts of the two channels of the SiPM tile on the digital oscilloscope within the time window of 1 ms. Multiplying the counts in the 1 ms time window by 10^3 and normalizing them to the total area in a channel (half-tile, $12 \times 12mm^2$ $\times 8 = 1152mm^2$) we get the frequency of dark counts per unit area. On average, ~ 30 dark events are counted in the 1 ms time window. Thus, the result of the measurement of the dark count rate performed on a single SiPM tile coupled with a Front-End board is: $DCR \sim 25\ Hz/mm^2$.

3.4 Characterization of pre-production FEBs with SiPM tiles

After these preliminary tests, which showed good performance of the FEBs coupled with SiPM tiles, we started a characterization campaign on 100 pre-production FEBs. The aim was to demonstrate that the architecture chosen for the FEBs was suitable to support the high performance of the TAO SiPMs before starting massive production. In particular, we focused on the study of four figures of merit that have been defined in the TAO experiment [44] relative to the SiPMs, which have to meet specific requirements in order to reach the desired resolution of the TAO detector: Signal-to-Noise Ratio > 10, Single Photoelectron Resolution $< 15\%$, Crosstalk rate $< 20\%$ and Dark Count Rate < 100 Hz/mm^2 at $-50\,^\circ$C. Moreover, a Dynamic Range of 250 photoelectrons (p.e.) for each SiPM tile, corresponding to the maximum signal that can be processed linearly without saturation and compatible with the 0–2 V AD9083 input range, is mandatory, and has been checked. During my Ph.D., I worked in collaboration with other researchers from the Roma Tre University JUNO group on the characterization of 100 pre-production Front-End boards coupled with TAO SiPM tiles (Hamamatsu S16088) at a cryogenic temperature of $-50\,^\circ$C, the same temperature used in the TAO central detector. The goal of the characterization was to show that the implemented architecture for the FEB meets the requirements on the four figures of merit relative to the SiPMs.

3.4.1 Experimental setup

The experimental setup employed for testing the performance of the front-end electronics coupled with the SiPM tiles at $-50\,^\circ$C is shown in Figure 3.22. The setup is the following:

- A climate chamber from ACS, model DY200 C, which allows operating at cryogenic temperatures up to $-70\,^\circ$C.
- A very low intensity UV light-pulser from Hamamatsu, model C8898. The photons are emitted with $\lambda = 407$ nm, in the range of typical scintillation photon wavelengths, with a pulse duration of 80 picoseconds. The laser is coupled to an optical fiber, through which the SiPM tiles are illuminated.
- Two power supplies: a high-voltage (HV) generator from Elind, model 180 P5, for the SiPM tiles supply ($\sim$ 100 V at $-50\,^\circ$C), and a low-

voltage (LV) generator from Elind, model 32DP16, for biasing the integrated circuits on the board (±2.2 V).

- 6 FEBs and 6 SiPM tiles tested at one time, 12 overall channels.
- A flange for the cabling of the power supply and of the output signal of the 6 FEBs and SiPMs
- 6 twisted cables of$\sim$ 14 m for carrying the FEB differential output signal and a transformer to recombine the output differential signals.
- A digital oscilloscope from Teledyne-Lecroy, model WavePro804HD, for data acquisition and preliminary analysis.

3.4.2 Experimental technique

Characterization of the FEBs and SiPM tiles response was carried out at $-50\,^{\circ}$C, under low-intensity laser and dark conditions. Indeed, as we have seen before, in order to evaluate the dark count rate and correlated noise (crosstalk), the SiPM tiles must not be illuminated. The evaluation of the signal-to-noise ratio and resolution on the single photoelectron can, in fact, be carried out under both working conditions. In darkness, on the other hand, the signal produced by the SiPMs can be unambiguously attributed to noise phenomena, allowing their magnitude to be evaluated. To obtain the response spectra under both working conditions, as previously discussed, the waveforms produced by the SiPMs corresponding to the production of one or more photoelectrons were sampled in a defined time window using the digital oscilloscope. One of the differences in the experimental technique between the preliminary tests and this pre-production characterization is the choice of the time window in which the maximums are sampled. In fact, to perform a more accurate measurement of the electronic noise, the sampling window has been extended backward by 1 μs. This allows for a narrower distribution of the pedestal, leading to a better signal-to-noise ratio. A picture of the typical acquired waveforms and the histogram related to the voltage maximums is shown in Figure 3.23. The histogram exhibits several peaks. The first peak corresponds to 0 p.e. collected (pedestal), the second one to the collection of 1 p.e., the third one to the collection of 2 p.e., and so on. Performing a gaussian fit on each peak of the multi-photon spectrum, as shown in Figure 3.3, it is possible to obtain the information relative to the figures of merit of the SiPMs. The signal-to-noise ratio is obtained as the difference between the mean values of the first peak (μ_1) and the pedestal (μ_0), divided by the

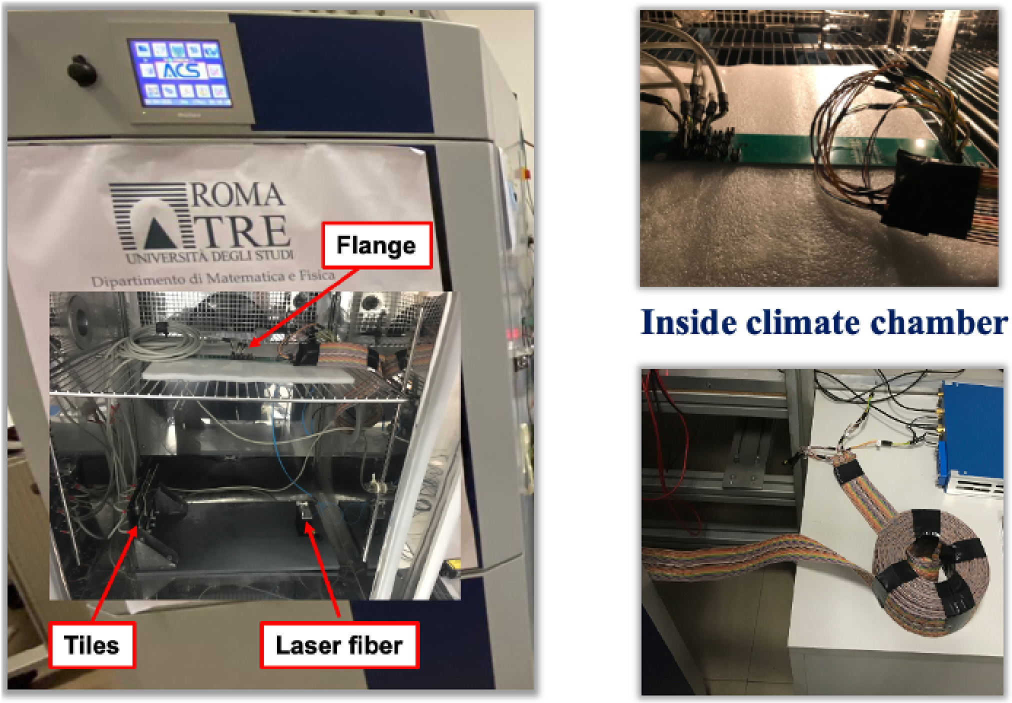

CLIMATE CHAMBER

Outside climate chamber

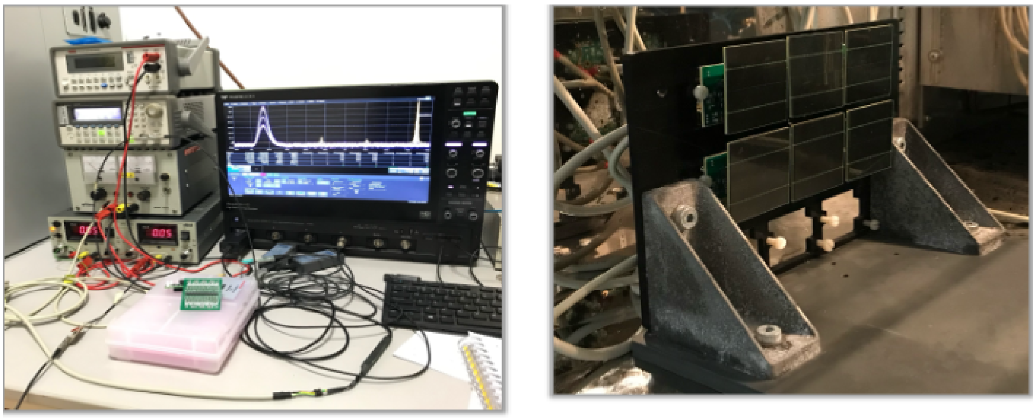

SUPPLY & READOUT

6 FEBs + Tiles

Figure 3.22: *Pictures of the experimental setup used for the characterization of the FEBs coupled with the SiPM tile. In the upper left, the inside of the climate chamber used to operate at* $-50\,^{\circ}$C*. In the upper right, the flange cabling inside the climate chamber; outside the climate chamber the twisted cables and the transformer used to recombine the output differential signals. In the bottom left, the supply and readout system. In the bottom right, a close-up picture of the 6 FEBs and SiPM tiles analized at once.*

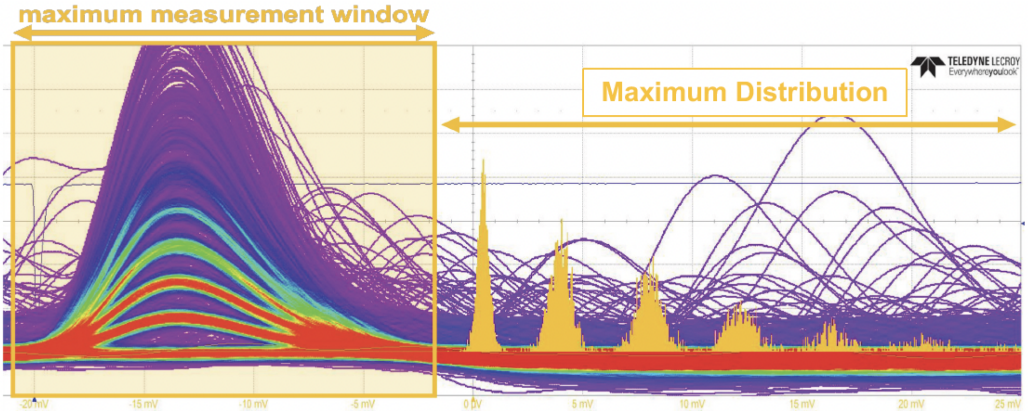

Figure 3.23: *Visualization of the response of a SiPM tile showed on the digital oscilloscope, with the corresponding histogram of the maximums on the right*

standard deviation of the pedestal (σ_0). The single photoelectron resolution, instead, is obtained by the ratio between the standard deviation (σ_1) and the mean value (μ_1) of the first peak, corresponding to the production of 1 p.e. The requirements, then, are the followings:

- Signal-to-noise ratio:

$$SNR = \frac{\mu_1 - \mu_0}{\sigma_0} > 10 \tag{3.20}$$

- Single photoelectron resolution:

$$RES = \frac{\sigma_1}{\mu_1} \times 100 < 15\% \tag{3.21}$$

In dark conditions, the peaks in the finger plots are generated by noise effects. In particular, the production of the first photoelectron is due to thermal noise, which can subsequently produce one or more secondary photoelectrons by activating adjacent cells for the optical crosstalk. Consequently, if we want to measure the frequency of crosstalk noise events, we have to evaluate the ratio between the number of events in the peaks corresponding to two or more photoelectrons detected (N_{2+}) and the number of events in the peak of the first photoelectron (N_1). Then, the condition on the crosstalk frequency is:

- Crosstalk:

$$XTLK = \frac{N_{2+}}{N_1} < 20\% \tag{3.22}$$

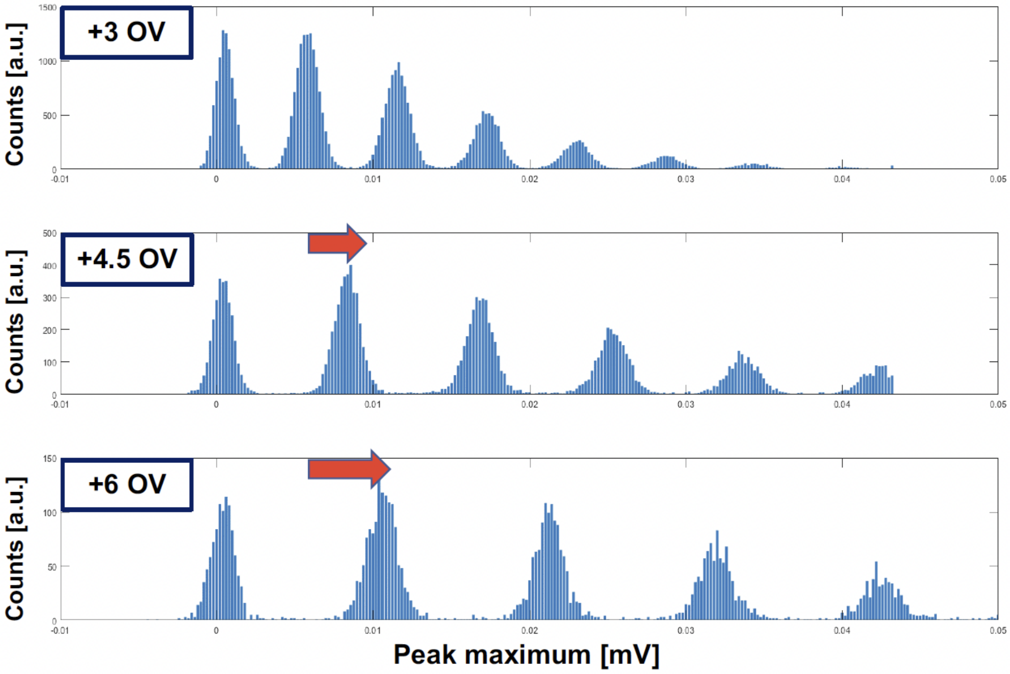

Figure 3.24: *Histograms corresponding to the maximum distribution of the acquired waveforms from the SiPM tile for 3 different over-voltages (+3, +4.5, +6 V)*

The evaluation of the dark count rate, as we have seen, follows a different procedure. In dark conditions, using the digital oscilloscope, events above a certain voltage threshold, identified as halfway between 0 p.e. and 1 p.e., are counted within a 1 ms time window. The number of events ($N_{0.5+}$) is then multiplied by 10^3 and normalized for the size of half-tile, since each channel reads half a tile. This gives the frequency of dark count events expressed in Hz/ mm^2. The requirement on the DCR is:

- Dark count rate:

$$DCR = N_{0.5+} < 100Hz/mm^2 \tag{3.23}$$

Moreover, acting on the bias over the SiPM breakdown voltage $V_{OV} = V_{BIAS} - V_{BR}$, it is possible to change the photoelectric gain and adjust the dynamic range and the values of these figures of merit, as shown in Figure 3.24, where the histograms corresponding to the maximum distribution of the acquired waveforms for 3 different overvoltages (+3 V, +4.5 V, +6 V) are reported. Increasing the operating voltage improves the photon detection efficiency, the single electron resolution and the signal-to-noise ratio, it

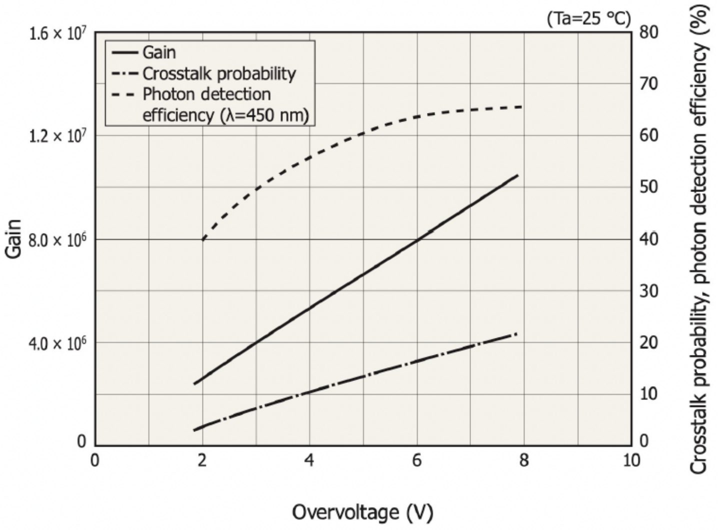

Figure 3.25: *Variation of the Gain, of the Crosstalk probability and of the Photon Detection Efficiency (at* $\lambda = 450$ *nm) as functions of the Overvoltage for the Hamamatsu S16088 TAO SiPM tiles at room temperature.*

also increases the dark count rate and the crosstalk rate at the same time, as shown in Figure 3.25. For this reason, it is not convenient to operate the TAO SiPM tiles with an overvoltage $V_{OV} > 4.5V$.

3.4.3 Result of the characterization

The characterization of the 100 pre-production Front-End Boards was performed with two overvoltages: $V_{OV} = 3V$ and $V_{OV} = 4V$. Figure 3.26 shows, as an example, the characterization made on a channel of the 6 FEBs and SiPM tiles tested at once, for the two different overvoltages, in dark conditions and with the UV laser source. In Fig. 3.27 is shown the dark count rate measurement for the two overvoltage values. Regarding the Dynamic Range, the single p.e. signal is ∼8 mV and ∼10.5 mV for $V_{OV} = 3V$ and $V_{OV} = 4V$, respectively. Therefore, considering the 0–2 V ADC input range, a dynamic range greater than 125 p.e. for single channel, and consequently more than 250 p.e. for the entire SiPM tile, is achieved. The figures of merit are reported only for the nominal operating condition of $V_{OV} = 3V$, which has been selected as the working point for the TAO experiment. In Figure 3.28 the result of the characterization performed on all 100 pre-production FEBs with $V_{OV} = 3V$ is shown. On average, the measurements performed showed the following results for the four figures of merit:

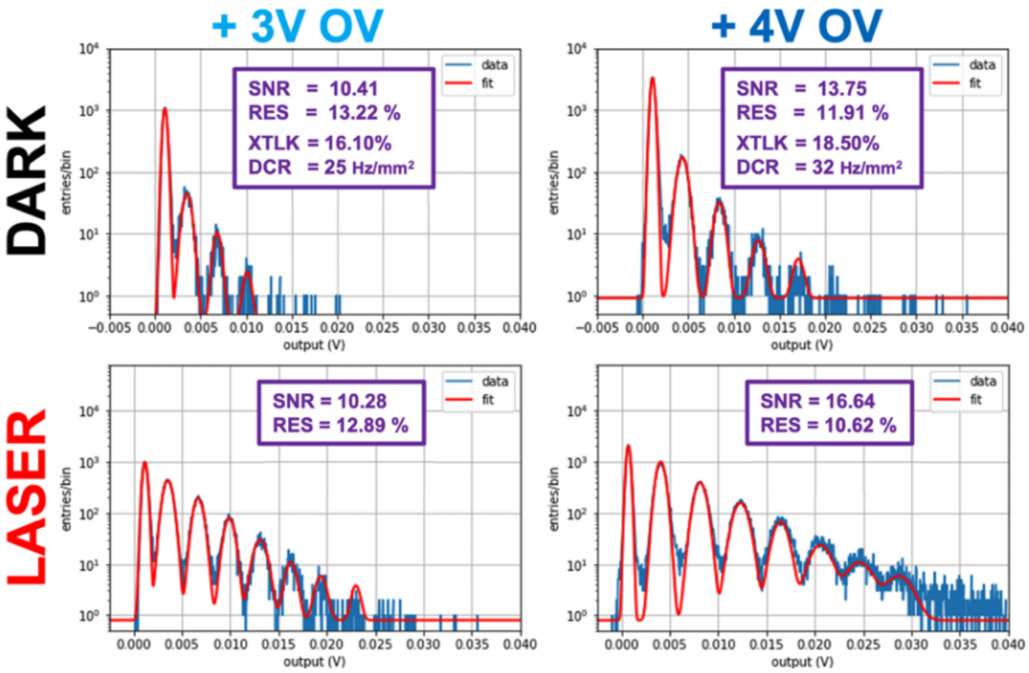

Figure 3.26: *Example of characterization of one channel of the set of 6 Front-End boards coupled with 6 S16088 TAO SiPM tiles tested at once, with* $V_{OV} = 3V$ *and* $V_{OV} = 4V$ *overvoltages, in dark condition and with a very low-intensity UV laser source, at* $-50\,°\mathrm{C}$.

- $\langle \mathrm{SNR} \rangle = 11.86 \pm 1.60$
- $\langle \mathrm{RES} \rangle = (13.98 \pm 1.22)\ \%$
- $\langle \mathrm{XTLK} \rangle = (14.45 \pm 2.57)\ \%$
- $\mathrm{DCR} \simeq 25\ Hz/mm^2$

These results demonstrate how the implemented architecture of the FEBs allows the SiPM performance to meet the TAO requirements for energy resolution.

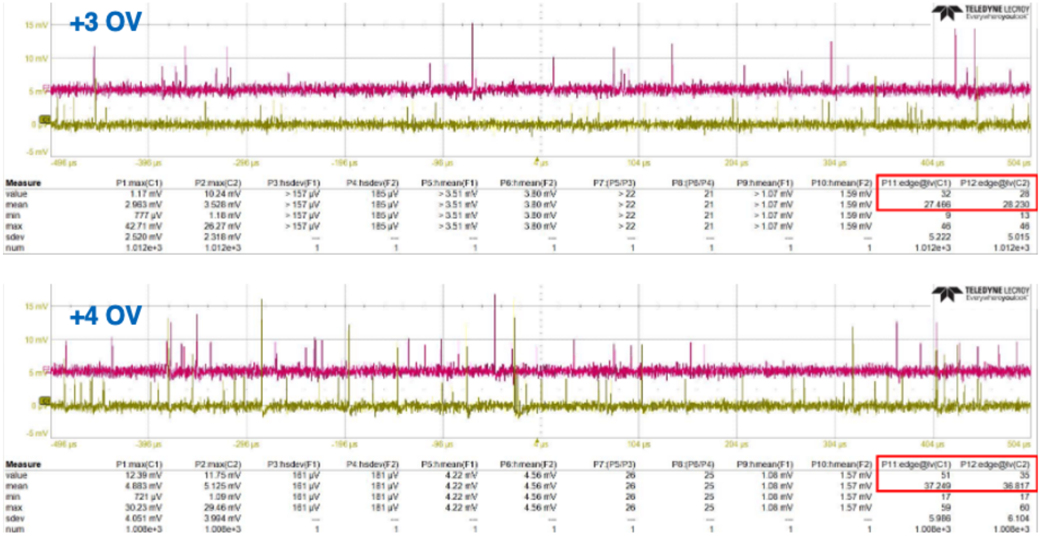

Measure	P1:max(C1)	P2:max(C2)	P3:hsdev(F1)	P4:hsdev(F2)	P5:hmean(F1)	P6:hmean(F2)	P7:(P5/P3)	P8:(P6/P4)	P9:hmean(F1)	P10:hmean(F2)	P11:edge@lv(C1)	P12:edge@lv(C2)
value	1.17 mV	10.24 mV	> 157 µV	185 µV	> 3.51 mV	3.80 mV	> 22	21	> 1.07 mV	1.59 mV	32	28
mean	2.983 mV	3.528 mV	> 157 µV	185 µV	> 3.51 mV	3.80 mV	> 22	21	> 1.07 mV	1.59 mV	27.466	28.230
min	777 µV	1.18 mV	> 157 µV	185 µV	> 3.51 mV	3.80 mV	> 22	21	> 1.07 mV	1.59 mV	9	13
max	42.71 mV	26.27 mV	> 157 µV	185 µV	> 3.51 mV	3.80 mV	> 22	21	> 1.07 mV	1.59 mV	46	46
sdev	2.520 mV	2.318 mV	---	---	---	---	---	---	---	---	5.222	5.015
num	1.012e+3	1.012e+3	1	1	1	1	1	1	1	1	1.012e+3	1.012e+3

Measure	P1:max(C1)	P2:max(C2)	P3:hsdev(F1)	P4:hsdev(F2)	P5:hmean(F1)	P6:hmean(F2)	P7:(P5/P3)	P8:(P6/P4)	P9:hmean(F1)	P10:hmean(F2)	P11:edge@lv(C1)	P12:edge@lv(C2)
value	12.39 mV	11.75 mV	181 µV	181 µV	4.22 mV	4.56 mV	26	25	1.08 mV	1.57 mV	51	35
mean	4.883 mV	5.125 mV	181 µV	181 µV	4.22 mV	4.56 mV	26	25	1.08 mV	1.57 mV	37.249	36.817
min	721 µV	1.09 mV	181 µV	181 µV	4.22 mV	4.56 mV	26	25	1.08 mV	1.57 mV	17	17
max	30.23 mV	29.46 mV	181 µV	181 µV	4.22 mV	4.56 mV	26	25	1.08 mV	1.57 mV	59	60
sdev	4.051 mV	3.994 mV	---	---	---	---	---	---	---	---	5.986	6.104
num	1.008e+3	1.008e+3	1	1	1	1	1	1	1	1	1.008e+3	1.008e+3

Figure 3.27: *Measurement of the dark count rate through the digital oscilloscope, at* $V_{OV} = 3V$ *and* $V_{OV} = 4V$ *overvoltages, at* $-50\,°C$.

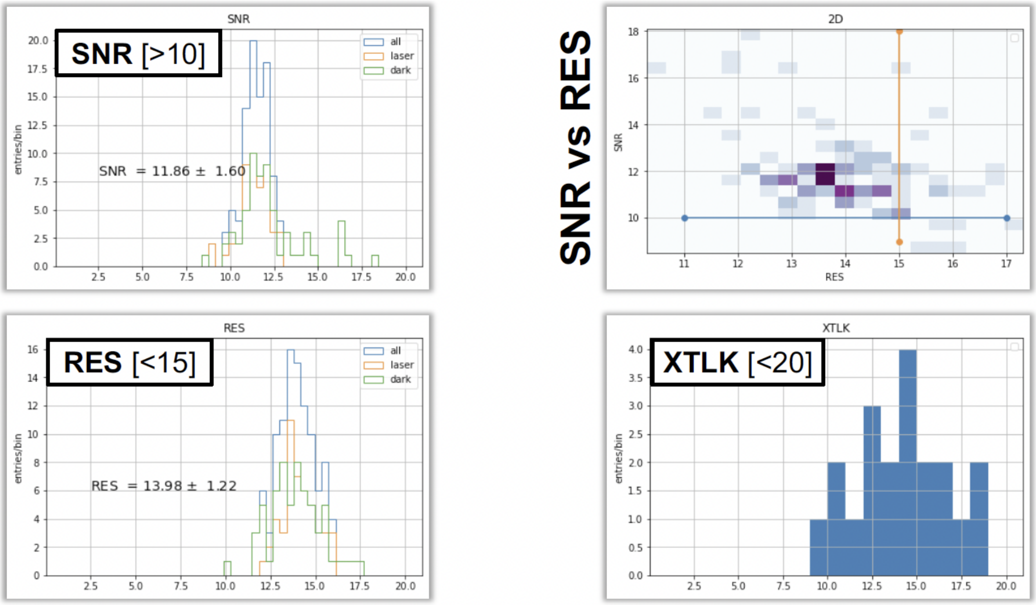

Figure 3.28: *Overall results of the characterization on the 100 pre-production Front-End boards coupled with S16088 TAO SiPM tiles with for* $V_{OV} = 3V$, *in dark condition and with a very low-intensity UV laser source, at* $-50\,°C$.

3.5 FEBs and ADCs post-production tests

After verifying the correct operation with SiPM tiles, mass production of the Front-End boards started. The FEB production was carried out by an external company. Approximately 4,350 boards were produced in total, compared to the 4024 requested. The production of the boards was completed at the end of 2024. In order to verify their correct operation before shipping them to the Taishan site for installation on the TAO detector, a dedicated mass testing campaign was carried out, which will be described in the following section. At the end of the mass testing, all 4024 FEBs have been successfully installed and are currently being used in the commissioning phase of the TAO detector. Regarding analog-to-digital converters, mass production started in May 2025. The production was carried out by the same external company of the FEBs. Approximately 275 ADC boards have been produced, compared to the 258 requested. The majority of the ADCs boards have been successfully tested and shipped to the Taishan site, installed in the TAO detector, and are currently being used in the commissioning phase, with only 16 ADCs still missing, waiting to be tested and shipped. The mass tests performed on the FEBs and ADCs, carried out at the INFN laboratories of Roma Tre University, are briefly described below.

3.5.1 FEBs mass testing

The FEB mass testing followed two steps:

- Test of the FEB to SiPM tile connections
- Test of the response of each FEB channel

For the FEB to SiPM tile connection, each FEB is plugged on a test board. The test board contains LEDs indicating that each connector pin is properly connected. Figure 3.29 shows a picture and a schematization of the test board. Only 3 of the total of 4380 FEBs failed the LED test.

With the response test, all four channels of each FEB are tested to check the linearity of the response. Using a pulse generator, a square signal with different amplitudes of 500 mV, 4V, and 10V is injected with a test board to the input of each channel of the FEBs. The FEB outputs are then analyzed using a digital oscilloscope, producing histograms of the response. A picture of the setup used for the mass testing campaign is shown in Fig. 3.30, the input signal and the expected output signal are depicted in Fig. 3.31. The output signal shown in Fig. 3.31 (right) is expected to have this shape because the FEB is optimized to process fast transient signals rather

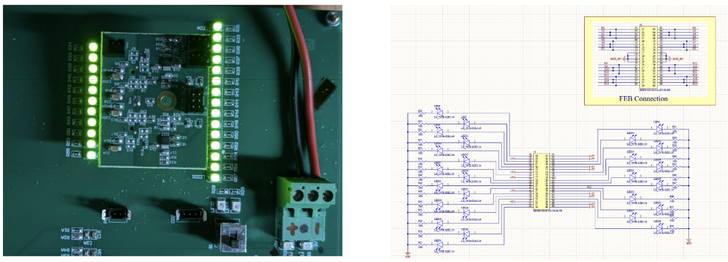

Figure 3.29: *Picture and schematization of the test board used for the FEB-tile connection test.*

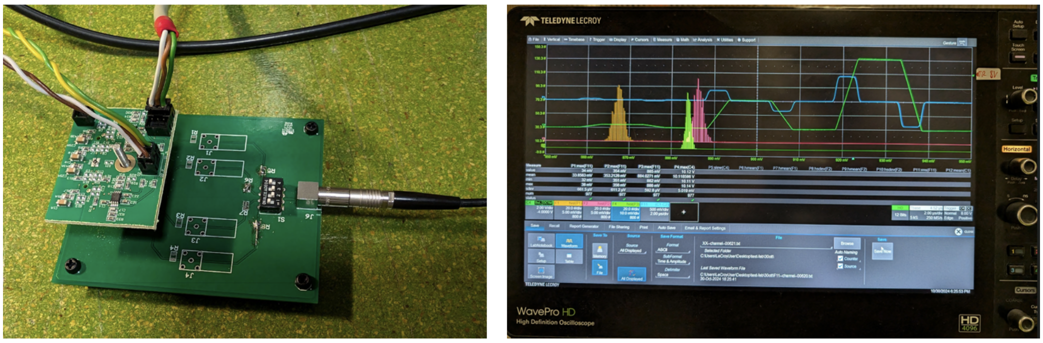

Figure 3.30: *Picture of the setup used for the response test of the FEBs. On the left, a picure of the FEB coupled with the test board. On the right, the input and output signals shown on the digital oscilloscope.*

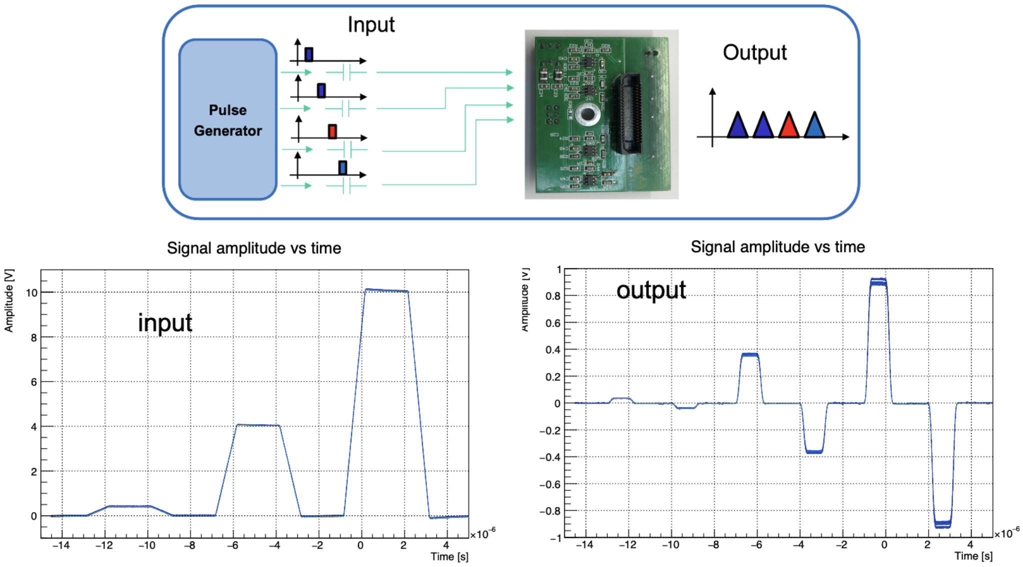

Figure 3.31: *On top, the schematization of the response test. In the bottom part, the input signal sent to each channel and the expected output signal.*

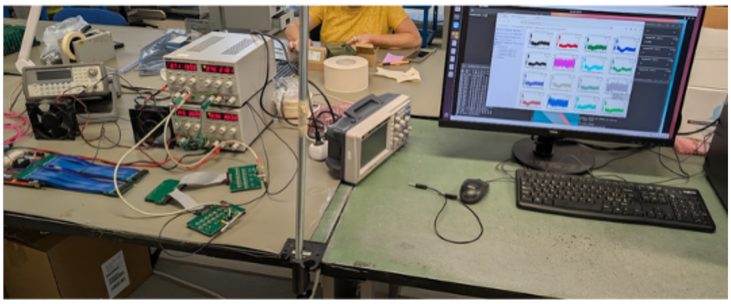

Figure 3.32: *Picture of the setup used for the QA / QC test of the ADCs.*

than quasi-static voltage levels. Therefore, when a square input signal is injected, the front-end responds mainly to the rising and falling edges of the pulse. This produces a shaped bipolar output, with a pulse of one sign at the leading edge and a pulse of opposite sign at the trailing edge. The compliance of each FEB with the design specifications was evaluated using a set of figures of merit derived from the measured output signals. In particular, the main quantities considered were the overall gain, the linearity of the response within the required dynamic range, and the shape and stability of the output signal. These parameters were compared to the expected values from the design in order to verify that each FEB operated within specifications.

During the test, some of the boards showed short circuits or were noisy. Most of them were cured and shipped. Currently, all 4024 Font-End boards are installed at the TAO detector and are being successfully used in the commissioning phase.

3.5.2 ADCs mass testing

Through the use of a test JIG, quality assurance and quality control (QA / QC) tests have been performed on all the produced ADC boards, to evaluate the response of all 32 channels of each board and determine whether the device can be accepted for use or not. Figure 3.32 shows a picture of the experimental setup used for the mass testing. The test JIG generates 32 signals that feed all the ADC board inputs. Each signal consists of a square signal with 5 different amplitudes up to ∼2V. In this way, it is possible to scan the whole input range of the AD9083 (0-2 V). Figure 3.33 shows the schematization of the test and an example of a good channel response to the input signal. The quality of the channel response was assessed based on a set of qualitative criteria derived from the digitized waveforms. In particular, a channel was considered to operate correctly if the output signal exhibited a stable shape without distortions, a consistent amplitude scaling

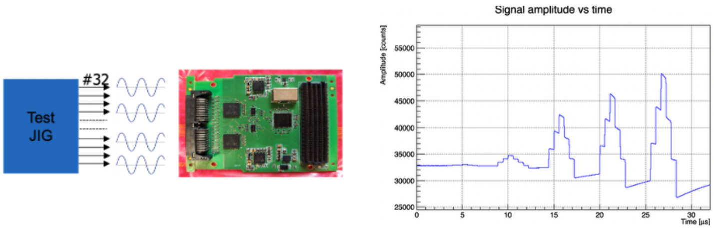

Figure 3.33: *On the left, a schematization of the QA / QC test. On the right, an example of a good channel response to the input signal with different amplitudes.*

with the input signal, and no signs of saturation, clipping or abnormal noise. In addition, the response was required to be uniform across channels under the same input conditions. These criteria were used to identify channels not meeting the expected performance.

At the moment, almost all boards have been tested, shipped, and installed in the TAO detector, and are being used for the commissioning phase. During the QA/QC tests, some of the ADC boards exhibited failures in the readout chain, resulting in the absence or corruption of the digitized signal at the DAQ level. Most of these boards were successfully recovered after further intervention, leaving only 16 ADC boards to be cured, tested, and shipped to the Taishan site. Currently, 242 ADCs are being used successfully in the commissioning phase of the TAO detector, with the last 16 ADC boards expected to be installed in the next weeks.

Chapter 4

Inverse Beta Decay Monte Carlo simulations

Monte Carlo simulations play a central role in the interpretation and analysis of data collected in high energy physics experiments. Their purpose is to reproduce, as realistically as possible, the physical processes underlying signal formation and background generation, as well as the response of the detector to these processes.

In the context of the Taishan Antineutrino Observatory (TAO), Monte Carlo (MC) modeling of inverse beta decay (IBD) reaction is essential for several reasons. First, TAO aims to measure the unoscillated reactor antineutrino spectrum with precision below the 2% at 1 MeV, a goal that requires a detailed understanding of how IBD events deposit energy in the liquid scintillator. Second, Monte Carlo simulations provide quantitative predictions for key observables, such as the prompt and delayed energy spectra and their time distributions, which form the basis of the Inverse Beta Decay selection criteria.

During my PhD, I generated and analyzed MC simulations of IBD events, in order to perform some preliminary analysis, including the evaluation of the IBD selection efficiency. In addition, a preliminary study on the prompt IBD events was carried out, with the purpose of evaluating the energy leakage effects of the detector and estimating the detector response, producing a very preliminary response matrix.

In the first part of this chapter, distributed computing of the JUNO experiment used to perform MC simulations will be described, as well as an overview of the TAO software and the physical generator used for the IBD simulations. Then, the results of the IBD simulations and the efficiency of the selection criteria will be shown. In the last part, the energy leakage effect and the detector response will be described.

4.1 JUNO distributed computing system

Distributed computing is a fundamental tool for large-scale experiments such as JUNO. The extensive amount of data samples required by the JUNO physics program, both for Monte Carlo simulations and for data analysis, makes the use of a distributed computing system essential. The data acquisition system of TAO is designed to handle a high-rate, waveform-based readout of several thousand SiPM channels. At the trigger input level, the data throughput reaches values of the order of 100 Gbps, dominated by SiPM dark counts and background signals. After event selection, the effective event rate is of the order of a few hundred Hz, with a corresponding data throughput of about 500–800 Mbps. The final output data rate is reduced to below 100 Mbps, mainly limited by the network bandwidth between the Taishan site and IHEP. This corresponds to a total data volume of approximately 1 TB per day, or about 300 TB per year. These figures define the computational requirements for data processing, storage and simulation workflows.

To address these computational needs, the JUNO Collaboration has developed and adopted a dedicated Distributed Computing Infrastructure (DCI) [78], designed to efficiently manage large production campaigns and user analysis. Computing and storage resources are geographically distributed across several data centers around the world, including the major facilities at IHEP, IN2P3, INFN-CNAF, JINR, and other partner institutes. The JUNO DCI is designed to integrate grid, cloud, and cluster resources into a coherent system, offering to the users a global identity and a uniform interface for job submission and data access. Authentication and authorization are based on X.509 certificates combined with Virtual Organization Membership Service (VOMS) credentials, which uniquely identify users and associate them with the JUNO Virtual Organization (VO). The JUNO DCI relies on DIRAC (Distributed Infrastructure with Remote Agent Control), which is a general-purpose framework for distributed computing adopted by many large-scale scientific collaborations. JUNO DCI manages and executes jobs through a centralized workload management system (WMS) built on the DIRAC middleware. User jobs, submitted via JUNO-specific interfaces such as JSUB or the Production System, are handled by the DIRAC WMS, which is responsible for scheduling, dispatching, and monitoring workloads across geographically distributed computing sites. DIRAC interfaces with local batch systems at each site and employs a pilot-job mechanism to execute workloads. The WMS for job submission is depicted in Figure 4.1. Data management is provided by DIRAC, which provides a global view of the data through the Dirac File Catalogue (DFC), where files are identified by logical file names, decoupling data access from physical storage locations.

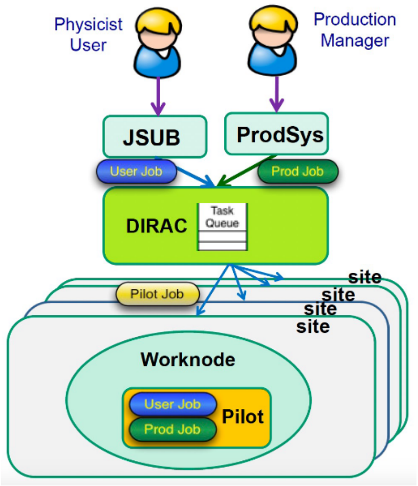

Figure 4.1: *Schematic view of the JUNO DCI workload management model. User and production jobs are submitted through JSUB and ProdSys, respectively, and forwarded to DIRAC, which acts as the Workload Management System (WMS) of the JUNO DCI. DIRAC queues tasks, deploys pilot jobs on distributed sites, and matches available resources to pending workloads.*

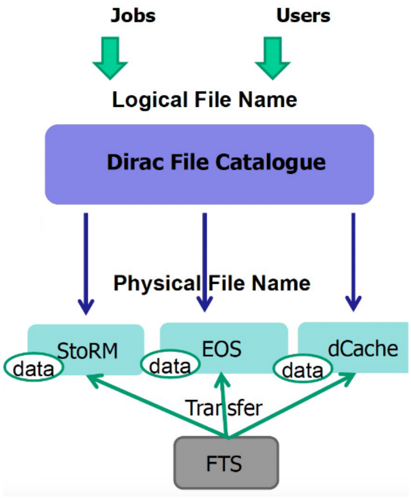

Figure 4.2: *Schematic view of data management in the JUNO DCI. Jobs and users access data through logical file names registered in the Dirac Fila Catalogue, which maps them to physical file names stored on distributed storage elements such as StoRM, EOS, and dCache. Data replication and transfers between storage elements are coordinated by the FTS, while DIRAC provides a unified and location-independent interface to distributed datasets.*

Data transfers and replication between storage elements are coordinated by DIRAC-integrated services, such as the File Transfer System (FTS), ensuring efficient and reliable movement of data across the distributed infrastructure and allowing simulation and analysis outputs to be shared and reused within the JUNO collaboration. Figure 4.2 shows a schematization of the data management system in JUNO DCI.

During my PhD, I worked on the job submission scripts of the JUNO DCI, adapting them to the specific requirements of the TAO simulation software. After implementing these modifications, I delivered a tutorial to the TAO collaborators to illustrate the updated workflow. I also exploited the DCI to carry out Monte Carlo simulations for my research.

4.2 TAO simulation software

The TAO offline software (TAOsw), developed in C++ and Python, is based on the Software for Non-collider Physics Experiments (SNiPER) framework [79], and is built on the existing JUNO software [80]. It handles software units (Geant4, ROOT, I/O), job profiles, and events and offers extensible data schemes and concurrent processing capabilities. In the context of the TAOsw and the JUNO DCI, a job represents a single unit of work submitted to the computing system, typically corresponding to the simulation or processing of a given number of events. The term "event" refers to individual physical interactions (e.g. inverse beta decay or background processes) generated and processed within the simulation chain. A "job profile" defines the configuration of a job, including the type of events to be simulated, the number of events per job, and the associated software and detector conditions. The core utilities such as Geant4 [81] and ROOT [82] are used for simulation and data analysis, respectively. It handles software units, job profiles, and events and offers extensible data schemes and concurrent processing capabilities.

The existing framework of the JUNO software provides a significant advantage in constructing TAO offline software: since both are liquid scintillator detectors, the existing JUNO modules can be adapted and customized to meet the dimensions of TAO and other needs. The complete layout of the TAO offline software with the above details is shown in Figure 4.3 and contains some modules of the JUNO offline software, specific modules of the TAO offline software, the SNiPER framework, and some external libraries like Geant4 and ROOT. The modules in the JUNO software include as follows:

- Generators like GENIE [83], which handles the neutrino interaction with the target matter and simulates the corresponding secondary particles.
- Geant4, a simulation toolkit for modeling detector geometry, physics processes like electromagnetic process, decay physics, hadronic, optical and special processes tailored for accurate neutrino interaction and background event modeling and photon propagation. Also, Geant4 handles the propagation and interaction of the neutrino secondaries, as well as the emission, propagation and detection of optical photons. The optical response of the detector is simulated using the Geant4 optical model, where scintillation photons are generated and tracked through the detector volume, taking into account absorption, re-emission, scattering processes and interactions with detector materials and surfaces, up to their detection by the SiPM photosensors.
- The Calibration package handles the energy scale calibration and detector response corrections by applying calibration constants to the simulated or real data. These constants are typically derived from dedicated calibration measurements, performed using radioactive sources deployed through systems such as the ACU and CLS. In the context of this work, where the detector calibration was not yet available, the calibration constants were obtained from simulation studies and reference values from the literature. The calibrated data are then used as input for the subsequent reconstruction algorithms.
- The reconstruction package processes the data to reconstruct energy, vertex, waveform, charge distribution, particle tracks and directional information.
- The analysis package handles the event selection and statistical analysis of the data to identify IBD candidate and assess the reactor antineutrino spectrum.

The JUNO Offline Software is developed for a wide variety of non-collider physics analysis problems, supporting complex analysis in solar and atmospheric neutrinos, while utilizing general reconstruction algorithms and flexible data processing workflows. TAO, instead, is explicitly focused on reactor antineutrino detection and, as such, employs specialized reconstruction algorithms, dedicated calibration methods specific to liquid scintillator response, and statistical analysis tools aimed at precision measurements of the unoscillated antineutrino spectrum. The TAO software uses the same modules as JUNO with the following key adaptations:

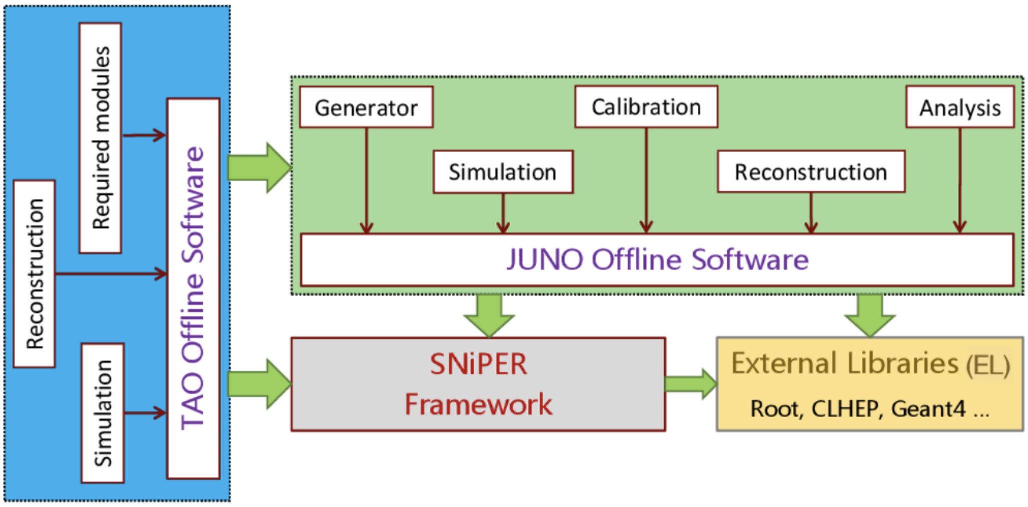

Figure 4.3: *Components of the TAO offline software. The JUNO Offline Software is a data processing environment with components of physics generators, detector simulation, calibration, reconstruction and analysis. The TAO Offline Software, that has been tailored specifically for reactor antineutrino detection, has a structure similar to JUNO Offline Software but focusing on the specific requirements of the TAO experiment. The SNiPER Framework serves as the mainstay for the software of both JUNO and TAO providing an extensible architecture for efficient event data management and the External Libraries that consist of mainly Geant4 for simulating interactions of particles and ROOT for data handling and visualization.*

- **Detector geometry:** JUNO is a large-scale detector with a spherical central volume of about 35 m in diameter, surrounded by tens of thousands of PMTs and an external water Cherenkov veto. Its simulation must handle long optical paths, large photon statistics, and complex boundary conditions over macroscopic distances. TAO is a compact, ton-scale detector with a central volume of about 1.8 m in diameter. The simulation of the detector focuses on a detailed local geometry at the level of individual detector components relevant for optical photon propagation, including mechanical supports, thermal insulation layers, and a very dense SiPM coverage.

- **Photosensors:** JUNO uses large-area PMTs, whose response is modeled in terms of quantum efficiency, angular acceptance, transit-time spread, and dark noise typical of PMTs. TAO employs SiPMs with very high photon detection efficiency and near-total optical coverage. The simulation includes SiPM-specific effects such as dark count rate, optical cross-talk, afterpulsing, saturation, and detailed charge and time response.

- **Scintillator composition:** JUNO uses a liquid scintillator based on linear alkylbenzene without gadolinium loading, where neutron capture in inverse beta decay occurs predominantly on hydrogen with a capture time of $\sim 200\ \mu s$. TAO uses gadolinium-loaded liquid scintillator, leading to a much shorter neutron capture time of $\sim 30\ \mu s$ and a higher energy gamma cascade. The simulation explicitly models neutron capture on gadolinium and its impact on timing and energy deposition. The optical parameters of Gd-LS such as the absorption and re-emission probability are taken from Daya Bay software [84] since TAO and Daya Bay use similar Gd-LS, and these optical parameters remain unchanged at $-50\,^{\circ}\mathrm{C}$ compared to those at room temperature [85].

The simulation module in the TAO offline software consists of three essential components: the physics generator, the detector simulation (DetSim), and the electronics simulation (ElecSim). After simulation, the Calibration and Reconstruction packages complete the chain, providing simulated data to the Analysis package.

The physics generators represent the first stage of the TAO simulation chain. Their role is to generate a truth-level description of the physical processes of interest, with particular emphasis on reactor antineutrino interactions, but also on background events like atmospheric neutrinos, natural radioactivity, cosmic muons, and their induced backgrounds. Generators define the interaction channel, produce the primary particles involved in the event, and assign their kinematic properties, such as energy, position, time, and direction, according to models and interaction cross sections. At this stage, no detector geometry or response is considered, and the generator output provides the reference Monte Carlo truth for subsequent validation and systematic studies.

The Detector Simulation (DetSim) models the interaction of the generated particles with the TAO detector materials. Based on a detailed Geant4 description of the compact TAO geometry, DetSim simulates energy depositions in the gadolinium-loaded liquid scintillator, scintillation light production, and optical photon transport to the SiPMs. Given the small detector size and near-complete photosensor coverage, the DetSim stage for TAO places a strong emphasis on precise optical modeling and uniformity of light collection. The output of DetSim represents the idealized detector response to a physical event, including material and optical effects, but excluding any readout or electronics distortions.

The Electronics Simulation (ElecSim) extends the simulation by modeling the response of the TAO photosensors and front-end electronics. Starting from the detector-level information produced by DetSim, ElecSim simulates the conversion of optical photons into electrical signals in the SiPMs and their subsequent processing by the front-end electronics. The SiPM response is modeled by including the main stochastic effects—dark noise, optical crosstalk and afterpulsing—applied at the level of pulse generation. Dark noise is generated independently for each channel as a Poissonian process in time, with amplitudes smeared according to the gain and its fluctuations. Crosstalk is implemented as a discrete stochastic process that can produce additional avalanches associated with a primary pulse, including both internal contributions within the same channel and external contributions in neighboring channels, with timing determined by optical propagation between sensors. Afterpulsing is modeled as a probabilistic process per pulse, with a time delay sampled from a two-component exponential distribution accounting for fast and slow trapping mechanisms, and with an amplitude modulated by the microcell recovery. The front-end electronics response is simulated by constructing the waveform using a single-photoelectron pulse shape modeled as the difference of two exponential functions, to which Gaussian electronic noise is added. In the present implementation, the waveform is sampled with a clock cycle of 4 ns, corresponding to a sampling frequency of 250 MHz. The analog signal is then digitized through an ADC model, and the resulting waveform is processed to extract timing and charge information at the channel level. In this simulation chain, the role of the Trigger and

Data Acquisition (TDAQ) system is effectively incorporated within the electronics simulation stage: the digitization of the waveform, together with the extraction of timing and charge information and the application of selection thresholds, reproduces the main features of the TDAQ response. The TAO ElecSim stage is particularly detailed due to the use of waveform-level readout and operation at $-50,^\circ$ C, which strongly affects sensor and electronics behavior. The output of ElecSim consists of digitized channel-level signals, including waveform-derived timing and charge information, which are used as input for the subsequent calibration and reconstruction stages.

The Calibration represents the first stage of the TAO offline data processing chain that is common to both simulation and real data. It operates on electronics-level information produced by ElecSim or acquired from the detector and applies calibration constants to correct for hardware-dependent effects such as pedestal offsets, channel-to-channel gain variations, timing misalignments, and non-linear response. In TAO, calibration is a critical step in achieving the stringent control of the energy scale and uniformity required for sub-percent-level spectral measurements. The calibrated output provides a standardized representation of the detector response.

Reconstruction is the final stage of the TAO offline processing chain and operates on calibrated detector information to extract physics observables. Using the calibrated charge and timing information from the SiPM channels, reconstruction algorithms estimate quantities such as the event visible energy and interaction vertex. In TAO, vertex reconstruction plays a crucial role, in particular for the definition of the fiducial volume and for the correction of spatial non-uniformities in the detector response. Current reconstruction approaches combine both traditional and machine-learning-based methods. A widely used technique is the charge center algorithm (CCA), which estimates the event position as the charge-weighted centroid of the SiPM signals. In addition, more advanced approaches based on deep learning have been developed, exploiting convolutional neural networks to learn the mapping between detector observables and the true event position. These methods have been extensively studied in recent works for the TAO experiment, showing that vertex reconstruction resolutions of the order of $\mathcal{O}(1\text{–}2), \mathrm{cm}$ can be achieved. In particular, resolutions better than about 20 mm for CCA and down to $\sim$ 12 mm for deep-learning-based algorithms at 1 MeV have been reported, with biases at the millimeter level [86].

In this work, the first part of the analysis relies only on detector-level (DetSim) information, while in the second part electronics simulation and calibration effects are also taken into account. Reconstructed variables, however, are not directly used in the analyses presented in this thesis, as the focus is on detector response studies and on the construction of the response matrix. Nevertheless, reconstruction remains essential for defining fiducial volume selections and for enabling realistic physics analyses. Monte Carlo simulations presented and analyzed in the following sections have been generated using the TAOsw within the JUNO distributed computing infrastructure, acting remotely from a JUNO user-interface at the CNAF (Centro Nazionale Analisi Fotogrammi) computing center.

4.3 IBD MC simulations

Monte Carlo simulations of Inverse Beta Decay (IBD) events play a central role for TAO in the study of the detector response and in the validation of analysis techniques. In this work, the Monte Carlo simulation focuses on IBD events, which represent the signal of interest for the experiment. Background contributions, such as cosmogenic events and natural radioactivity, are not explicitly simulated, since the analysis is primarily aimed at characterizing the detector response and studying energy-related effects using signal events. Background modeling becomes essential in a complete physics analysis, where event selection and sensitivity studies are performed, but it is beyond the scope of this work. IBD event samples were generated using the physics generator “IBD.exe” provided within the JUNO software framework. The generator makes use of the antineutrino flux model and the IBD cross section discussed in section 1.2.1 to simulate the production and the interactions of the reactor electron antineutrinos in the TAO central detector. Thus, for each antineutrino interaction, a positron and a neutron are generated as primary particles, with the kinematics discussed in section 1.2.3. Then, the DetSim module simulates the interactions of the positron and the neutron in the gadolinium-doped scintillator. The positron is produced with a kinetic energy T_{e^+} closely related to the incoming antineutrino energy. As it propagates through the liquid scintillator, it rapidly loses energy via ionization and excitation of the scintillator molecules, producing scintillation light, then annihilates with an electron, emitting two 0.511 MeV photons. This constitutes the prompt signal. The deposited energy by the positron is then given by $E_{dep} = T_{e^+} + 2 \times 0.511$ MeV $= E_{e^+} + m_{e^+}$. The neutron first undergoes elastic scattering with the nuclei of the scintillator, primarily hydrogen, losing energy and progressively thermalizing over a timescale of a few microseconds. Once thermalized, the neutron is captured by the nuclei present in the scintillator. In TAO, the liquid scintillator is loaded with 0.1% of gadolinium, which provides a large neutron capture cross section. Neutron capture predominantly occurs on gadolinium, releasing a cascade of gamma rays with a total energy of about 8 MeV, which forms the delayed signal. A smaller fraction of neutrons is captured on hydrogen, producing a single 2.2 MeV gamma ray. As we have seen, the kinetic energy of the neutron is of the order of KeV; consequently, it is negligible in terms of the contribution to the initial antineutrino energy, which can be expressed as a function of the deposited energy by the positron: $E_{\bar{\nu}_e} \simeq E_{dep} + 0.782$ MeV. Therefore, in order to reconstruct the antineutrino energy spectrum, the prompt energy deposition by the positron is the key quantity to take into account. The deposited energy by the neutron, instead, is fundamental for the signature of the IBD events. In fact, the neutron capture by gadolinium is the key factor of the IBD selection criteria, as we will see in the next section. To highlight these main two features, a sample of 50.000 IBD events has been generated randomly inside the TAO Gd-LS volume. Figure 4.4 shows the deposited energy by the positron and by the neutron. The shape of the energy deposited by the positron is the classical bell shape of the IBD with a maximum around $\sim$ 3 MeV. The energy deposited by the neutron, instead, highlights the neutron capture on hydrogen (2.2 MeV peak) and the capture on the two gadolinium isotopes (7.94 MeV for ^{157}Gd and 8.54 MeV for ^{155}Gd). Although neutron capture on gadolinium is dominant in terms of event fraction, this is not directly reflected by the relative peak heights in the deposited-energy spectrum. The reason is that neutron capture on hydrogen produces a single 2.2 MeV gamma ray, leading to a relatively narrow feature, whereas capture on gadolinium releases a cascade of gamma rays with total energy around 8 MeV. In a compact detector such as TAO, this energy can be distributed over multiple secondaries and may be only partially contained in the active volume, resulting in a broader deposited-energy distribution. For this reason, the hydrogen peak can appear relatively pronounced even though hydrogen capture is sub-leading with respect to gadolinium capture. Figure 4.5, instead, shows the hit time distributions of the photons produced by the energy depositions of the positrons and the neutrons on the Silicon Photomultipliers. The first, deposits all its energy inside a $\sim 3\mu s$ time window, but the majority of the photons reach the SiPMs with an average time of $\sim 20ns$ (prompt signal). For the neutron, thermalization and capture are processes with a longer average lifetime. The hit time distribution of the photons produced by the neutron capture by the hydrogen and by the gadolinium is a long process, but the majority of the photons reach the SiPMs with an average time of $\sim 30\mu s$.

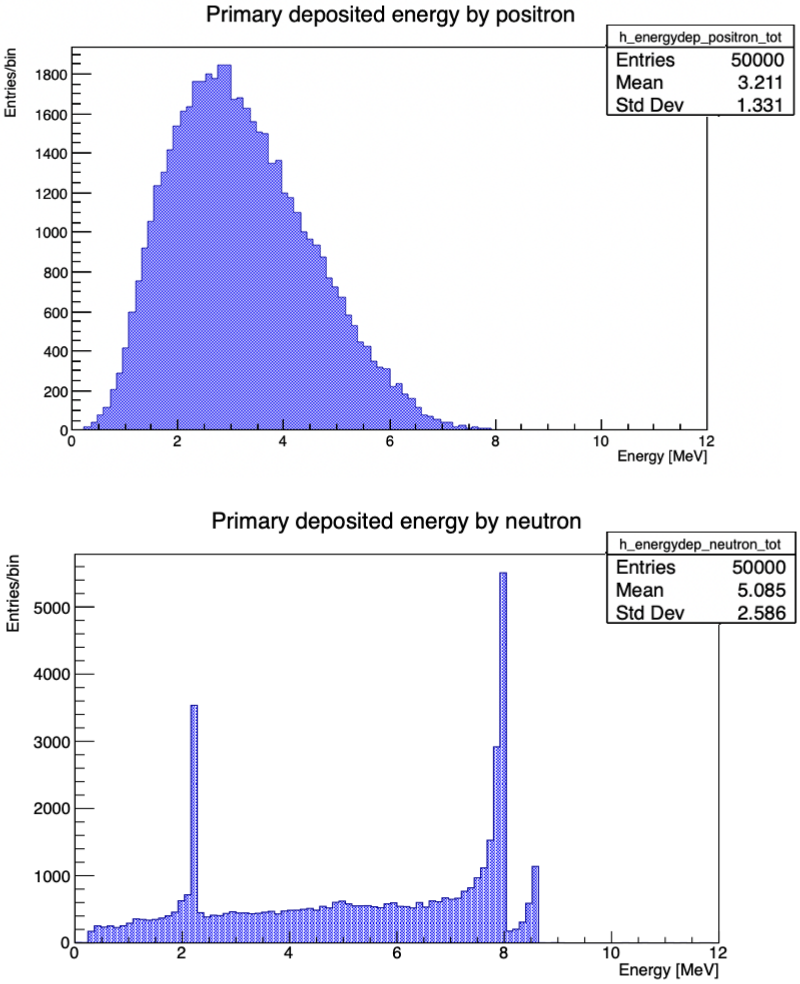

Figure 4.4: *On top, the deposited energy by the positron inside the Gd-LS volume, with the classical IBD bell shape. At bottom, the deposited energy by the neutron, with the peaks of the capture by the hydrogen at 2.2 MeV and by the two gadolinium isotopes at 7.94 MeV for* $^{157}\mathrm{Gd}$ *and at 8.54 MeV for* $^{155}\mathrm{Gd}$

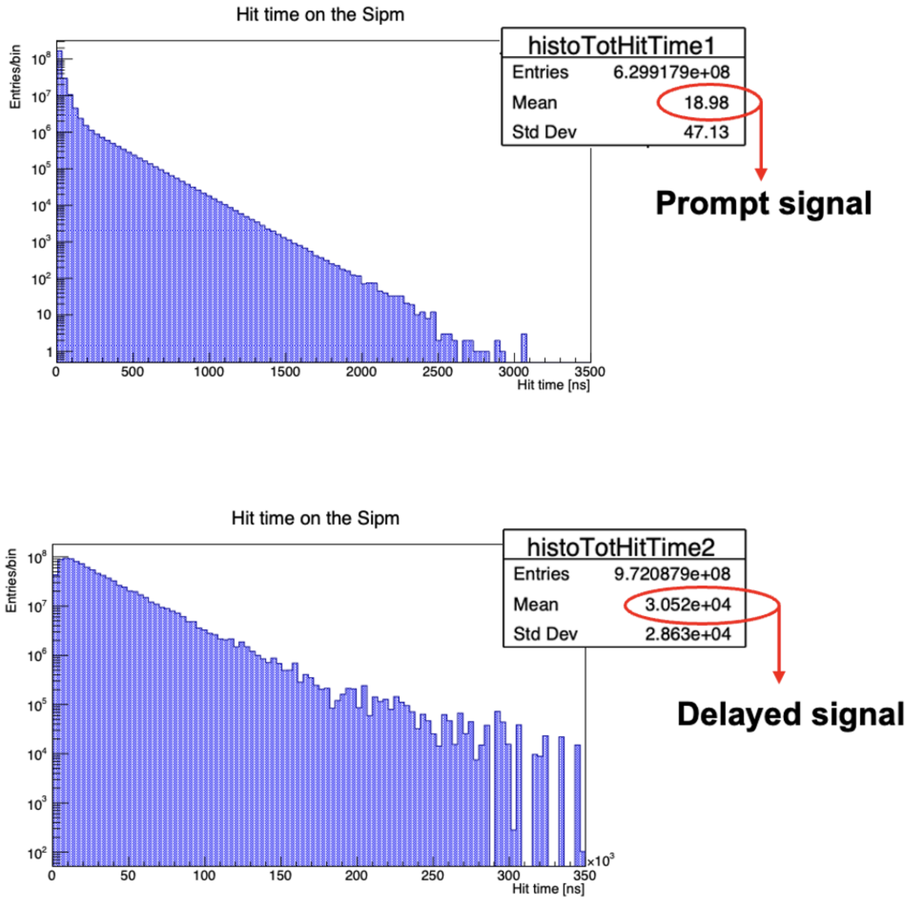

Figure 4.5: *On top, the hit time distribution on the SiPMs of the photons produced by the positron energy deposition, with an average time of* $\sim 20ns$. *At bottom, the distribution of the hits on the SiPMs of the photons emitted during the neutron capture, with and average time of* $\sim 30\mu s$.

4.3.1 IBD selection

The presence of gadolinium in the scintillator mixture, as discussed above, provides a very clear signature for inverse beta decay events in TAO, and is a key factor for the high efficiency of the selection cuts. A useful practice is to evaluate the efficiency of the signal selection cuts on a pure signal Monte Carlo sample, in our case a pure IBD MC sample. The first cut that has to be applied is the Fiducial Volume (FV) cut, $R < 650$ cm, which is not exclusive of the IBD selection and will be applied for the data taking phase of the TAO experiment. In fact, in addition to fully contain the energy deposition of the gammas from the positron annihilation, the FV cut contributes to reduce the background-to-signal ratio from 10% to 2%. The IBD selection cuts and the corresponding efficiencies are as follows:

- **Prompt signal energy cut efficiency** ε_{e+}**:** select prompt signals in [0.9-9] MeV range.
- **Delayed signal energy cut efficiency** ε_n**:** select delayed signals in [7-9] MeV range.
- **Time interval efficiency** ε_t**:** select events with a hit time difference in $1 < \Delta T < 100 \mu s$.
- **Gadolinium capture efficiency** ε_{Gd}**:** how often the neutron is captured by gadolinium.

To evaluate the selection efficiencies, a sample of 50,000 IBD events was generated in the Gd-LS volume. As the IBD selection is performed after the fiducial volume (FV) cut, the corresponding effective sample consists of about 20,000 events. This sample size is sufficient for the validation of the event topology and the selection criteria, as the main features of the signal can be captured with limited statistics. Studies requiring a more precise characterization of the detector response instead rely on significantly larger Monte Carlo samples to reduce statistical fluctuations.

The results and techniques are described below. The statistical uncertainty associated with the efficiency measurements is evaluated by assuming binomial statistics, since each event either satisfies or does not satisfy the applied selection criteria.

- **Prompt signal energy cut efficiency** ε_{e^+}**:** in a pure IBD sample, the prompt signal in the fiducial volume is almost entirely in [0.9-9] MeV range. $\varepsilon_{e+} = 99.95 \pm 0.02\%$

Selection cut	Efficiency (%)
Prompt energy (ε_{e^+})	99.95 ± 0.02
Delayed energy (ε_n)	52.35 ± 0.35
Time interval (ε_t)	96.62 ± 0.12
Gadolinium capture (ε_{Gd})	82.27 ± 0.27
Total ($\varepsilon_{\mathrm{IBD}}$)	41.6 ± 0.3

Table 4.1: Summary of the IBD selection efficiencies and total efficiency.

- **Delayed signal energy cut efficiency ε_n:** the efficiency of selecting delayed events with energy in the [7-9] MeV range is:

$$\varepsilon_n = \frac{N[7-9]}{N_{tot}} = (52.35 \pm 0.35)\% \tag{4.1}$$

- **Time interval efficiency ε_t:** the efficiency of selecting the events with a hit time difference in $1 < \Delta T < 100 \mu s$ is $\varepsilon_t = (96.62 \pm 0.12)\%$

- **Gadolinium capture efficiency ε_{Gd}:** the efficiency of gadolinium capture is obtained from the fraction between events in which capture occurs on gadolinium (N_{Gd}) and events in which capture occurs on hydrogen (N_H) or on gadolinium.

$$\varepsilon_{Gd} = \frac{N_{Gd}}{N_{Gd} + N_H} = (82.27 \pm 0.27)\% \tag{4.2}$$

Figure 4.6 shows the deposited energy by the neutron in the fiducial volume, from which it was evaluated ε_n and ε_{Gd}, and the hit time difference between the photons produced by the energy deposition of the neutron and the positron, through which the efficiency of the hit time difference was calculated. Then, the overall selection efficiency of IBD events is:

$$\varepsilon_{IBD} = \varepsilon_{e^+} \cdot \varepsilon_n \cdot \varepsilon_t \cdot \varepsilon_{Gd} = (41.6 \pm 0.3)\% \tag{4.3}$$

A summary of the efficiencies of the individual selection criteria and of the overall IBD selection efficiency is reported in Table 4.1.

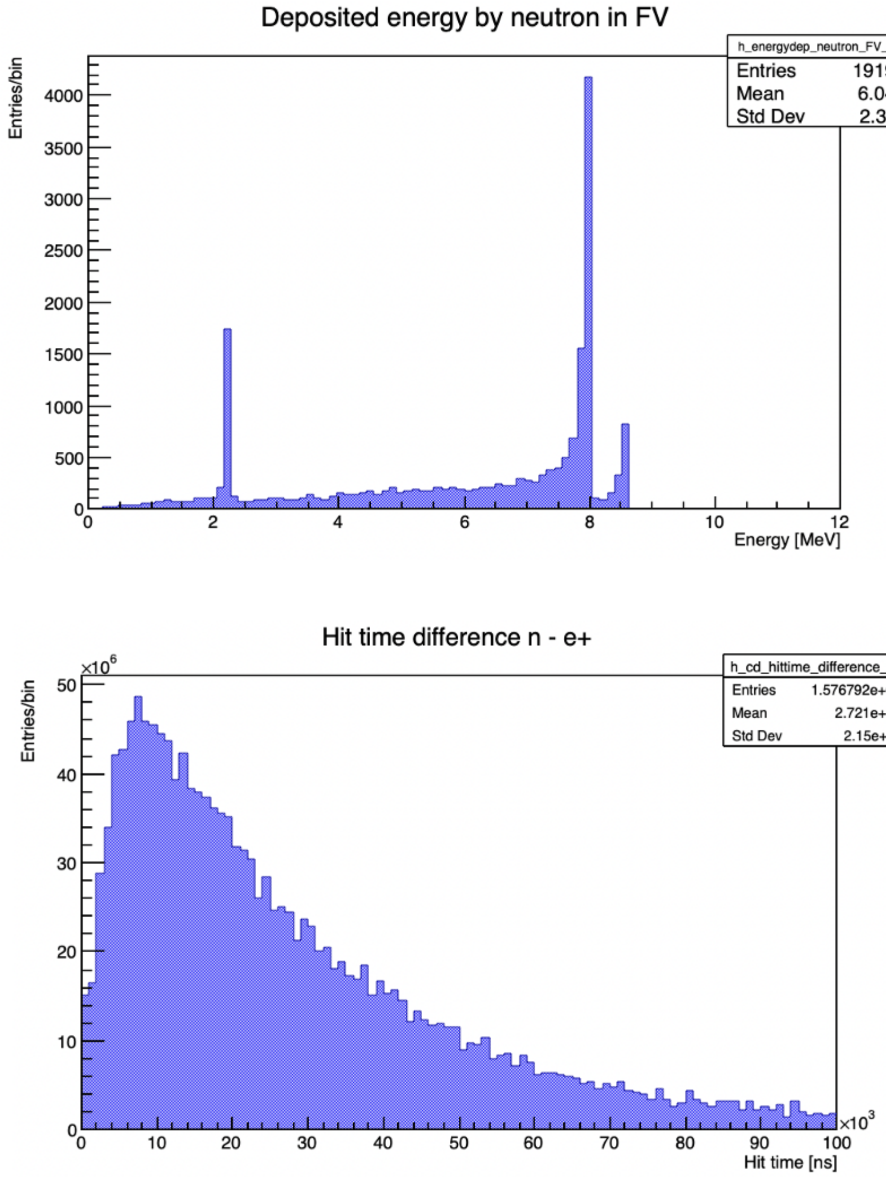

Figure 4.6: *On top, the energy deposited by the neutron in the fiducial volume. At bottom, the distribution of the hit time difference on the SiPMs between the delayed and prompt photons.*

4.4 Prompt IBD Monte Carlo simulations

As we have seen, the signature of inverse beta decay events is very clean and difficult to emulate by background events in TAO. Furthermore, given the clear temporal separation between the energy deposits of the positron and the neutron, it is useful to study the detector's response to positron-only IBD events. This is important because the positron carries most of the visible energy of the interaction and therefore determines the reconstructed energy of the event. Studying positron-only events allows a direct characterization of the detector response, including energy resolution and energy leakage effects, without the additional smearing introduced by the neutron capture process.

For this reason, the physics generator "IBD.exe" of JUNO was used, "switching off" the neutron, to generate positron events with IBD spectrum (i.e. IBD prompt). Using the JUNO DCI, I generated 4 million IBD prompt events randomly distributed inside the Gd-LS volume. Two preliminary studies have been carried out, the first one to evaluate the energy leakage effects of the detector, the second one to study the response of the detector to IBD prompt events through the use of the full simulation chain (DetSim, ElecSim and Calibration).

4.4.1 TAO energy leakage effects

In liquid scintillator detectors such as TAO, the visible energy of positron events does not necessarily coincide with the total initial energy released by the interaction. As shown by the event-by-event correlation between deposited (E_{dep}) and initial (E_{in}) positron energy in Figure 4.7, this discrepancy arises from the combined effects of energy leakage and light collection inefficiencies, which become particularly relevant in compact detector geometries. Energy leakage occurs when a fraction of the electromagnetic energy escapes the active scintillator volume, for instance, through the partial escape of gamma rays produced in positron annihilation, especially for events generated close to the detector boundaries. In addition, even when energy is fully deposited, not all scintillation photons are detected: a fraction of the optical light can be lost due to non-photosensitive regions, absorption, or reflections within the detector. Despite the high photocoverage of TAO ($\sim 95\%$), these optical effects contribute to the observed spread in the distributions of E_{dep} versus E_{in}. The comparison between the correlations obtained with and without a fiducial volume selection clearly demonstrates that the application of the fiducial volume cut significantly reduce the energy leakage effects. This results in a narrower and more linear correlation between deposited and initial energy of the positrons, qualitatively confirming the crucial role of the

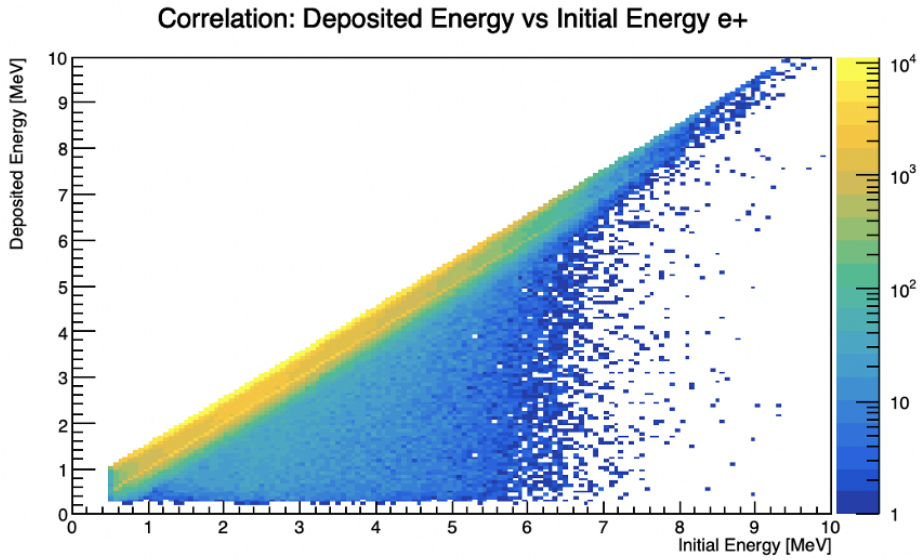

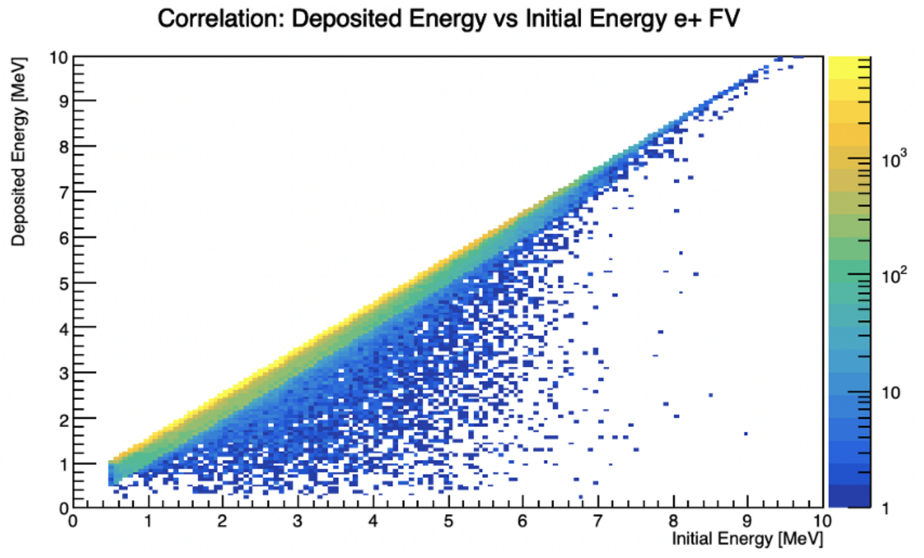

Figure 4.7: *Event-by-event correlation between the energy deposited by the positron and the true initial energy of the positron. On top, in the whole volume. At bottom, in the fiducial volume.*

fiducial volume in mitigating the energy leakage effects in the TAO detector. The energy leakage affects both the shape and normalization of reconstructed energy spectra and must be carefully modeled with Monte Carlo simulations. Figure 4.7 shows the comparison of the distribution of E_{dep} versus E_{in} in the whole volume and in the fiducial volume.

4.4.2 TAO detector response

The detector response of the TAO detector can be characterized through a response matrix that connects the energy deposited by positrons to the experimentally observable signal. In this work, the response matrix is constructed starting from an event-by-event correlation between the energy deposited by positrons in the liquid scintillator and the number of photoelectrons detected by the Silicon Photomultipliers. This correlation provides a direct mapping between the physical energy deposition and the detector-level observable, encapsulating the combined effects of scintillation light production, optical transport, photon detection, and front-end electronics response. The detector response can therefore be interpreted as a two-step mapping: from the true positron energy to the deposited energy, affected by energy leakage, and from the deposited energy to the detected photoelectrons, driven by the detector and electronics response.

Using a large Monte Carlo sample, the response matrix enables a detailed description of energy smearing and bin-to-bin migration effects inherent to the detector, and provides the basis for energy reconstruction through unfolding techniques. To construct the response matrix, we start from the energy deposited by the positron obtained from DetSim. The electronics response is then simulated with ElecSim to reproduce the behavior of the SiPMs and front-end electronics. Finally, the Calibration package is applied to correct the waveforms and extract the number of detected photoelectrons. A ROOT-based algorithm is then used to build an event-by-event correlation between the deposited energy and the number of detected photoelectrons. Figure 4.8 shows the output of the three steps of the simulation chain: the deposited energy of the positron from the detector simulation, the response of the SiPMs after the electronics simulation, and the corresponding distribution of photoelectrons obtained after calibration. Figure 4.9 shows the event-by-event correlation between the number of collected photoelectrons and the deposited energy, both in the full gadolinium-doped scintillator volume and within the fiducial volume. As can be seen from the two graphs in Figure 4.9, the smearing due to detector, SiPM, and electronics effects is significantly reduced by selecting events in the fiducial volume. This is because, as already discussed, events close to the detector boundaries are more affected

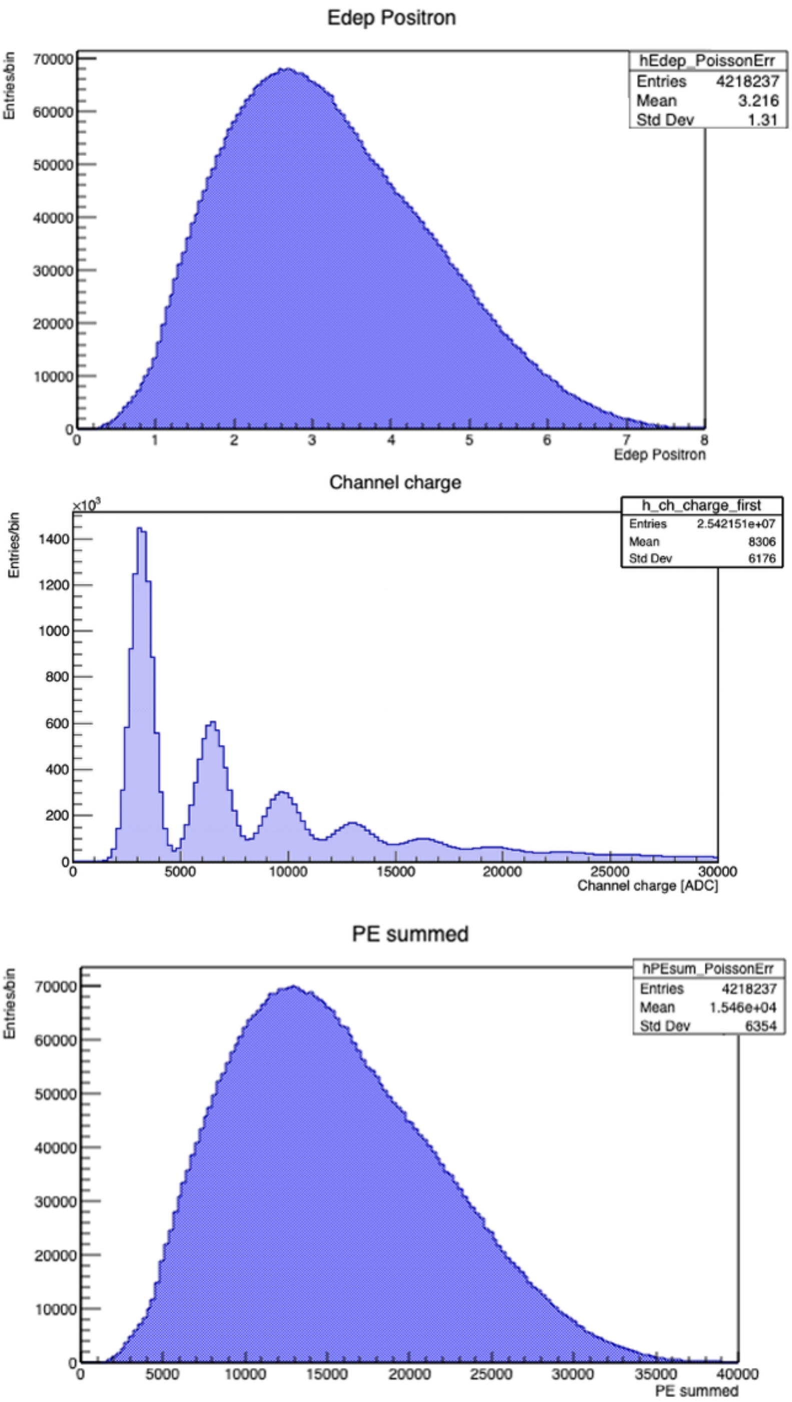

Figure 4.8: *Simulation chain results. On top, the deposited energy by the positron, output of DetSim. In the middle, the charge collected by the SiPMs, output of ElecSim. At bottom, the corresponding photoelectron distribution, output of Calibration.*

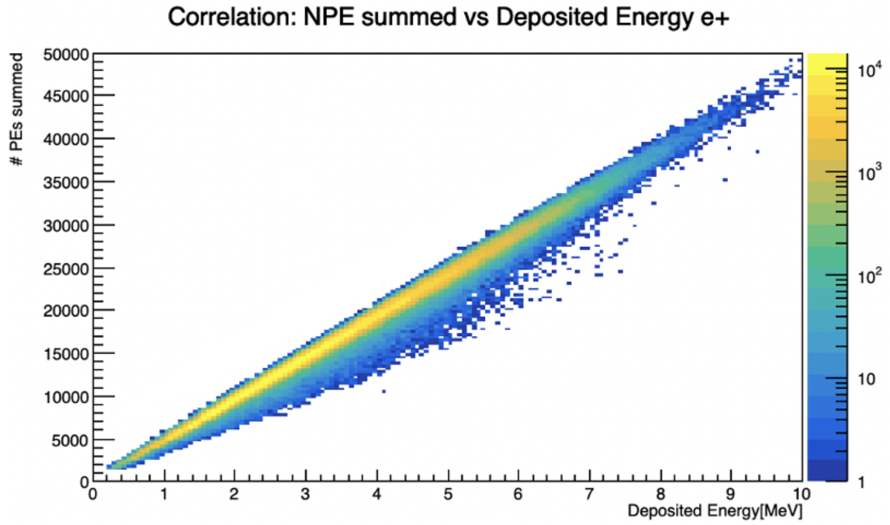

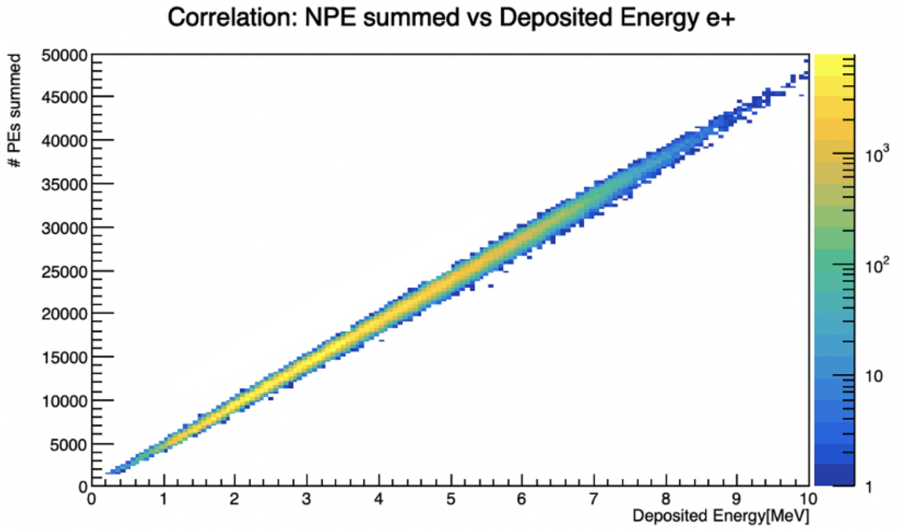

Figure 4.9: *Event-by-event correlation between the number of photoelectrons collected and the deposited energy of the positron. On top, in the whole volume. At bottom, in the fiducial volume.*

by energy leakage and light collection inefficiencies, which introduce larger fluctuations in the deposited energy. The asymmetry observed in the top plot arises from energy leakage effects, which lead to a systematic shift of the deposited energy towards values lower than the initial energy. Since part of the electromagnetic energy, in particular from annihilation gamma rays, can escape the active volume, events are predominantly distributed below the diagonal. The behavior observed in the bottom plot, where the spread is larger in the central energy region, can be explained by the interplay of different effects. At intermediate energies, the development of electromagnetic cascades and the production of secondary particles introduce larger event-by-event fluctuations in the deposited energy. At lower energies, the event topology is simpler, while at higher energies the relative fluctuations decrease, resulting in a reduced spread. In this sense, the response matrix fully encapsulates the detector effects and represents the key ingredient to connect detector-level observables to the underlying physical energy spectrum.

To obtain the response matrix, we start from the correlation between $N_{\text{p.e.}}$ and E_{dep} in the fiducial volume. Events in the energy range $[1, 9]$ MeV, corresponding to the prompt signal energy window, are selected, resulting in a reduced correlation dataset. The selected events are then used to fill a 50×50 matrix. The response matrix is finally normalized to unity, so that each element can be interpreted in a probabilistic sense. A graphical representation of the matrix is shown in Figure 4.10.

A natural application of the response matrix is the reconstruction of the initial energy spectrum from detector-level observables through unfolding techniques. In this framework, the measured distribution of photoelectrons can be related to the underlying deposited energy distribution via the response matrix. In the binned case, this relation can be written as

$$d_i = \sum_j M_{ij} \, t_j, \tag{4.4}$$

where d_i is the detector-level distribution (e.g. in photoelectrons), t_j is the true energy distribution, and M_{ij} is the response matrix. In principle, the unfolded distribution can be obtained by inverting this relation,

$$t_j = \sum_i M_{ij}^{-1} \, d_i, \tag{4.5}$$

although in general regularization techniques are required to control the amplification of statistical fluctuations and the effect of correlations among bins.

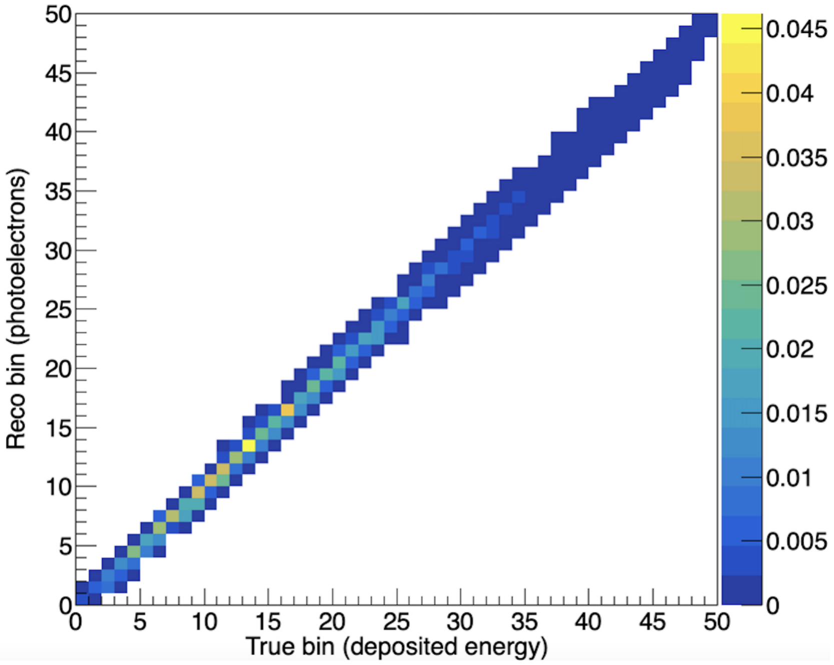

Figure 4.10: *Representation of the 50 × 50 response matrix of the photoelectrons collected in response to the energy deposited by the IBD prompt events.*

In the context of TAO, however, the response matrix can be constructed using the deposited energy, e.g. the visible energy, rather than the true initial energy. This choice is justified by the fact that, for IBD prompt events, the visible energy closely tracks the true positron energy, up to relatively small corrections arising from energy leakage and non-linear detector effects. Moreover, the primary physics goal of TAO is to provide a precise measurement of the reactor antineutrino spectrum in terms of visible energy, which is the relevant observable for oscillation analyses. In particular, JUNO will rely on the spectral shape of the visible antineutrino energy distribution, rather than on the true neutrino energy, for its physics analyses in particular for the NMO. Therefore, describing the detector response in terms of deposited energy is not only a technically convenient choice, but also directly aligned with the physical observables used in the final analyses. This makes the response matrix constructed in terms of visible energy both meaningful and sufficient for the intended applications. In fact, this choice mitigates the impact of energy leakage effects, which would otherwise introduce a strong asymmetry in the matrix, with a significant population below the diagonal, as shown in Figure 4.7. Such asymmetries make the matrix poorly conditioned and difficult to invert without regularization. By using the deposited energy, the correlation between $N_{\text{p.e.}}$ and E_{dep} becomes significantly more symmetric, as shown in Figure 4.10. As a consequence, the resulting response matrix is better conditioned and closer to a diagonally dominant structure, making it a suitable case for the application of direct unfolding techniques with reduced need for strong regularization.

In the TAO experiment, this approach could provide an alternative method to reconstruct the deposited energy of IBD prompt events starting directly from the measured charge or photoelectron distributions. Such a method would be complementary to standard reconstruction techniques based on likelihood or machine learning, and could provide an independent cross-check of the detector response and energy scale. In this work, the response matrix is constructed using Monte Carlo simulations and truth-level information, and is primarily used to study energy smearing and migration effects. However, in a realistic experimental scenario, the response matrix could be derived or tuned using calibration data, for instance from radioactive sources deployed in the detector using the Automatic Calibration Unit. This would enable data-driven corrections and validation of the detector model, reducing the dependence on simulation.

After the application of the IBD selection, the measured distribution of photoelectrons associated with prompt events could then be unfolded using such a response matrix to extract the corresponding deposited energy spectrum. This approach naturally accounts for detector effects such as resolution and inefficiencies, and provides a consistent framework to connect detector-level observables to physical quantities.

Conclusions

This thesis presents the work I carried out as a PhD student within the JUNO collaboration, in particular on the TAO experiment. The main focus has been on the characterization of the TAO front-end electronics coupled with silicon photomultipliers, and, subsequently, on the Monte Carlo simulation of inverse beta decay events in the TAO detector.

The characterization of the TAO silicon photomultipliers and front-end electronics has been performed through dedicated measurements carried out at the INFN laboratories of Roma Tre University. In particular, four figures of merit related to the silicon photomultipliers and to the front-end electronics have been checked, given their direct impact on the energy resolution of the TAO experiment. The results of the characterization are as follows: signal-to-noise ratio $\langle \mathrm{SNR} \rangle = 11.86 \pm 1.60$, single photoelectron resolution $\langle \mathrm{RES} \rangle = (13.98 \pm 1.22)$ %, crosstalk $\langle \mathrm{XTLK} \rangle = (14.45 \pm 2.57)$ %, dark count rate DCR $\simeq 25\ Hz/mm^2$. These measurements provided essential validation of the front-end electronics design and confirmed its suitability for the TAO detector requirements on the energy resolution.

Thereafter, Monte Carlo simulations of inverse beta decay events in the TAO detector were developed and analyzed within the TAO offline software framework and the JUNO DCI. The efficiency of the inverse beta decay selection cuts have been evaluated, resulting in $\varepsilon_{IBD} = (41.6 \pm 0.3)\%$. In addition, dedicated studies have been performed to investigate energy leakage effects and to characterize the detector response using large samples of simulated prompt IBD events.

Overall, the work presented in this thesis contributes to the validation of both the front-end electronics and the simulation framework of the TAO experiment. These results contribute to the commissioning and physics exploitation of TAO, supporting its role as a high-precision reference detector for JUNO in the determination of the neutrino mass ordering.

Acknowledgments

I would like to give a special thanks to all the people who have been helpful and supportive during my PhD.

First of all, I thank my supervisor, Prof. Stefano Mari, for his availability and for the help provided in the realization of the thesis.

A special thanks goes also to the coordinator of the Roma Tre JUNO group, Prof. Fabrizio Petrucci, and to the other members of the group, Prof. Andrea Fabbri and Dott. Carlo Venettacci.

I would then like to thank my parents, to whom I dedicate this thesis, a source of inspiration for me, for always supporting and sustaining me. I thank my partner Fabiola, for the encouragement and strength she has always given to me.

Bibliography

[1] W. Pauli. Letter to the participants of the tübingen conference, 1930. Reprinted in: Collected Scientific Papers, Vol. 2, p. 1313 (1964).

[2] E. Fermi. An attempt of a theory of beta radiation. *Zeitschrift für Physik*, 88:161–177, 1934.

[3] C. L. Cowan, F. Reines, F. B. Harrison, H. W. Kruse, and A. D. McGuire. Detection of the free neutrino: A confirmation. *Science*, 124:103–104, 1956. doi: 10.1126/science.124.3212.103. URL `https://doi.org/10.1126/science.124.3212.103`.

[4] B. Pontecorvo. Mesonium and anti-mesonium. *Sov. Phys. JETP*, 6:429, 1957.

[5] Y. Fukuda et al. Evidence for oscillation of atmospheric neutrinos. *Phys. Rev. Lett.*, 81:1562–1567, 1998. doi: 10.1103/PhysRevLett.81.1562.

[6] S. L. Glashow. Partial Symmetries of Weak Interactions. *Nucl. Phys.*, 22:579–588, 1961. doi: 10.1016/0029-5582(61)90469-2.

[7] Abdus Salam. Weak and electromagnetic interactions. In Nils Svartholm, editor, *Elementary particle theory*, pages 367–377. Almquist & Wiksell, 1968.

[8] Steven Weinberg. A Model of Leptons. *Phys. Rev. Lett.*, 19:1264–1266, 1967. doi: 10.1103/PhysRevLett.19.1264.

[9] R. L. Workman and Others. Review of Particle Physics. *PTEP*, 2022: 083C01, 2022. doi: 10.1093/ptep/ptac097.

[10] Peter W. Higgs. Broken symmetries, massless particles and gauge fields. *Phys. Lett.*, 12:132–133, 1964. doi: 10.1016/0031-9163(64)91136-9.

[11] Georges Aad et al. Observation of a new particle in the search for the Standard Model Higgs boson with the ATLAS detector at the LHC. *Phys. Lett. B*, 716:1–29, 2012. doi: 10.1016/j.physletb.2012.08.020.

[12] Serguei Chatrchyan et al. Observation of a New Boson at a Mass of 125 GeV with the CMS Experiment at the LHC. *Phys. Lett. B*, 716:30–61, 2012. doi: 10.1016/j.physletb.2012.08.021.

[13] P. M. Watkins. Discovery of the W and Z bosons. *Contemp. Phys.*, 27: 291–324, 1986. doi: 10.1080/00107518608211015.

[14] Gerard 't Hooft. Naturalness, chiral symmetry, and spontaneous chiral symmetry breaking. *NATO Sci. Ser. B*, 59:135–157, 1980. doi: 10.1007/978-1-4684-7571-5_9.

[15] M. C. Gonzalez-Garcia and Yosef Nir. Neutrino Masses and Mixing: Evidence and Implications. *Rev. Mod. Phys.*, 75:345–402, 2003. doi: 10.1103/RevModPhys.75.345.

[16] Ziro Maki, Masami Nakagawa, and Shoichi Sakata. Remarks on the Unified Model of Elementary Particles. *Progress of Theoretical Physics*, 28(5):870–880, 11 1962. ISSN 0033-068X. doi: 10.1143/PTP.28.870. URL `https://doi.org/10.1143/PTP.28.870`.

[17] S. P. Mikheyev and A. Yu. Smirnov. Resonance Amplification of Oscillations in Matter and Spectroscopy of Solar Neutrinos. *Sov. J. Nucl. Phys.*, 42:913–917, 1985.

[18] S. P. Mikheyev and Alexei Yu. Smirnov. Resonant amplification of ν oscillations in matter and solar-neutrino spectroscopy. *Il Nuovo Cimento C*, 9:17–26, 1986.

[19] L. Wolfenstein. Neutrino Oscillations in Matter. *Phys. Rev. D*, 17: 2369–2374, 1978. doi: 10.1103/PhysRevD.17.2369.

[20] M. Blennow. Theoretical and phenomenological studies of neutrino physics. *PhD thesis*, 2015.

[21] N. Agafonova et al. Latest results of the OPERA experiment on nu-tau appearance in the CNGS neutrino beam. *SciPost Phys. Proc.*, 1:028, 2019. doi: 10.21468/SciPostPhysProc.1.028.

[22] I. Ambats et al. The MINOS Detectors Technical Design Report. *Journal Name*, 10 1998. doi: 10.2172/1861363.

[23] K. Abe et al. The T2K Experiment. *Nucl. Instrum. Meth. A*, 659: 106–135, 2011. doi: 10.1016/j.nima.2011.06.067.

[24] Q. R. Ahmad et al. Direct evidence for neutrino flavor transformation from neutral current interactions in the Sudbury Neutrino Observatory. *Phys. Rev. Lett.*, 89:011301, 2002. doi: 10.1103/PhysRevLett.89.011301.

[25] S. Abe et al. Precision Measurement of Neutrino Oscillation Parameters with KamLAND. *Phys. Rev. Lett.*, 100:221803, 2008. doi: 10.1103/PhysRevLett.100.221803.

[26] G. Bellini et al. Final results of Borexino Phase-I on low energy solar neutrino spectroscopy. *Phys. Rev. D*, 89(11):112007, 2014. doi: 10.1103/PhysRevD.89.112007.

[27] F. P. An et al. Observation of electron-antineutrino disappearance at Daya Bay. *Phys. Rev. Lett.*, 108:171803, 2012. doi: 10.1103/PhysRevLett.108.171803.

[28] J. K. Ahn et al. Observation of Reactor Electron Antineutrino Disappearance in the RENO Experiment. *Phys. Rev. Lett.*, 108:191802, 2012. doi: 10.1103/PhysRevLett.108.191802.

[29] Angel Abusleme et al. JUNO Physics and Detector. 4 2021.

[30] Ivan Esteban, M. C. Gonzalez-Garcia, Michele Maltoni, Ivan Martinez-Soler, João Paulo Pinheiro, and Thomas Schwetz. Nufit 6.0: Updated global analysis of three-flavor neutrino oscillations, 2024. URL `http://www.nu-fit.org/`. Preprint or online resource.

[31] T. Wester, K. Abe, C. Bronner, Y. Hayato, K. Hiraide, and et al. Atmospheric neutrino oscillation analysis with neutron tagging and an expanded fiducial volume in Super-Kamiokande i–v. *Physical Review D*, 109(7), April 2024. doi: 10.1103/PhysRevD.109.072005.

[32] IceCube Collaboration. Measurement of atmospheric neutrino oscillation parameters using convolutional neural networks with 9.3 years of data in IceCube DeepCore, 2024. URL `https://icecube.wisc.edu/`. Collaboration internal or preprint.

[33] Jeremy Wolcott. New NOvA results with 10 years of data, 2024. URL `https://agenda.infn.it/event/37867/contributions/233955/attachments/121832/177712/2024-06-17`. Conference presentation.

[34] Y. Abe and et al. Improved measurements of the neutrino mixing angle θ_{13} with the Double Chooz detector. *Journal of High Energy Physics*, pages 1–44, 2014. doi: 10.1007/JHEP10(2014)086. URL `https://doi.org/10.1007/JHEP10(2014)086`.

[35] R. E. Carter, F. Reines, J. J. Wagner, and M. E. Wyman. Free antineutrino absorption cross section. expected cross section from measurements of fission fragment electron spectrum. *Physical Review*, 113: 280–286, 1959.

[36] M. Fallot, S. Cormon, M. Estienne, A. Algora, V. M. Bui, A. Cucoanes, M. Elnimr, L. Giot, D. Jordan, J. Martino, A. Onillon, A. Porta, G. Pronost, A. Remoto, J. L. Tain, F. Yermia, and A.-A. Zakari-Issoufou. New antineutrino energy spectra predictions from the summation of beta decay branches of the fission products. *Physical Review Letters*, 109:202504, 2012.

[37] A. C. Hayes, J. L. Friar, G. T. Garvey, Gerard Jungman, and G. Jonkmans. Systematic uncertainties in the analysis of the reactor neutrino anomaly. *Physical Review Letters*, 112:202501, 2014.

[38] A. A. Hahn, K. Schreckenbach, W. Gelletly, F. von Feilitzsch, G. Colvin, and B. Krusche. Antineutrino spectra from ^{241}Pu and ^{239}Pu thermal neutron fission products. *Physics Letters B*, 218(3):365–368, 1989.

[39] P. Huber. Determination of antineutrino spectra from nuclear reactors. *Physical Review C*, 84:024617, 2011. doi: 10.1103/PhysRevC.84.024617. URL `https://doi.org/10.1103/PhysRevC.84.024617`.

[40] T. A. Mueller et al. Improved predictions of reactor antineutrino spectra. *Physical Review C*, 83:054615, 2011. doi: 10.1103/PhysRevC.83.054615. URL `https://doi.org/10.1103/PhysRevC.83.054615`.

[41] D. Adey et al. Extraction of the ^{235}U and ^{239}Pu Antineutrino Spectra at Daya Bay. *Phys. Rev. Lett.*, 123(11):111801, 2019. doi: 10.1103/PhysRevLett.123.111801.

[42] G. Mention, M. Fechner, Th. Lasserre, Th. A. Mueller, D. Lhuillier, M. Cribier, and A. Letourneau. The reactor antineutrino anomaly. *Physical Review D*, 83:073006, 2011.

[43] N. Dinu et al. Characteristics of a prototype matrix of silicon photomultipliers (sipm). *Journal of Instrumentation (JINST)*, 4:P03016, 2009.

[44] A. Abusleme et al. Tao conceptual design report: A precision measurement of the reactor antineutrino spectrum with sub-percent energy resolution. *arXiv preprint*, 2020. URL `https://arxiv.org/abs/2005.08745`.

[45] F. Capozzi, E. Lisi, and A. Marrone. Neutrino mass hierarchy and electron neutrino oscillation parameters with one hundred thousand reactor events. *Physical Review D*, 89(1):013001, 2014. doi: 10.1103/PhysRevD.89.013001. URL `https://doi.org/10.1103/PhysRevD.89.013001`.

[46] A. Strumia and F. Vissani. Precise quasielastic neutrino/nucleon cross-section. *Physics Letters B*, 564:42–54, 2003. doi: 10.1016/S0370-2693(03)00616-6. URL `https://doi.org/10.1016/S0370-2693(03)00616-6`.

[47] A. Abusleme et al. Juno physics and detector. *Progress in Particle and Nuclear Physics*, 123:103927, 2021. doi: 10.1016/j.ppnp.2021.103927. URL `https://doi.org/10.1016/j.ppnp.2021.103927`.

[48] F. An et al. Neutrino physics with juno. *Journal of Physics G: Nuclear and Particle Physics*, 43(3):030401, 2016. doi: 10.1088/0954-3899/43/3/030401. URL `https://doi.org/10.1088/0954-3899/43/3/030401`.

[49] Francesco Capozzi, Eligio Lisi, and Antonio Marrone. Mapping reactor neutrino spectra from TAO to JUNO. *Physical Review D*, 102(5), September 2020. ISSN 2470-0029. doi: 10.1103/PhysRevD.102.056001. URL `http://dx.doi.org/10.1103/PhysRevD.102.056001`.

[50] Angel Abusleme et al. First measurement of reactor neutrino oscillations at juno, 2025. URL `https://arxiv.org/abs/2511.14593`.

[51] A. A. Sonzogni, M. Nino, and E. A. McCutchan. Revealing fine structure in the antineutrino spectra from a nuclear reactor. *Physical Review C*, 98(1), July 2018. ISSN 2469-9993. doi: 10.1103/PhysRevC.98.014323. URL `http://dx.doi.org/10.1103/PhysRevC.98.014323`.

[52] A. Aguilar-Arevalo et al. Evidence for neutrino oscillations from the observation of $\bar{\nu}_e$ appearance in a $\bar{\nu}_\mu$ beam. *Physical Review D*, 64: 112007, 2001. doi: 10.1103/PhysRevD.64.112007.

[53] A. Aguilar-Arevalo et al. Improved search for $\bar{\nu}_\mu \rightarrow \bar{\nu}_e$ oscillations in the miniboone experiment. *Physical Review Letters*, 110:161801, 2013. doi: 10.1103/PhysRevLett.110.161801.

[54] A. Aguilar-Arevalo et al. Significant excess of electronlike events in the miniboone short-baseline neutrino experiment. *Physical Review Letters*, 121(22):221801, 2018. doi: 10.1103/PhysRevLett.121.221801.

[55] J. Kostensalo, J. Suhonen, C. Giunti, and P. C. Srivastava. The gallium anomaly revisited. *Physics Letters B*, 795:547–547, 2019. doi: 10.1016/j.physletb.2019.06.025.

[56] S. Schael et al. Precision electroweak measurements on the z resonance. *Physics Reports*, 427:257–454, 2006. doi: 10.1016/j.physrep.2005.12.006.

[57] Alexander L. Read. Presentation of search results: The cls technique. *Journal of Physics G*, 28:2693–2704, 2002. doi: 10.1088/0954-3899/28/10/313.

[58] Thomas Junk. Confidence level computation for combining searches with small statistics. *Nuclear Instruments and Methods in Physics Research Section A*, 434:435–443, 1999. doi: 10.1016/S0168-9002(99)00498-2.

[59] D. Adey, F. P. An, A. B. Balantekin, et al. Improved measurement of the reactor antineutrino flux at daya bay. *Physical Review D*, 100(5), September 2019. ISSN 2470-0029. doi: 10.1103/PhysRevD.100.052004. URL `http://dx.doi.org/10.1103/PhysRevD.100.052004`.

[60] X. Chen, G. F. Cao, M. H. Qu, et al. Burn-in test and thermal performance evaluation of silicon photomultipliers for the juno–tao experiment. *Journal of Instrumentation*, 19:C07008, July 2024. doi: 10.1088/1748-0221/19/07/C07008. URL `https://doi.org/10.1088/1748-0221/19/07/C07008`.

[61] J. Liu, B. Cai, R. Carr, et al. Automated calibration system for a high-precision measurement of neutrino mixing angle θ_{13} with the daya bay antineutrino detectors. *Nuclear Instruments and Methods in Physics Research Section A*, 750:19–37, 2014. doi: 10.1016/j.nima.2014.02.049.

[62] Ruhui Li, Guofu Cao, Jun Cao, Yichen Li, Yifang Wang, Zhimin Wang, and Liang Zhan. Detector optimization to reduce the cosmogenic neutron backgrounds in the tao experiment. 2022. URL `https://arxiv.org/abs/2206.01112`. v4.

[63] Claudio Piemonte and Alberto Gola. Overview on the main parameters and technology of modern silicon photomultipliers. volume 926, pages 2–15. 2019.

[64] Maria Giuseppina Bisogni, Alberto Del Guerra, and Nicola Belcari. Medical applications of silicon photomultipliers. *Nuclear Instruments and Methods in Physics Research Section A: Accelerators, Spectrometers, Detectors and Associated Equipment*, 926:118–128, 2019.

[65] A. Dalla Mora et al. Fast silicon photomultiplier improves signal harvesting and reduces complexity in time-domain diffuse optics. *Optics Express*, 23(11):13937–13946, 2015.

[66] F. Acerbi et al. High-density silicon photomultipliers: Performance and linearity evaluation for high efficiency and dynamic-range applications. *IEEE Journal of Quantum Electronics*, 54(2):1–7, 2018. doi: 10.1109/JQE.2018.2802542.

[67] K. Balygin et al. A quantum random number generator based on the 100 mbit/s poisson photocount statistics. *Journal of Experimental and Theoretical Physics*, 126(6):728–740, 2018. doi: 10.1134/S1063776118060018.

[68] G. Ambrosi and V. Vagelli. Applications of silicon photomultipliers in ground-based and spaceborne high-energy astrophysics. *The European Physical Journal Plus*, 137(1):170, 2022. ISSN 2190-5444. doi: 10.1140/epjp/s13360-021-02159-4.

[69] Martin Aleksa et al. Calorimetry at fcc-ee. *The European Physical Journal Plus*, 136:1066, 2021. doi: 10.1140/epjp/s13360-021-02034-2.

[70] S. Vinogradov. Analytical models of probability distribution and excess noise factor of solid state photomultiplier signals with crosstalk. *Nuclear Instruments and Methods in Physics Research Section A: Accelerators, Spectrometers, Detectors and Associated Equipment*, 695:247–251, 2012. doi: 10.1016/j.nima.2011.11.086.

[71] P. C. Consul and F. Famoye. *Lagrangian Probability Distributions.* Birkhäuser, Boston, 2006.

[72] Hamamatsu Photonics K.K. Mppc (sipms) / spads – product overview. Online, n.d. URL `https://www.hamamatsu.com/eu/en/product/optical-sensors/mppc.html`.

[73] P. Moreira et al. White rabbit: Sub-nanosecond timing distribution over ethernet. *JINST*, 4:P09004, 2009.

[74] Analog Devices Inc. Ltc6269 – product overview. Online, n.d.. URL `https://www.analog.com/en/products/ltc6269.html`.

[75] Analog Devices Inc. Ltc6405 – product overview. Online, n.d.. URL `https://www.analog.com/en/products/ltc6405.html#product-overview`.

[76] Analog Devices Inc. Ad9083 – product overview. Online, n.d.. URL `https://www.analog.com/en/products/ad9083.html#product-overview`.

[77] GitHub contributors. Fpga board system architecture. GitHub repository, n.d. URL `https://github.com/palzhj/u4fcpv2`.

[78] Xiaomei Zhang et al. Juno distributed computing system. *EPJ Web of Conferences*, 295:04030, 2024. doi: 10.1051/epjconf/202429504030. Proceedings of CHEP 2023.

[79] J. Zou, Xiang-Jie Huang, W. D. Li, et al. Sniper: an offline software framework for non-collider physics experiments. *Journal of Physics: Conference Series*, 664(7):072053, December 2015. doi: 10.1088/1742-6596/664/7/072053.

[80] Xing-tao Huang, Teng Li, Jiaheng Zou, et al. Offline data processing software for the juno experiment. In *Proceedings of Science*, volume 282, page 1051, February 2017. doi: 10.22323/1.282.1051.

[81] J. Allison, K. Amako, J. Apostolakis, et al. Recent developments in geant4. *Nuclear Instruments and Methods in Physics Research Section A*, 835:186–225, 2016. ISSN 0168-9002. doi: 10.1016/j.nima.2016.06.125. URL `https://www.sciencedirect.com/science/article/pii/S0168900216306957`.

[82] R. Brun and F. Rademakers. Root: An object oriented data analysis framework. *Nuclear Instruments and Methods in Physics Research Section A*, 389:81–86, 1997. doi: 10.1016/S0168-9002(97)00048-X.

[83] C. Andreopoulos et al. The genie neutrino monte carlo generator. *Nuclear Instruments and Methods in Physics Research Section A*, 614:87–104, 2010. doi: 10.1016/j.nima.2009.12.009.

[84] F. P. An et al. A side-by-side comparison of daya bay antineutrino detectors. *Nuclear Instruments and Methods in Physics Research Section A*, 685:78–97, 2012. doi: 10.1016/j.nima.2012.05.030.

[85] J. Xie, J. Cao, Y. Ding, M. Liu, X. Sun, W. Wang, and Y. Xie. A liquid scintillator for a neutrino detector working at $-50°$. *Nuclear Instruments*

and Methods in Physics Research Section A, 1009:165459, 2021. doi: 10.1016/j.nima.2021.165459.

[86] Hangyu Shi, Jun Wang, Guofu Cao, Wei Wang, and Yuehuan Wei. Vertex reconstruction in the tao experiment. *arXiv preprint*, 2025.